

POLITECNICO DI TORINO

Master Degree course in Chemical and Sustainable Processes Engineering

Master Degree Thesis

CFD modeling of biomass hydrolysis reactors

Supervisor

MARCHISIO Daniele Augier Frederic Bouras Meriem Rezazadeh Niki

Candidate
Bernelli Matteo

ACADEMIC YEAR 2024-2025

RINGRAZIAMENTI

Desidero esprimere la mia più sincera gratitudine al gruppo di ricerca nel quale ho avuto la fortuna di lavorare e portare a termine questa esperienza. La costante disponibilità, i preziosi consigli e la guida che mi avete fornito nell'arco di questi mesi hanno reso possibile la realizzazione di questo lavoro. La vostra competenza e il vostro sostegno sono stati fondamentali in ogni fase del percorso.

Un ringraziamento speciale va anche al professore Marchsio Daniele che ha permesso la realizzazione di questo lavoro e che mi ha supportato durante il mio periodo di ricerca. La sua presenza e il suo supporto, insieme alla sua disponibilità, hanno reso questa esperienza estremamente formativa e arricchente.

Infine, desidero ringraziare tutte le persone che hanno contribuito a rendere indimenticabile la mia esperienza all'estero: grazie a voi non solo ho avuto l'opportunità di crescere dal punto di vista accademico e professionale, ma ho anche potuto vivere un percorso umano e personale di grande valore che porterò per sempre nel mio cuore.

Abstract

The intensification of climate change has stimulated the research for sustainable energy sources, among which second generation (2G) bioethanol has emerged as a promising alternative. This biofuel can be obtained through the fermentation of simple sugars derived from lignocellulosic biomass. A critical step in the biomass hydrolysis process is the liquefaction, where pretreated biomass is converted into glucose through the action of enzymes. To ensure economic feasibility, this step must be conducted at high solids loading to minimize water usage and reduce the energy demand for distillation of ethanol in the last step of the process. However, under such conditions the biomass slurry exhibits non-Newtonian behaviour, leading to significant challenges in the mixing process and in the description of system evolution during enzymatic hydrolysis. To overcome these challenges, this work developed the computational fluid dynamics (CFD) model of the reactors used to conduct biomass liquefaction in the experimental tests. The study began with a literature review aimed to have a better understand of the main difficulties associated with modelling of biomass hydrolysis reactors and the mixing of non-Newtonian fluids. A reference study was then selected to build a validated model: the geometry of the reactor described in the paper was reconstructed, and the torque values on the impeller at different rotational speeds were compared with the reported experimental data. This validation procedure confirmed the reliability of the model for both Newtonian and non-Newtonian fluids and enabled the estimation of some important hydrodynamic parameters such as the power input, the average shear rate, the elongation and the fraction of dead zones during the agitation. After this section, CFD models of the experimental reactors were developed, including the IKA systems equipped with Paravisc and Anchor impellers, as well as the TORNADO reactor. From these simulations, it was possible to construct the Power Number-Reynolds curve (Np-Re) in the laminar regime, different for each geometry. In the end, the several hydrodynamic parameters that may have an impact on the biomass conversion were extracted. The subsequent analysis revealed that all the hydrodynamic parameters investigated may have an influence on the glucose conversion, particularly during the first two hours of the liquefaction. Beyond this initial phase, their impact on the conversion rate diminished significantly, suggesting that other factors become more important. Nonetheless, it was not possible to determine the relative contribution of each hydrodynamic parameter using a single system and one set of experimental data. To achieve this, further simulations and experimental studies under different conditions are required, particularly with the Anchor IKA and TORNADO reactors, which will provide complementary information about the relation between glucose conversion and the reactors hydrodynamic. In this work the CFD model of three different reactors has been created and validated leading to the possibility to build the Power Number-Reynolds curve for different geometry and extract important hydrodynamic parameters for different operating conditions. This demonstrates the value of CFD modeling as a tool for analysing the liquefaction of lignocellulosic biomass at high solids loading, giving the possibility to calculate parameters that are impossible to measure in laboratory. This works is the first attempt to investigate and identify the scale up criteria for hydrolysis reaction.

Contents

0.1	Extend	ded Summary in Italian
	0.1.1	Introduzione
	0.1.2	Numero di potenza e costante di Metzner Otto
	0.1.3	Validazione delle simulazioni
	0.1.4	Reattori IKA e TORNADO
	0.1.5	Correlazione tra agitazione e conversione della biomassa 12
	0.1.6	Conclusioni
0.2	Introd	uction
0.3	Lignoo	cellulosic biomass
	0.3.1	Cellulose
	0.3.2	Hemicellulose
	0.3.3	Lignin
0.4	Proces	s Overview
0.5	Comp	utational Fluid Dynamics and Governing Equation
	0.5.1	Conservation Equation
	0.5.2	Solution Strategies
	0.5.3	Numerical Diffusion
	0.5.4	Rotating Frame Motion
	0.5.5	Simulation and Boundary Conditions
0.6	Non-N	Tewtonian fluids and Rheological Models
	0.6.1	Biviscosity Model
0.7	Power	Number
0.8	Metzn	er e Otto Constant
0.9	Model	Validation
0.10		g of the Experimental Data
0.11		Reactors
		Geometry
	0.11.2	Mesh
	0.11.3	Metzner Otto Constant
		Real Rheology Simulations
0.12		do Reactor
		Geometry
		Mesh
		Metzner Otto Constant
		Real Rheology Simulation 76

Bibliography	87
0.15 Conclusion	85
0.14 Correlation between Fluid Agitation and Glucose Conversion	81
0.13 Comparison of Reactor Configurations	79

0.1 Extended Summary in Italian

0.1.1 Introduzione

L'intensificazione dei cambiamento climatici sta stimolando la ricerca di fonti energetiche sostenibili ed alternative, tra le quali la produzione di bioetanolo di seconda generazione. Questo biocarburante può essere ottenuto attraverso la fermentazione di zuccheri semplici derivati dall'idrolisi della biomassa lignocellulosica, ottenuta come scarto da varie industrie.

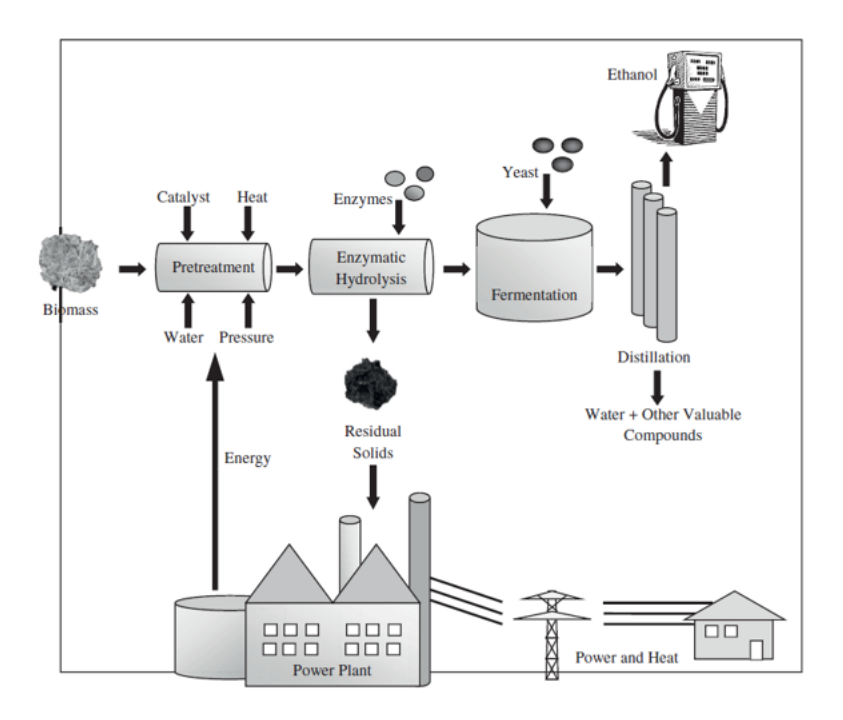


Figure 1. Schema del processo di produzione di bioetanolo partento da biomassa. [7]

Una fase critica nel processo è lo step che prende il nome di liquefazione, durante il quale la biomassa pretrattata viene convertita in glucosio grazie all'azione di enzimi. In questa fase la concentrazione di solidi deve essere elevata, in modo tale da minimizzare l'uso di acqua e ridurre il fabbisogno energetico per la distillazione dell'etanolo nell'ultima fase del processo. Tuttavia, in tali condizioni, la sospensione di biomassa presenta un comportamento fortemente non newtoniano, rendendo complicato il processo di miscelazione e la descrizione dell'evoluzione del sistema durante l'idrolisi enzimatica. L'obiettivo del lavoro è di creare il modello CFD dei reattori per la liquefazione utilizzati in laboratorio, in modo tale da riuscire a simulare la fluidodinamica del processo. Inoltre, in questo lavoro è stata tracciata una possibile strategia da seguire per identificare quali sono i possibili parametri fluidodinamici che influenzano la conversione del glucosio. Questa potrebbe essere utilizzata in futuro per identificare il miglior parametro da utilizzare per lo scale up dei reattori per l'idrolisi della biomassa.

0.1.2 Numero di potenza e costante di Metzner Otto

Durante lo studio delle prestazioni dei vari reattori sono stati selezionati e analizzati alcuni parametri fluidodinamici, tra cui la potenza necessaria per l'agitazione, lo shear rate medio, l'intensità di deformazione e la percentuale di zone stagnanti nel reattore durante l'agitazione.

Per ogni geometria è possibile costruire una particolare curva, che vede il numero di potenza in funzione del numero di Revnolds.

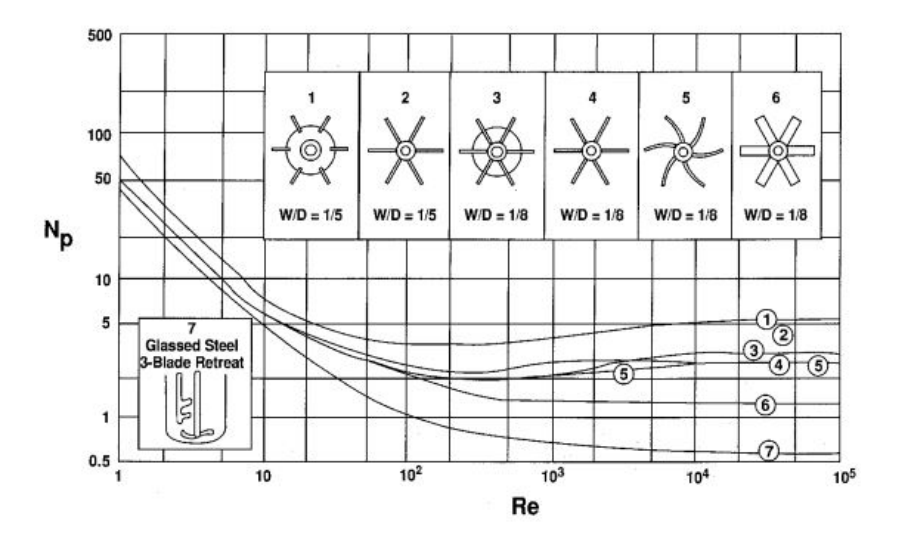


Figure 2. Numero di potenza vs. numero di Reynolds per differenti tipologie di giranti. [8]

Nel grafico (2) è possibile osservare che ogni geometria ha una curva specifica, la quale può essere suddivisa in tre sezioni a seconda del regime fluidodinamica all'interno del reattore. La sezione di maggior interesse per questo studio è quella a basso numero di Reynolds, ovvero quando il regime fluidodinamico è laminare, dove si ha una relazione lineare tra il numero di potenza (Np) e il numero di Reynolds (Re).

Questa tipologia di grafici sono molto utili poichè conoscendo il numero di Reynolds all'interno del reattore è possibile risalire al numero di potenza, Np, mediante una relazione semplice e successivamente è possibile calcolare la potenza necessaria per l'agitazione mediante la formula seguente.

$$P = NpN^3D^5\rho \tag{1}$$

Nell'equazione (1) N indica la velocità rotazionale in giri al secondo, D è il diametro della girante e ρ è la densità del fluido.

La potenza assorbita può essere calcolata anche partendo dal momento torcente generato dall'agitazione del fluido sull'impeller, che a sua volta è stimabile dalle simulazioni CFD. Grazie alle simulazioni è stato possibile creare la curva Np-Re per ogni geometria disponibile ed utilizzarla anche per il calcolo della costante di Metzner Otto.

Quest'ultima permette di stimare lo shear rate medio all'interno del reattore durante

l'agitazione mediante la relazione seguente.

$$\dot{\gamma}_{eff} = K_s N \tag{2}$$

Nell'equazione (2), N è la velocità rotazionale in giri al secondo e Ks è la costante di Metzner Otto. Essa dipende dalla geometria del sistema e in parte minore dalla reologia del fluido.

Un altro parametro fluidodinamico preso in considerazione è l'intensità di deformazione media subita dal fluido durante il moto. Quest'ultimo si ricava partendo dal gradiente di velocità medio all'interno del reattore e scomponendolo nelle sue due componenti, il tensore di deformazione e il tensore di vorticità. Il tensore di deformazione fa riferimento al moto del fluido tenendo in considerazione solamente la deformazione e senza il contributo della rotazione. Al contrario, il tensore di vorticità tiene in considerazione solamente la rotazione senza il contributo di deformazione. A questo punto è possibile calcolare la norma di ogni tensore che indicherà rispettivamente l'intensità di deformazione media subita dal fluido durante l'agitazione e l'intensità della rotazione media dello stesso.

L'ultimo paramentro analizzato nello studio sono le zone morte dei reattori durante l'agitazione. Queste sono definite come porzioni di fluido che non si muovono durante l'agitazione e per questo motivo sono scarsamente miscelate, influendo negativamente sulla conversione finale.

0.1.3 Validazione delle simulazioni

La validazione delle simulazioni è stata svolta partendo da una ricerca bibliografica in modo tale da individuare lavori che avessero una tematica simile a questa e comprendere al meglio le difficoltà del processo di idrolisi della biomassa lignocellulosica. Inoltre, è stato svolto uno studio approfondito sulla miscelazione dei fluidi non Newtoniani.

Al termine di questa sezione, è stato selezionato un articolo scientifico come punto di riferimento [2] per la creazione di un modello CFD i cui risultati potessero essere confrontati con dei valori sperimentali. A questo scopo, è stato ricreato il modello CFD del reattore utilizzato nell'articolo e sono stati confrontati i valori sperimentali di momento torcente sulla girante del reattore con i valori ottenuti dalle simulazioni, sia per fluidi Newtoniani che non Newtoniani. In questo modo il modello è stato validato per entrambe le tipologie di fluido. Oltre a questo, è stata calcolata la curva Numero di Potenza–Reynolds, la costante di Metzner Otto (utile per calcolare lo shear rate medio all'interno del reattore) e altri due parametri fluidodinamici, quali l'elongazione media del fluido e la percentuale di zone stagnanti durante l'agitazione.

Per quanto riguarda la validazione delle simulazioni per i fludi Newtoniani possiamo osservare il seguente grafico.

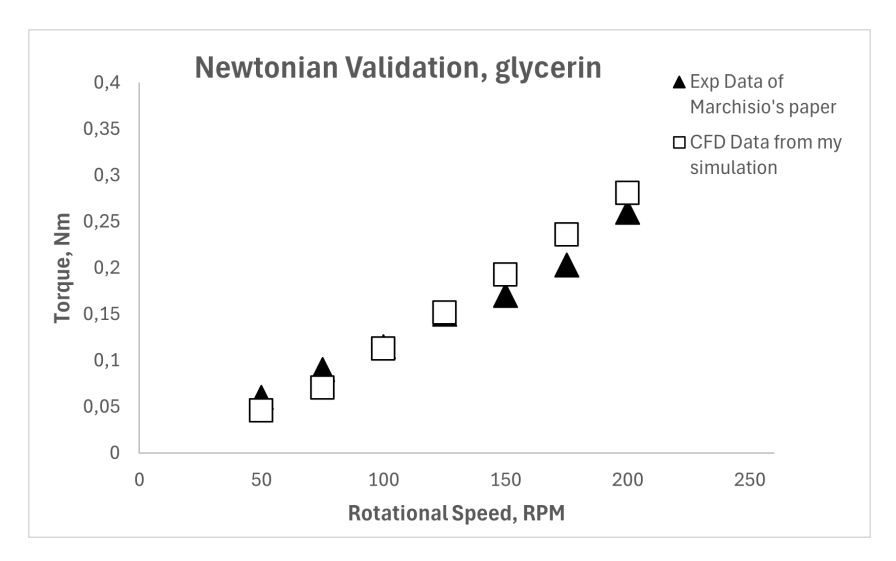


Figure 3. Confronto tra le misure sperimentali di momento torcente (triangoli neri) e i valori di momento torcente calcolati tramite simulazione (quadrati bianchi). Il fluido usato è la glicerina a 36 gradi centigradi, $\mu = 0.37 Pas$. [2]

Tramite la figura (3) è possibile osservare come le simulazioni CFD siano in grado di riprodurre i risultati ottenuti sperimentalmente. Gli errori sono compresi in un range tra 1% - 20%.

A seguire è stata svolta anche la validazione per i fluidi Non Newtoniani utilizzando il modello di Herschel Bulkley. I risultati sono mostrati nella figura successiva e anche in questo caso si nota come le simulazioni riproducano con una buona qualità i risultati sperimentali, con un range di errore che va dal 1% al 15%.

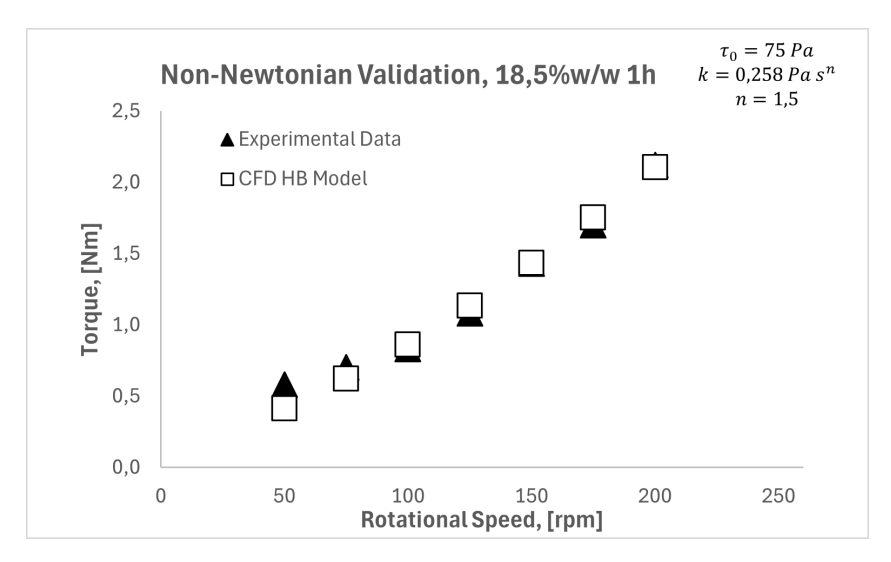


Figure 4. Confronto tra i valori di momento torcente sperimentali e quelli ottenuti via CFD per un fluido con una concentrazione pari a $18.5\% \frac{w}{w}$ di solidi dopo un'ora di reazione. [2]

Utilizzando alcune reologie di fluidi Newtoniani è stato possibile la costruzione del grafico Np-Re, ovvero numero di potenza in funzione del numero di Reynolds, per il regime laminare.

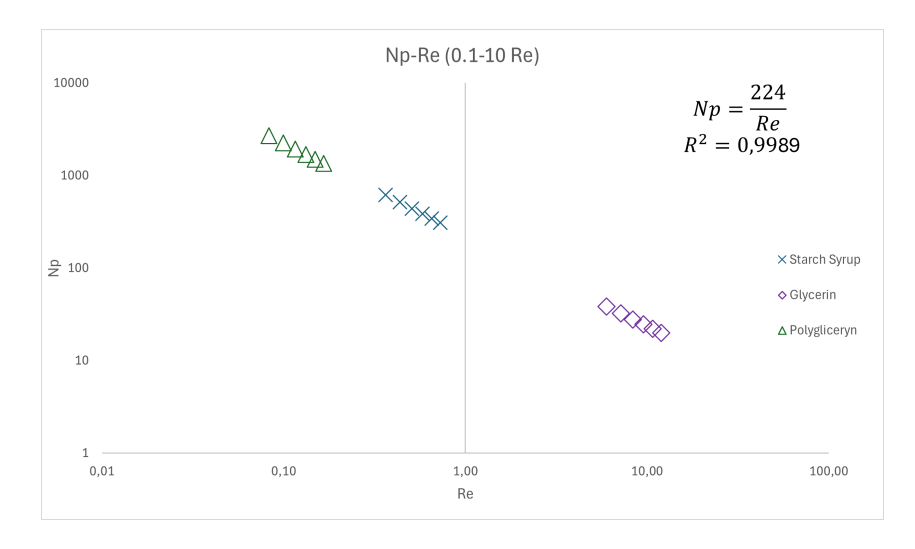
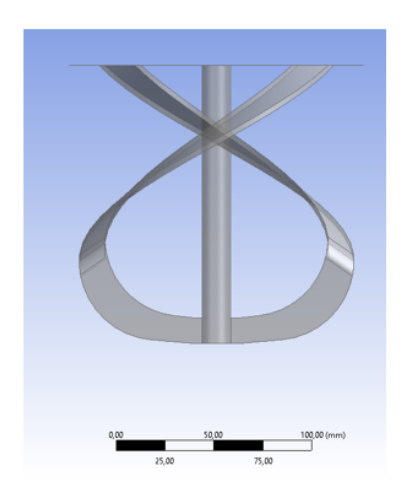


Figure 5. Np vs Reynolds per la geometria usata nel lavoro [2].

I punti seguono una linea retta e questo ci conferma che il regime è laminare e il numero di Reynolds è compreso tra 1-10. Utilizzando questa tipologia di grafici è possibile andare a calcolare la costante di potenza, ovvero la constate che definisce la linea retta, funzione solamente della geometria del sistema. Da questa costante è stato poi possibile stimare la costante di Metzner Otto.

0.1.4 Reattori IKA e TORNADO

Il passo successivo è stato quello di crea il modello per i reattori utilizzati nelle prove in laboratorio. In particolare, è stato creato il modello CFD del reattore IKA, sia equipaggiato con la girante Anchor sia Paravisc, e del reattore TORNADO. Inoltre, è stata ottenuta la reologia del fluido durante il processo utilizzando il reattore IKA Paravisc, per tre diverse velocità rotazionali e per diversi campionamenti temporali. Mediante l'ipotesi che l'evoluzione della reologia nel tempo fosse simile per le tre diverse configurazioni, è stato possibile simulare tutti i sistemi con la stessa reologia. Questo ha permesso di fare dei paragoni tra i diversi reattori, confrontando i parametri fluidodinamici come la potenza necessaria per l'agitazione, lo shear rate medio e l'elongazione media permettendo così di sottolineare come i vari sistemi si comportano in modo differente e permettano di ottenere prestazioni diverse durante l'agitazione.



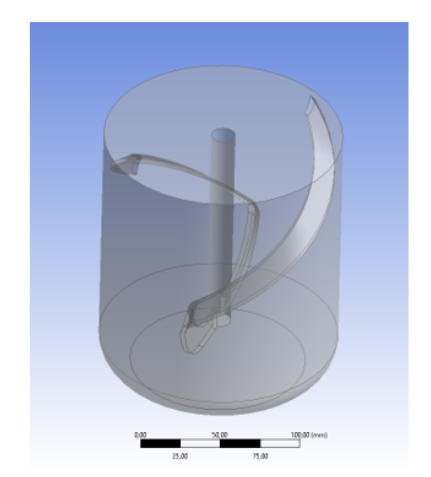
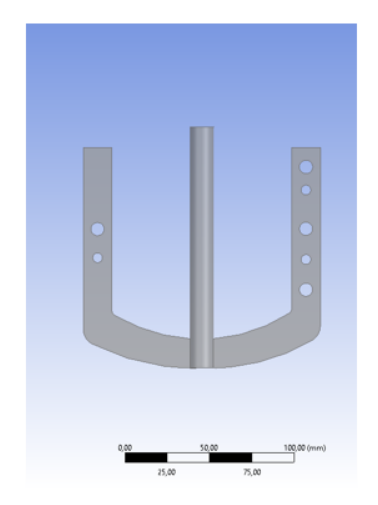


Figure 6. Geometria della girante Paravisc e del reattore IKA.



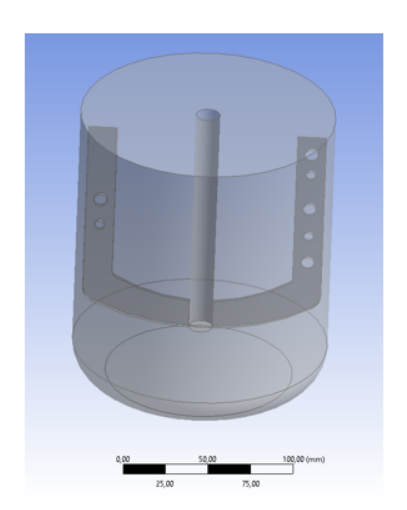


Figure 7. Geometria della girante Anchor e del reattore IKA.

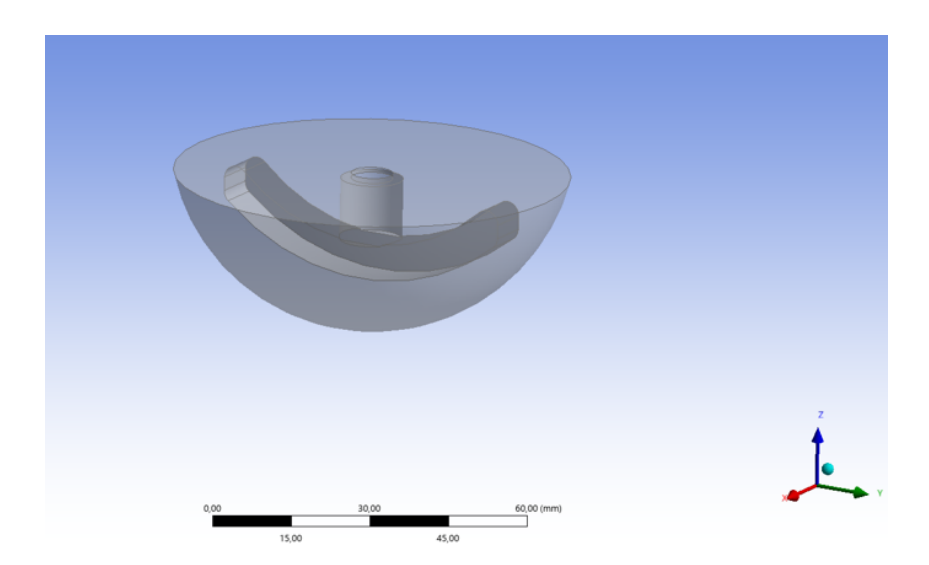


Figure 8. Geometria del reattore TORNADO.

Dalle figure (6)(7)(8) è possibile osservare la geometria creata tramite DesignModeler riproducendo i tre diversi sistemi. A questo punto è stata creata una mesh per ogni reattore ed è stata condotta uno studio sul numero di celle migliore, in modo tale da conciliare velocità delle simulazioni e precisione dei risultati.

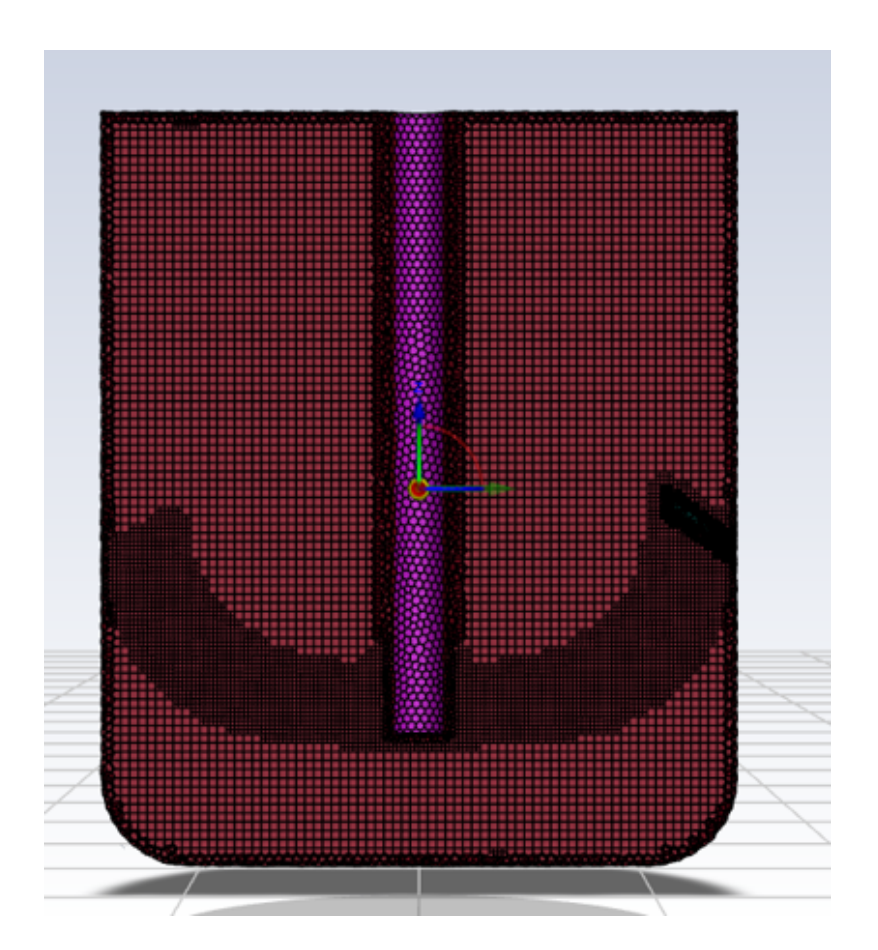


Figure 9. Mesh del reattore IKA con il Paravisc.

Grid Indipendence NonNewtonian Fluid



Figure 10. Grid Independence per fluidi Non Newtoniani $(\tau_0=484.14Pa,k=0.00113Pas^n,n=2.3~[2])$

Come è possibile osservare nella figura (9), è stata utilizzata una mesh di tipo Hexcore. Questa tipologia permette, infatti, la creazione di una mesh di buona qualità anche in geometrie complesse. Dopodichè, si è svolta una Grid Indipendence sia per un fluido Newtoniano e sia per un fluido Non Newtoniano (10).

Utilizzando le modalità descritte nella sezione di validazione del modello, per i tre sistemi è stato possibile calcolare vari parametri fluidodinamici, tra cui la potenza richiesta per l'agitazione, lo shear rate medio, l'intensità di deformazione e le zone stagnanti.

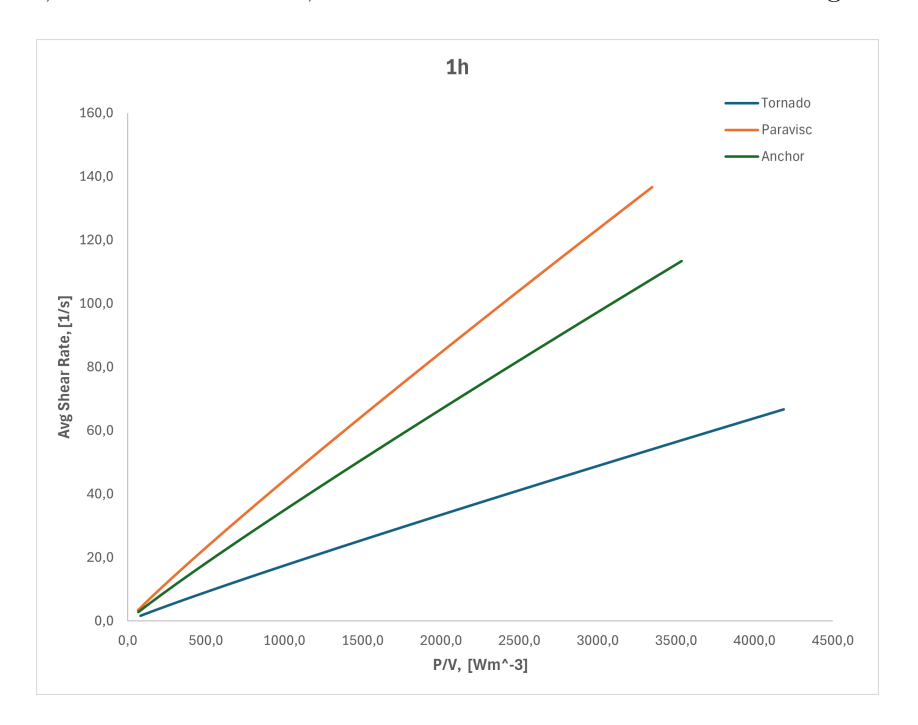


Figure 11. Shear rate medio vs. Power input per unità di volume dopo 1 ora di reazione.

Per esempio, nella figura (11) è stato svolto un confronto tra le varie geometrie sulla base dello shear rate medio all'interno del reattore. Per uno stesso valore di potenza alla girante, all'interno dei diversi reattori avremo valori di shear rate medio molto diversi. Questo può avere una importanza per processi in cui lo shear rate è un parametro critico e permette di scegliere la miglior configurazione.

0.1.5 Correlazione tra agitazione e conversione della biomassa

Durante il lavoro sperimentale è stata evidenziata una possibile correlazione tra la miscelazione del fluido durante la liquefazione e la conversione in glucosio della biomassa. L'ultima parte del lavoro ha avuto, dunque, come obiettivo quello di studiare quale parametro fluidodinamico influenza la velocità di conversione della biomassa. A questo scopo, è stata considerato il sistema IKA Paravisc e la reologia ottenuta con questa configurazione, andando a simulare il reattore per diversi tempi durante la liquefazione. In particolare, maggior importanza è stata data all'inizio della reazione (le prime tre ore) poiché in questo range si è osservato una differenza di velocità di conversione. Per ogni frazione temporale sono stati calcolati i parametri fluidodinamici di interesse, ovvero la potenza richiesta per l'agitazione, lo shear rate medio, l'elongazione media e la percentuale di zone stagnanti. Ciascun parametro ha mostrato una variazione più o meno significativa nelle prime ore di reazione, dimostrando la possibile esistenza di una correlazione tra i suddetti paramentri e la velocità di conversione della biomassa. Questo effetto svanisce man mano che la reazione procede, probabilmente dovuto all'insorgenza di altri fattori che governano il sistema.

Il lavoro sperimentale è stato condotto utilizzato un'unica geometria, ovvero il reattore IKA con il Paravisc come agitatore, mentre la biomassa utilizzata deriva da scarti dell'agricoltura, quali la paglia, pretrattata in precedenza. Gli esperimenti sono stati condotti a tre diverse velocità (50, 100 e 150 rpm) e per ogni ora durante la liquefazione è stato svolto uno studio reologico sul fluido. Da questo si è ottenuta una curva reologica per ogni ora, ovvero la curva shear stress-shear rate. Per ogni ora e per ogni velocità sono stati poi calcolati i parametri reologici per poter implementare la reologia su ANSYS fluent.

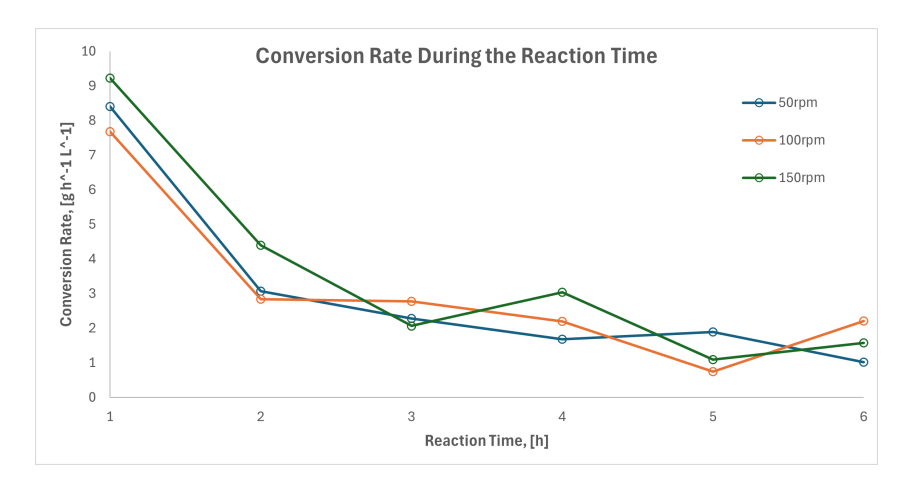


Figure 12. Velocità di conversione della biomassa durante la liquefazione per diverse velocità rotazionali.

La figura (12) rappresenta la velocità di conversione in funzione del tempo di liquefazione per le tre diverse velocità di rotazione.

Durante le prime due ore di reazione è possibile osservare che la velocità di reazione è maggiore nel caso a velocità di reazione maggiore (ovvero 150 rpm), mentre negli altri due casi (50 e 100 rpm) i valori sono simili. Questa differenta di velocità di conversione porta ad una differenza di conversione di glucosio totale al termine del processo e potrebbe essere dovuta all'agitazione.

Durante il lavoro sperimentale è stato utilizzato anche il reattore TORNADO, il quale ha evidenziato una maggior influenza dell'agitazione sulla conversione, ma purtroppo le curve reologiche non erano disponibili. Questo studio, dunque, è solamente un primo tentativo di approccio allo studio di questo fenomeno.

Per ogni ora durante la liquefazione sono stati calcolati i vari parametri fluidodinamici,

in modo tale da poter confrontarne le variazioni nel tempo. I parametri studiati sono la potenza necessaria per l'agitazione, lo shear rate medio, l'intensità della deformazione e la percentuale di zone morte nel reattore.

I vari parametri sono stati poi confrontati con la velocità di conversione in modo tale da riuscire ad osservare quale di questi avesse un impatto sulla conversione e quale non fosse influente.

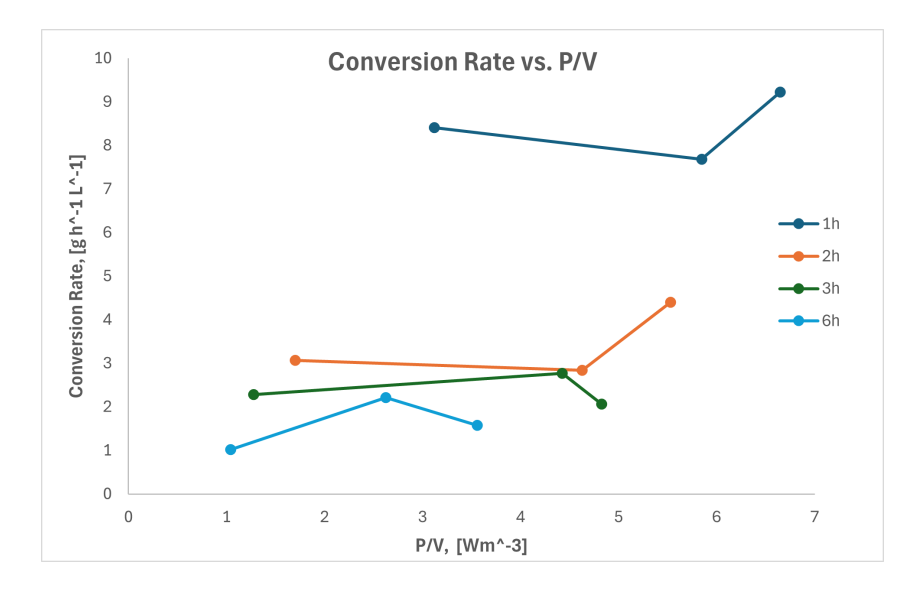


Figure 13. Velocità di conversione vs. Power input per diversi tempi di reazione.

A titolo di esempio, dalla figura (13) è possibile osservare la velocità di conversione di glucosio in funzione della potenza. Nelle prime due ore di reazione è possibile osservare una influenza sulla velocità di conversione aumentanto la potenza fornita alla girante. Questo effetto svanisce con il procedere delle reazione sia per la potenza che per gli altri paramentri fluidodinamici.

Ogni parametro ha dimostrato una sensibilità alla conversione della biomassa nelle prime ore di reazione e questo effetto svanisce con il procedere della reazione. Studiando un solo sistema non è possibile andare a separare il contributo di ogni parametro sulla conversione totale, poichè tutti i parametri sembrano avere un peso sul processo.

0.1.6 Conclusioni

In questo lavoro è stato creato il modello CFD per tre diverse configurazioni reattoristiche utilizzate per l'idrolisi della biomassa. Questi modelli sono stati validati ed in seguito sfruttati per la costruzione della curva Numero di Potenza–Reynolds per ogni sistema insieme al calcolo di importanti parametri fluidodinamici in diverse condizioni operative. Questa tipologia di analisi può essere utilizzata in futuro per uno studio approfondito del processo e per l'ottimizzazione della liquefazione, riuscendo ad ottenere grazie alla CFD parametri impossibili da misurare in laboratorio. Inoltre, è stato svolto un primo tentativo di indagine e identificazioni di parametri critici che potrebbero influenzare la conversione

della biomassa, utilizzando una reologia ottenuta da uno studio sperimentale. Lavorando con un unico set di dati e un singolo sistema non è stato possibile distinguere quali dei parametri abbia un grande impatto sulla conversione, dunque il parametro critico, e quale sia del tutto ininfluente. A questo scopo, è necessario lo studio di più sistemi in condizioni operative diverse. Questa strategia potrebbe portare, in futuro, a identificare quale sia il parametro più influente per la conversione da utilizzare come guida per lo scale up del processo di idrolisi della biomassa.

0.2 Introduction

In recent years, due to the intensification of climate change, the development of new sources of energy has received increasing attention. One of these sources is the production of second-generation (2G) bioethanol, obtained by fermentation of the hydrolysate from lignocellulosic biomass (derived from agricultural waste). In the first step of the process, cellulose is converted into glucose through the action of enzymes. This step is always preceded by a pretreatment of the solids, aimed at facilitating enzymatic hydrolysis. The conversion must be carried out at high solids loading to minimize the amount of water present in the process. The reason for this is to reduce the energy cost of separating water and ethanol in the final stage, making the process more economically advantageous. Due to the high solids loading, the slurry does not exhibit Newtonian behavior, and therefore the liquefaction step may present mixing problems [11]. The difficulties in calculating the rheological parameters of the fluid and in studying the system evolution can be overcome using computational fluid dynamics (CFD). The aim of this work is to develop a CFD model of the reactors where biomass hydrolysis takes place and to extract parameters from the model to identify the liquefaction scale up criteria.

0.3 Lignocellulosic biomass

The composition of lignocellulosic biomass varies according to its origin, and this will impact the composition of the slurry in the reactor leading to a different yield of bioethanol. Despite of those differences, the lignocellusosic biomass is always composed by three main group of components: cellulose, hemicellulose, lignin. [9]

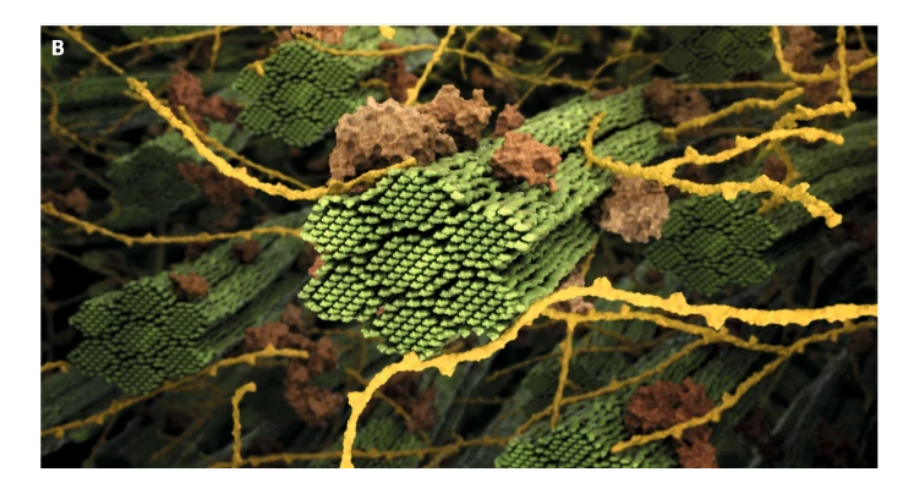


Figure 14. Structure of lignocellulosic biomass. [9]

0.3.1 Cellulose

Cellulose is the most abundant natural polymer on Earth. It is a homo polysaccharide composed of repeating cellobiose units, each consisting of two glucose molecules. In

biomass, cellulose occurs in both crystalline and amorphous regions. The crystalline structure significantly limits enzymatic conversion, as its tightly packed arrangement hinders enzyme accessibility to the glucose units. Cellulose can be depolymerized into cellobiose and glucose either through enzymatic action or by treatment with strong acids. [9]

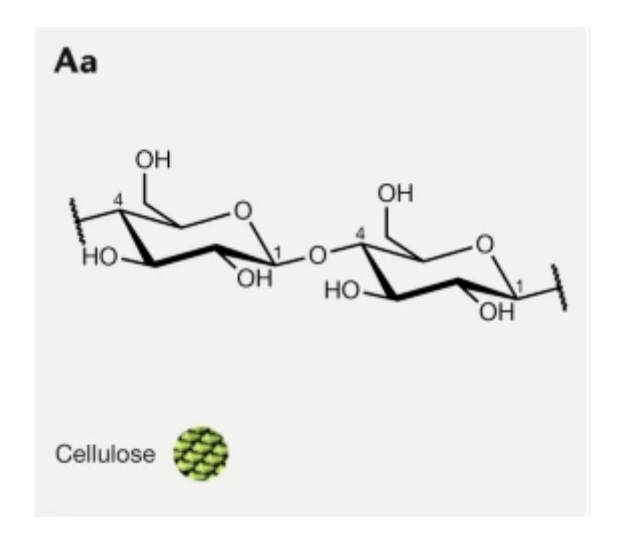


Figure 15. Scheme of the structure of cellulose. [9]

0.3.2 Hemicellulose

Hemicellulose is a heterogeneous polysaccharide composed of different sugar units, including d-glucose, d-galactose, d-mannose, d-xylose, l-arabinose, dglucuronic acid, and 4-O-methyl-d-glucuronic acid. This Heterogeneity leads to a more amorphous structure than the cellulose, which make hemicellulose easier to hydrolyze. The content of hemicellulose in lignocellulosic biomass can range from 20-35%. [9]

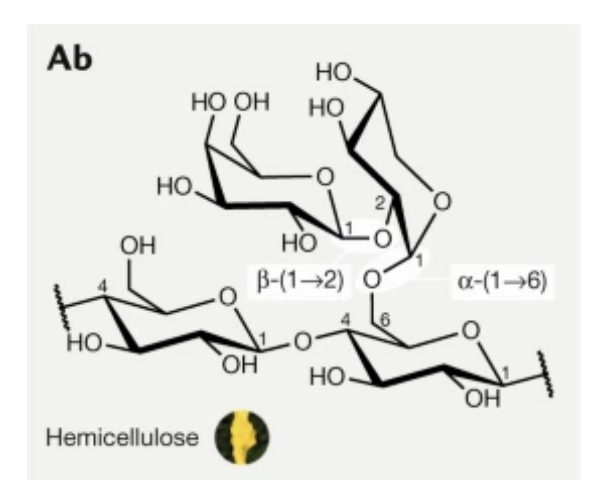


Figure 16. Scheme of the structure of hemicellulose. [9]

0.3.3 Lignin

Lignin, the main non-polysaccharide component of lignocellulose, is formed by the polymerization of phenylpropane units and is a complex, amorphous polymer that imparts rigidity and hydrophobicity to plant cell walls. Lignin acts as a barrier, protecting cellulose and hemicellulose from enzymatic degradation. As a result, higher levels of lignin make it more difficult to hydrolyses the biomass. [9]

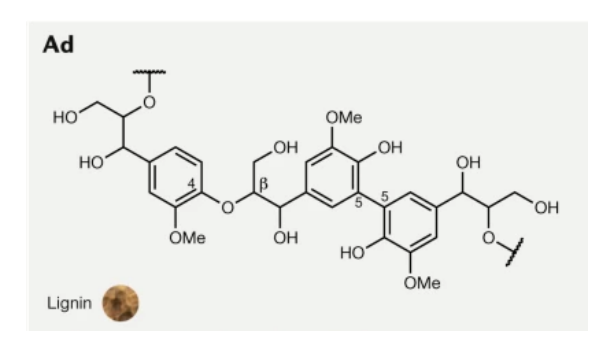


Figure 17. Scheme of the structure of lignin. [9]

0.4 Process Overview

Enzymatic hydrolysis of lignocellulose has long been studied as a method to convert biomass into fermentable sugars (glucose) for subsequent bioethanol production, with more recent attention focused on high solid loadings, as this approach makes the process more economically feasible. The process is composed by four parts (Figure 18): Pretreatment, Hydrolysis, Fermentation and Distillation. [7]

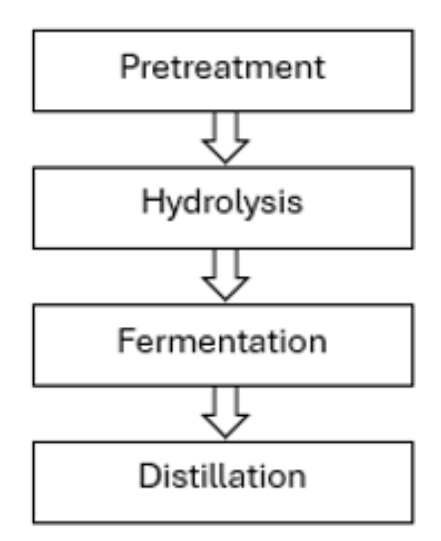


Figure 18. Block diagram of the process

The pretreatment part is used for increasing the availability of the cellulose for enzymatic hydrolysis. In fact, in nature the cellulose is disposed in a complex path of hemicellulose and lignin and without those treatment the hydrolysis will be less effective. The pretreatment can be either mechanical or thermochemical and it has also the aim to reduce the size of the particles that make up biomass pretreated.

The second step is the cellulose conversion into fermentable sugars, like glucose, using the enzymatic hydrolysis. Compared to chemical conversion, the enzymatic conversion of cellulose in more effective, highly selective and could reach higher yield.

After the Hydrolysis the fluid undergoes to the fermentation part, where the fermentable sugars are converted to bioethanol by using the metabolic activity of Saccharomyces cerevisiae. There are two different set up for this part: it can be done in the same reactor of the hydrolysis (SSF, Simultaneous Saccharification and Fermentation) or it can be done in a different one (SHF, Separate Hydrolysis and Fermentation).

The last step is the Distillation section, necessary for extract ethanol from the fluid and to separate it from the water. It is useful to do a pre-step for the separation of the formation residue, which can contain suspended matter like lignin. [7]

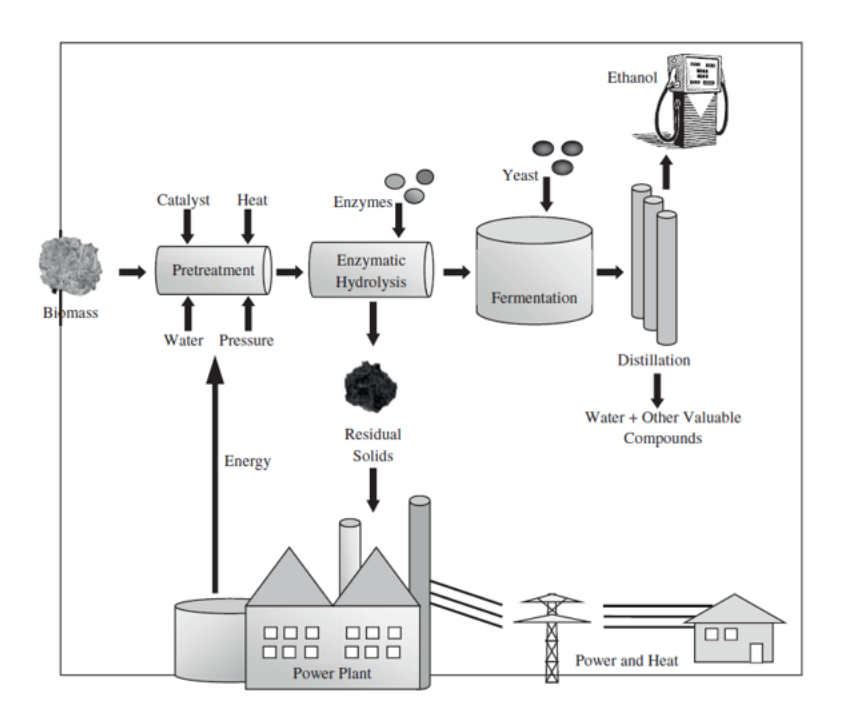


Figure 19. Scheme of the total process [7]

Distillation is usually more economical when the ethanol concentration is around 4% (w/w) and for obtaining it is necessary to have a solid loading around 20% (w/w) in the hydrolysis part, so it is convenient to work with a little amount of water, leading also to the possibility to have smaller equipment.

The lack of water has also a negative aspect for enzymatic hydrolysis because of the mass transfer and the lubricity. Firstly, water increases the effectiveness of the reactions providing a medium for solubilizing the enzymes and improve the mass transfer of products and reagents. In addition, water reduces the viscosity of the slurry by increasing the lubricity of the particles, resulting in a reduction of the shear stress necessary mix the fluid, allowing lower power input in the reactor. As solids loadings approach 20% (w/w), the liquid fraction becomes fully absorbed into the biomass, leaving little free water and the apparent viscosity of the mixture increases; consequently mixing and handling of material become more difficult. [7]

0.5 Computational Fluid Dynamics and Governing Equation

Modeling a stirred tank using computational fluid dynamics (CFD) requires consideration of many aspects of the process.

Any computational model requires the creation of a computational grid, composed by numerous cells, for the description of the volume occupied by the fluid inside the vessel (domain). In these cells the problem-specific variables are computed and stored. The

computational grid must fit the contours of the vessel and its internals, even if the components are geometrically complex.

Numerical simulations of stirred tanks are normally done in either two or three dimensions. In three dimensional (3D) simulations the impellers can be modeled using its exact geometry.

The difficulties in these type simulations is to incorporate the motion of the impeller in the presence of the stationary tank. For this purpose, a single rotational frame (SFR) approach was used in this work for take into consideration the motion of the impeller relative to the tank walls. [8]

0.5.1 Conservation Equation

If an element of fluid in motion is considered, two changes to the element will probably take place:

- the fluid element will translate and rotate in space;
- the fluid will become distorted, either by a simple stretching along one or more axes or by an angular distortion that causes it to change shape.

The process of translation is often referred to as "convection", and the process of distortion is related to the presence of gradients in the velocity field and a process called "diffusion". In more complicated systems, sources can also be present that give rise to additional changes in the fluid. Many processes, including those involved in the description of generalized fluid motion, are governed by a set of conservation or transport equations. These equations describe how the fluid changes over time as a result of convection, diffusion, and sources of the conserved or transported quantity. Moreover, these equations are coupled, meaning that variations in one variable can induce changes in other variables. [8]

Continuity

The continuity equation involve the conservation of mass. For obtain its mathematical expression, consider the flow of a fluid of density ρ through the six faces of a rectangular block, as shown in Figure 20. The block has sides of length Δx_1 , Δx_2 , Δx_3 and velocity components U_1 , U_2 , U_3 for each coordinate directions. [8]

To ensure conservation of mass, the sum of the mass flowing through all faces must be zero:

$$\rho(U_{1,out} - U_{1,in})(\Delta x_2 \Delta x_3) + \rho(U_{2,out} - U_{2,in})(\Delta x_1 \Delta x_3) + \rho(U_{3,out} - U_{3,in})(\Delta x_1 \Delta x_2) = 0$$
(3)

Dividing by the control volume $\Delta x_1 \Delta x_2 \Delta x_3$ is possible to obtain:

$$\rho(\frac{U_1}{\Delta x_1} + \frac{U_2}{\Delta x_2} + \frac{U_3}{\Delta x_3}) = 0 \tag{4}$$

In a more compact form and specify the term for the density variation in time:

$$\frac{\partial \rho}{\partial t} + \rho \frac{\partial U_i}{\partial x_i} = 0 \tag{5}$$

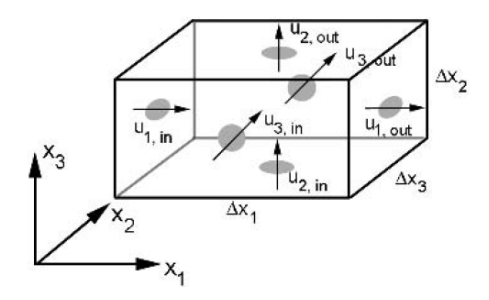


Figure 20. A rectangular volume with inflow and outflow [8].

Momentum

The momentum equation is a statement of conservation of momentum in each of the three component directions. The three momentum equations are collectively called the NavierStokes equations. In addition to momentum transport by convection and diffusion, several momentum sources are also involved:

$$\frac{\rho U_i}{\partial t} + \frac{\rho U_i U_j}{\partial x_j} = \frac{\partial p}{\partial x_i} + \frac{\partial \left[\mu \left(\frac{\partial U_i}{\partial x_j} + \frac{\partial U_j}{\partial x_i} - \frac{2\partial U_k}{3\partial x_k} \delta_{ij}\right)\right]}{\partial x_j} + \rho g_i + F_i \tag{6}$$

In the equation above the convection terms are on the left, while on the right-hand side are the pressure gradient the divergence of the stress tensor, which is responsible for the diffusion of momentum, the gravitational force and other generalized forces (source terms), respectively. [8]

0.5.2 Solution Strategies

For complex system, like this one, there is an high degree of coupling between the momentum equation and the rotational terms. This could lead to instabilities in the solution process.

With the simulation involving high rotational velocities, the calculation was started at low rotational speed, around 10% of the actual operating condition. Then the problem was solved and the data saved. After that, the rotational speed was increased and the calculation was started again without initialization. This operation was repeated until the actual rotational speed was reached for give more stability to the solution. [8]

Under-relaxation Factor

Another way used in this work to ensure more stability to the solution with high rotational speed was to reduce the under-relaxation factor for the velocities, from 0.5 to 0.3. But then, with low rotational speed and with better knowledge of the system, was possible to increase the pressure factor to 0.6 for obtain a faster convergence.

For better understand what a under-relaxation factor does, is important to know that the solution of a single differential equation is solved iteratively, makes use of information from

the preceding iteration. If ϕ_n is the value of the variable from the preceding iteration and ϕ_{n+1} is the new value, some small difference or change in the variable brings the variable from the old value to the new one:

$$\phi_{n+1} = \phi_n + \Delta\phi \tag{7}$$

Rather than use the full computed change in the variable, $\Delta \phi$, it is often necessary to use a fraction of the computed change when several coupled equations are involved:

$$\phi_{n+1} = \phi_n + f\Delta\phi \tag{8}$$

f is called under relaxation factors and typically range from 0.1 to 1.0, depending on the complexity of the flow physics, the variable being solved, the solution method being used, and the state of the solution. Underrelaxation makes the convergence process stable, but slower. As the solution converges, the underrelaxation factors should be raised to ensure convergence that is both rapid and stable at all times. [8]

0.5.3 Numerical Diffusion

Numerical diffusion is another a source of error that is always present in finite volume CFD, highlighting the fact that approximations are made during the process of discretization of the equations.

It is so named because is acts like an equivalent increase of the diffusion coefficient. In this case, during the solution of the momentum equation, the fluid will appear more viscous.

To minimize numerical diffusion is useful to use a higher order discretization scheme or build a grid that minimize the effect. Numerical diffusion is usually less of a problem with quadrilateral or hexahedral meshes, provided that the flow is aligned with the mesh. [8]

0.5.4 Rotating Frame Motion

The model used to describe the reactor in this work is the Rotating Frame Motion. It solves the momentum equation for all the domain in a rotating frame using the angular velocity of the primary rotating component (the impeller), Ω , as the angular velocity of the frame. The tank, however, rotates in the opposite direction, so must have a rotational boundary condition of $-\Omega$ or an absolute velocity of zero. This approach can be use only if there are not buffed in the reactor and if the walls are a surface of revolution.

0.5.5 Simulation and Boundary Conditions

All simulations were performed on a computing cluster to reduce computational time. The cluster was equipped with AMD Genoa 9534 processors, and the average runtime per simulation was on the order of a few minutes, depending on the rheological properties of the fluid.

The rotating reference frame introduce the centrifugal and Coriolis forces into the Navier Stokes equation. The fluid domain is set in rotational motion and the impeller in moving along the domain. The reactor wall are set as stationary, with a absolute velocity of zero.

For both the reactor wall and the impeller surface are used the no slip condition. The upper surface is set as free of shear stress.

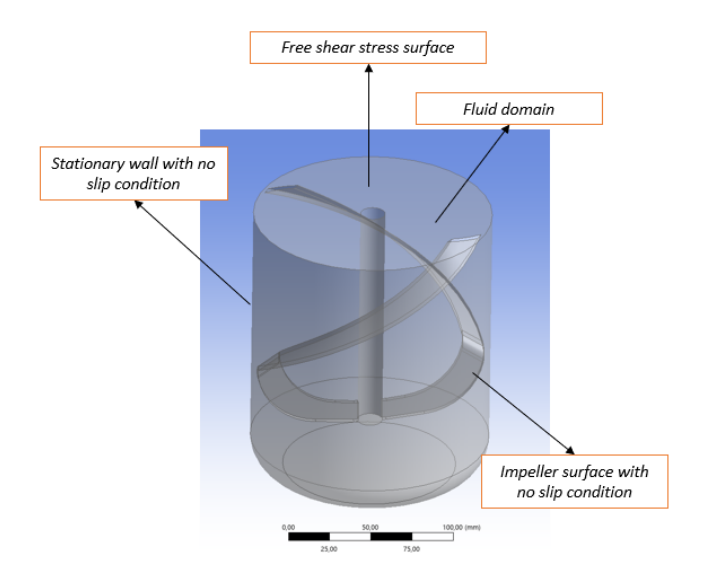


Figure 21. Example of boundary conditions used in this work.

0.6 Non-Newtonian fluids and Rheological Models

Fluids with Non-Newtonian behavior have viscosity that depend on the shear rate and it can be described by many laws that involve the local shear rate of the fluid in different ways according to the model.

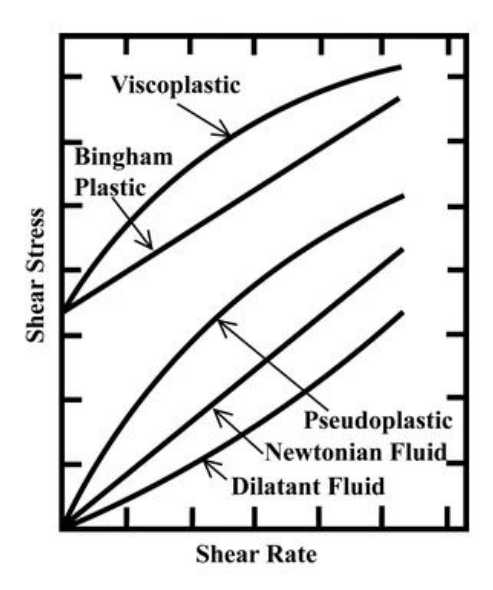


Figure 22. Curves for different type of Non-Newtonian fluids. [3]

In some cases, a fluid will transition from non Newtonian to Newtonian behavior after a threshold stress has been exceeded and they are called shear thinning fluids, exhibiting a drop of viscosity in regions of high shear.

For computational fluid dynamics, the consequence of non-Newtonian flow modeling is that the viscosity, a fluid property, becomes coupled to the fluid motion, making the equation set more difficult to solve.

In this work has been used two different model: the Power Law and the Herschel Bulkley model for modeling the rheology of the biomass slurry, because its ability to take in account the yield stress.

The equations are the following ones:

$$\tau = k \left(\dot{\gamma}\right)^{n-1} \tag{9}$$

For the Power Law, where K is called consistency index $[Pas^n]$ and n is the flow index [-]

$$\dot{\gamma} = 0 \quad \text{if} \quad \tau < \tau_0 \tag{10}$$

$$\tau = \tau_0 + k \left(\dot{\gamma}\right)^n \quad \text{if} \quad \tau \ge \tau_0 \tag{11}$$

This is the Herschel Bulkley model, is more complex compared to the Power Law but is better for modeling the biomass slurry rheology, thanks its ability to take in account the yield stress.

 γ is the shear rate, k is the consistency index,n the flow index and τ the shear stress. The rheological parameters of both models where calculated thanks to the rheological experiments conducted in the IFPEN laboratories. The viscosity of the slurry is also a function of the time and with the CFD model was possible to make a model of the reactor for each time during the Hydrolysis.

0.6.1 Biviscosity Model

The Herschel Bulkley model is difficult to simulate because of the yield stress and during the mixing this lead to zones with a velocity equal to zero, acting as a solid. So, when the shear rate is very low, the viscosity calculated with the model could be very high and this could cause some problem in the convergence of the solution calculated with the software

For overcome this problem, FLUENT use the biviscosity model. The fluid at low speed acts as a very viscous fluid with viscosity equal to μ_{yield} , that is possible to insert in the options. At high shear rate the fluid respect the classic Herschel Bulkley model. [2]

$$\mu = \mu_{yield} \quad \text{if} \quad \dot{\gamma} < \frac{\tau_0}{\mu_{yield}}$$
 (12)

$$\mu = \frac{\tau_0 + k[\dot{\gamma}^n - (\frac{\tau_0}{\mu_{yield}})^n}{\dot{\gamma}} \quad \text{if} \quad \dot{\gamma} \ge \frac{\tau_0}{\mu_{vield}}$$
(13)

0.7 Power Number

Is possible to estimate directly the power necessary for the rotation of the impeller from torque data, T, that can be obtained from CFD simulation or from laboratory measurements. [10]

From torque data is possible to calculate the power required:

$$P = 2\pi NT \tag{14}$$

Where P is the power required for the agitation, expressed in [W], T in the torque in [Nm] and N is the rotational speed in $\left[\frac{1}{s}\right]$.

Now is possible to calculate the Number of Power, Np, as follow:

$$Np = \frac{P}{\rho N^3 D^5} \tag{15}$$

Where D is the impeller diameter and ρ is the density.

As shows in the work of Furukawa et al. [4] and in the Hand Book of Industrial Mixing [8], there is a correlation between Np and the Reynolds number, and it depends on the geometry of the impeller.

$$Re = \frac{\rho ND}{\mu} \tag{16}$$

Where μ is the viscosity of the fluid.

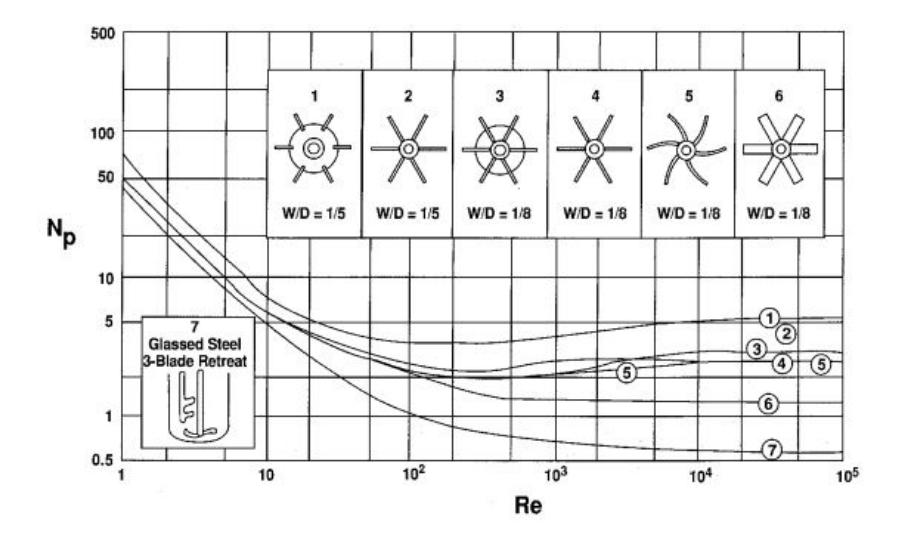


Figure 23. Power Number versus Reynolds Number for different type of impellers. [8]

At low Reynolds numbers (< 10 - 20) the correlation between Np and Re is linear, with a negative slope.

$$Np \propto Re^{-1} \tag{17}$$

This correlation is true for any type of fluids, Newtonian or Non-Newtonian. For the Newtonian fluids it can be defined a constant called Power constant, B, that depends only on the geometry of the impeller.

$$Np = \frac{B}{Re} \tag{18}$$

Also for the Non Newtonian fluids is possible to define a similar Reynolds number, called Re_{app} , based on an apparent viscosity μ_{app} , defined as the viscosity of the Newtonian fluid that needs the same amount of power for the agitation.

$$\mu_{app} = \frac{P}{BN^2D^3} \tag{19}$$

Where B is the Power constant of the impeller calculated with the Newtonian fluids.

$$Re_{app} = \frac{\rho DN^2}{\mu_{app}} \tag{20}$$

These definition are very useful for the calculation of the Metzner Otto constant. [12]

0.8 Metzner e Otto Constant

The study of mixing non-Newtonian fluids can be very challenging due to their complex behavior, as the viscosity varies with the shear rate. Consequently, it is impossible to know the exact shear rate throughout the tank during mixing. One of the most widely used methods to address this issue is known as the Metzner Otto concept [6]. The basic idea is to consider an average shear rate for calculate an apparent viscosity.

$$\dot{\gamma}_{eff} = K_s N \tag{21}$$

Where K_s is the Metzner Otto constant, N is the rotational speed and $\dot{\gamma}_{eff}$ is the average shear rate. The K_s depends only on the geometry of the impeller, on the rheology of the fluid and poorly on the mixing regime. It can be estimated with the measure of the torque obtained from CFD simulation.

As shows in the work of Tanguy et al. [12], there are many strategies that can be follow to obtain the Metzner & Otto constant and they will be explained in the next section.

0.9 Model Validation

In this section, model validation was performed by selecting a relevant paper from the literature on a similar topic and reproducing both the geometry and the reported results. The aim is to develop a validated model that provides confidence in the CFD results. For this part has been choose the paper of Carvajal et al. [2] and has been tried to reproduce the the model with the experimental results, using Netonian fluid and also a Non Newtonian fluid.

To create a similar geometry, necessary to reproduce the torque results, the images in the paper were digitized. Using these images along with the basic reactor dimensions provided in the study, it was possible to create a geometry closely approximating the real reactor.

Dimensions	[m]
Diameter of the impeller	0.145
Diameter of the tank	0.150
Clearance	0.0025
High of the tank	0.127

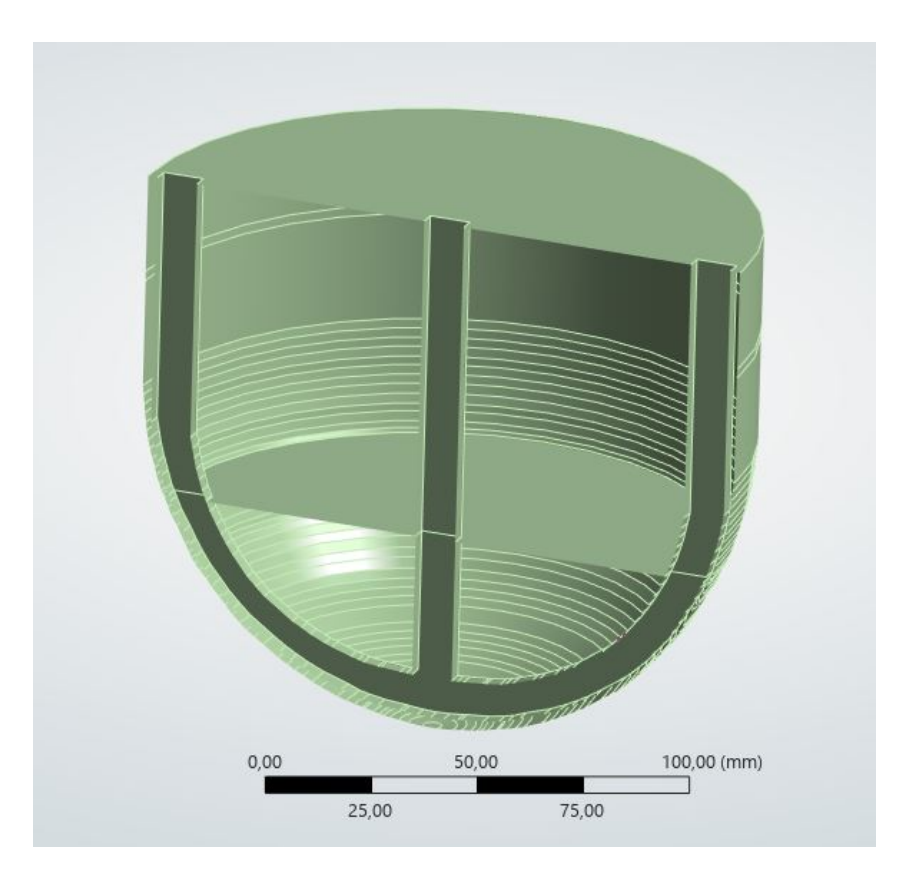


Figure 24. Tank geometry of Carvajal et al. [2]



Figure 25. Mesh used for the model validation section.

For obtain a similar mesh to the one used by Carvajal et al. was necessary to divided the tank in two zone for isolating the bottom part because is more complex and the program was not able to create a mesh with good quality in the all tank. With this method was possible to force the creation of hexahedral cells in the middle and near the top of the tank, while in the bottom were generated tetrahedral cells. The average qualities of the mesh were:

Element Quality	0.874
Skewness	0.143
Orthogonal Quality	0.890

Generally, a good mesh has value of Orthogonal Quality above 0.1 and values of Skewness under 0.95.

Once the mesh was done, it was possible to conduct simulation with the same fluids used in the paper. Carvajal et al. [2] used pure glycerin at 36 Celsius degree to validate their model by measuring the torque directly in laboratory experiments. From their study, torque values at different velocities were extracted and subsequently compared with those obtained from CFD simulations using the digitized model.

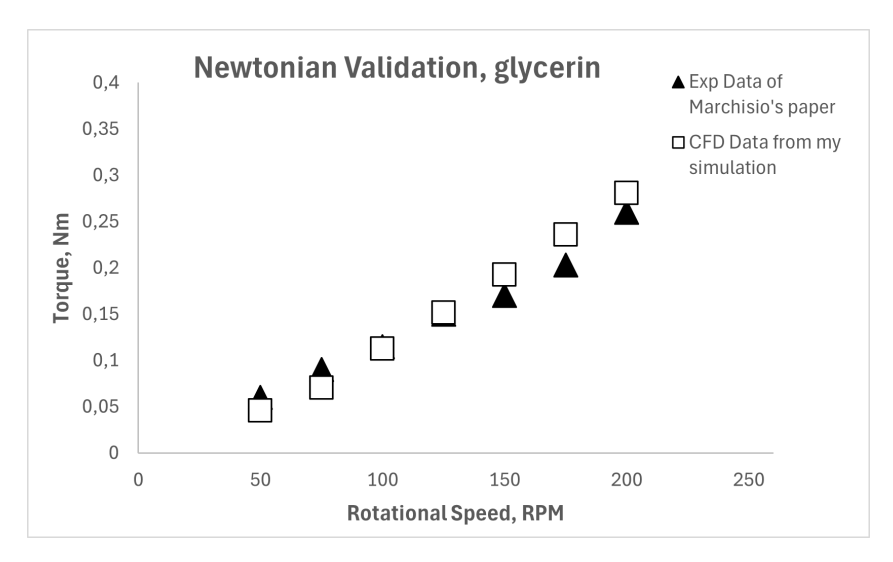


Figure 26. Value of experimental torque measurements (triangles) and values of torque obtained via CFD. The fluid used was Glycerin at 36 Celsius degree, $\mu=0.37 Pas.$ [2]

As it is possible to observe from the graph (Fig. 26 there is good agreement between experimental data and CFD results. The error rage is between 1% - 20%. After the Newtonian Validation, other simulation with other Newtonian fluids have been conducted with the aim to calculate the Power Constant of the impeller, B. In literature is possible to find many way to estimate the constant [12] for many type of impeller. The procedure used in this work is the following:

- Simulations with different Newtonian Fluid in the laminar regime (Re < 10 20).
- Calculation of the Power needed for the agitation, P, and the Power Number Np, from Torque values.
- Creation of the Np-Re graph and calculation of the Power Constant, B.
- Simulations with two Non-Newtonian fluids, modeled with the Power Law model and extraction of Torque values.
- Calculation of the apparent viscosity, μ_{app} , and the Apparent Reynolds Number, Re.
- Eventually, calculation of the Metzner Otto constant.

The constant can be estimated by the simulation with Newtonian fluid and by Non-Newtonian fluid and is important to conduct the simulation in the laminar regime (Re<10-20). The reason is in this zone the power number depends linearly by the Re, like show before (18). Three different Newtonian fluids were simulated with different viscosity. The data of the glycerin was found in the work of Carvajal et al. [2], while the other properties for the other fluids were found in the work of Jain et al. [5]

Fluid	Viscosity, [Pas]	Density, $\left[\frac{kg}{m^3}\right]$
Glycerin	0.37	1260
Polyglicerin	27.04	1279
Starch Syrup	6.7	1389

The simulations were carried out at six different velocities, ranging from 5 to 10 rpm, in order to ensure laminar flow conditions. The Reynolds number varied between 0,01 and 12. From the results, the torque was measured and used to calculate both the power required for agitation and the power number. Knowing the Reynolds number, it was also possible to build the logarithmic Np-Re graph.

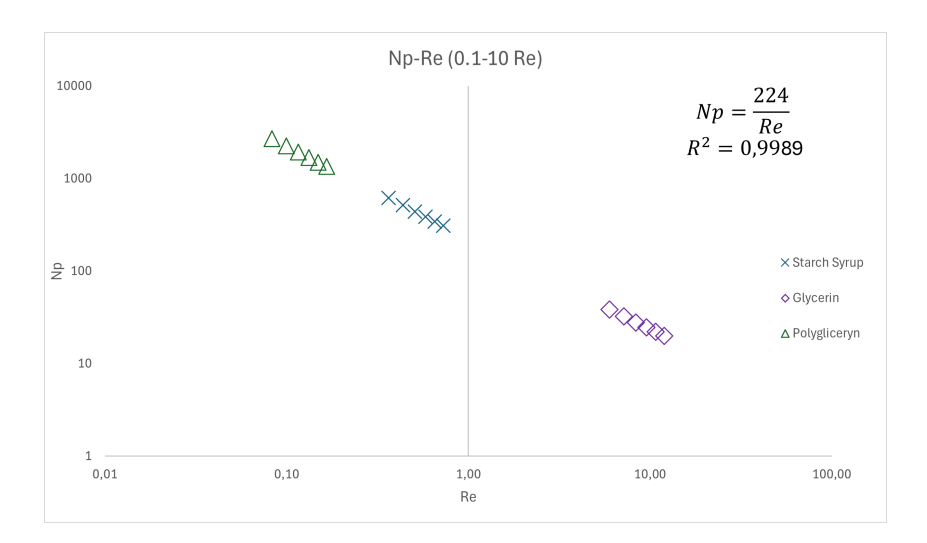


Figure 27. Np vs Reynolds. The data follow a straight line with a negative slope.

From this graph (Figure 27), it is possible to determine the power constant. The linear approximation fits the data very well, with errors ranging between 1% - 5%. For the different fluids the constants were very close to each other.

-	Power Constant, B
Glycerin	232
Polyglicerin	224
Starch Syrup	224

The values are consistent with each other, and the small difference between the one calculated with the glycerin should attributed to the fact that the numbers of Reynold are closer to the limit.

Then, two Non Newtonian fluids modeled with Power Law model have been choose: hydroxyethyl cellulose polymer solution with different concentrations. [5]

Power Law Model	$k, [Pas^n]$	n, [-]
HEC 1.75 %	4.91	0.68
HEC 2.00 %	7.9	0.65

The simulations were conducted with the same range of velocities as before and then the values of the torque on the impeller were extracted from the results. The apparent viscosity and the apparent Reynolds number were calculated with (19)(20).

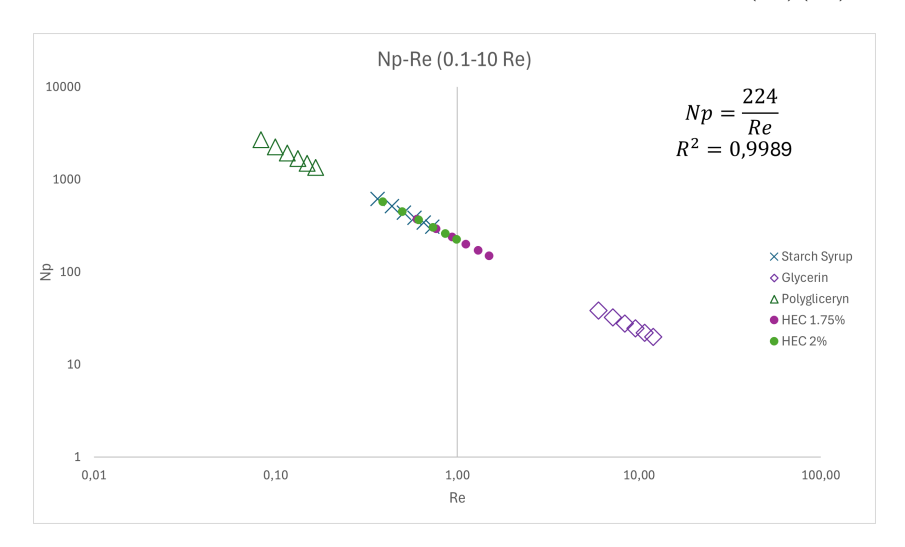


Figure 28. Np vs Reynolds with the value of Power Number and Apparent Reynolds of Non-Newtonian fluids.

After the calculation of the Apparent Reynolds, it was possible to calculate directly the Metzner Otto constant from the following equation [12]:

$$Ks = \left(\frac{kRe_{app}}{\rho N^{2-n}D^2}\right)^{\frac{1}{1-n}} \tag{22}$$

The values of Metzner Otto constant obtained from (22) are the following:

Metzner & Otto Constant	Ks
HEC 1.75 %	60
HEC 2.00 %	59

After the calculations of the Metzner Otto constant, it was possible to implement the Herschel Bulkley model and start the Non Newtonian Validation. The experimental data and the model parameters were obtained directly from the work of Carvajal et al. [2]. The laboratory tests were conducted with two different fluid with different concentrations of solids, $27.5\% \frac{w}{w}$ and $18.5\% \frac{w}{w}$. Then, the enzymes were inserted in the fluid for starting the reaction. At four different time points, the rheological properties of the slurry were measured, and the Herschel Bulkley parameters were determined. The results are presented below:

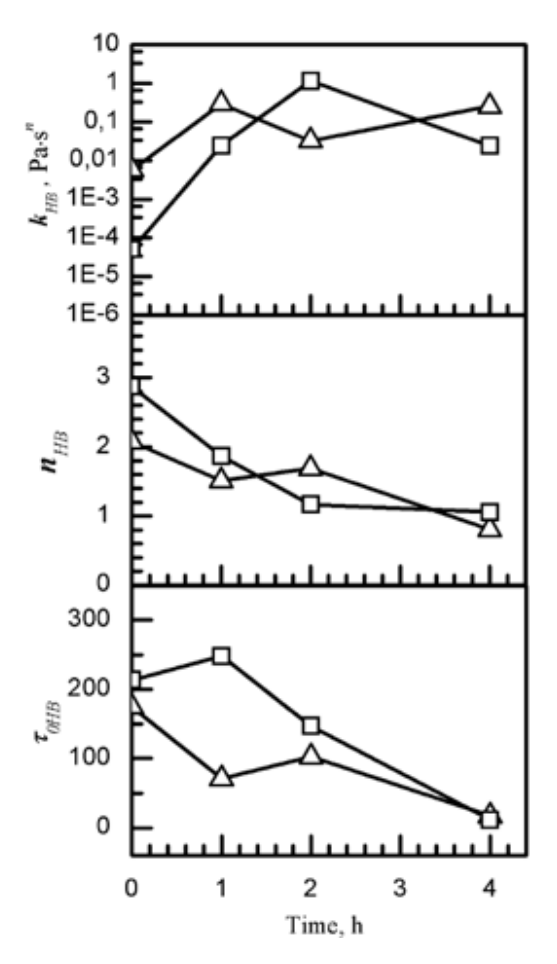


Figure 29. Herschel Bulkley parameters trough the step of Liquefaction. The square referee to $27.5\&\frac{w}{w}$ of initial concentration of solids and the triangles referee to $18.5\&\frac{w}{w}$ of initial concentration of solids

Two times have been chosen, 1h and 2h, and from the graphs have been extracted the values of the Herschel Bulkley parameters and the values of the Torque calculated via experiments. Then, the values were compared to the values of the torque calculated via CFD.

Solid Load and Reaction Time	$ au_0, [Pa]$	$k, [Pas^n]$	n, [-]
$27.5\% \frac{w}{w}, 1h$	250	0.015	1.9
$27.5\% \frac{w}{w}, 2h$	150	1	1.2
$18.5\% \frac{w}{w}, 1h$	75	0.0258	1.5
$18.5\% \frac{w}{w}, 2h$	100	0.0242	1.65

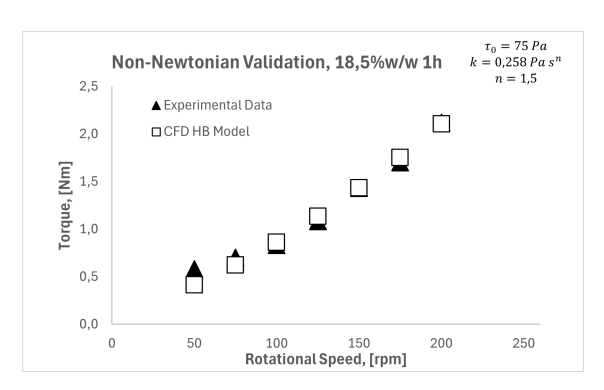


Figure 30. Comparison between torque values calculated via CFD and by Experiments for $18.5\% \frac{w}{w}$ of solids afters one hour of reaction

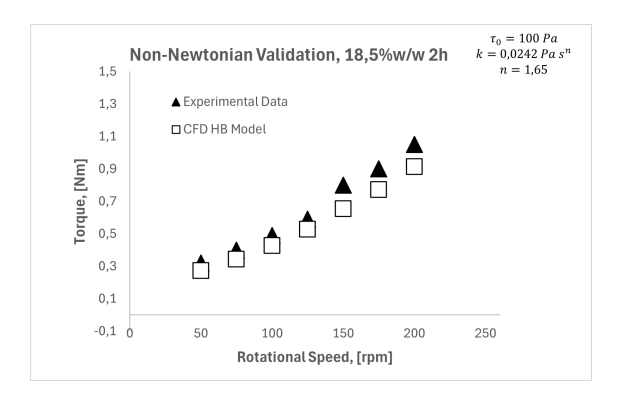


Figure 31. Comparison between torque values calculated via CFD and by Experiments for $18.5\%\frac{w}{w}$ of solids afters two hours of reaction

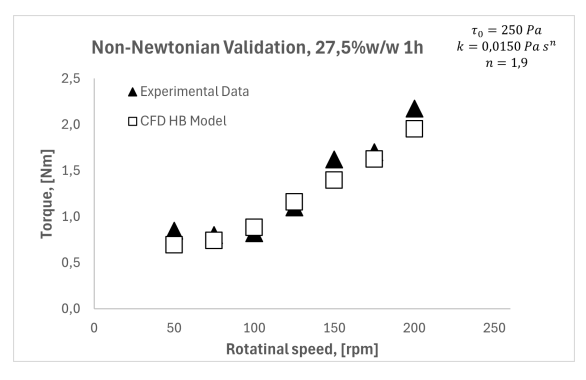


Figure 32. Comparison between torque values calculated via CFD and by Experiments for $27.5\% \frac{w}{w}$ of solids afters one hour of reaction

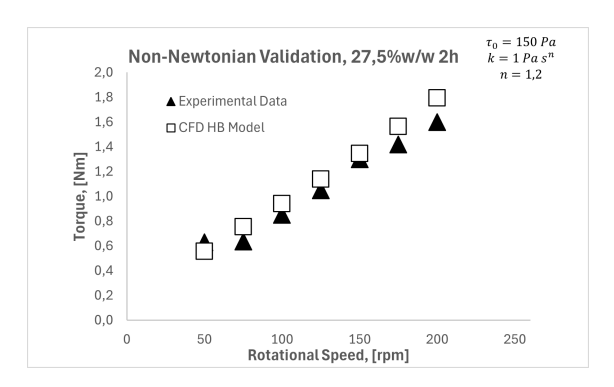


Figure 33. Comparison between torque values calculated via CFD and by Experiments for $27.5\% \frac{w}{w}$ of solids afters two hours of reaction

From the graphs (Figures 30, 31, 32, and 33), it can be observed that there is good agreement between the experimental data and the values obtained from the CFD simulations. The errors between the different value are approximately in the range 1% - 25%. Afterwards, the velocity profile inside the tank was extracted for different impeller speeds. To better understand the behavior of the Herschel Bulkley fluid, a comparison was made with a Newtonian fluid having a viscosity similar to the apparent viscosity of the non-Newtonian fluid. The data points were selected along two lines: one at the center of the tank and the other near the bottom of the impeller. The results were then plotted to highlight the differences between the two fluids.

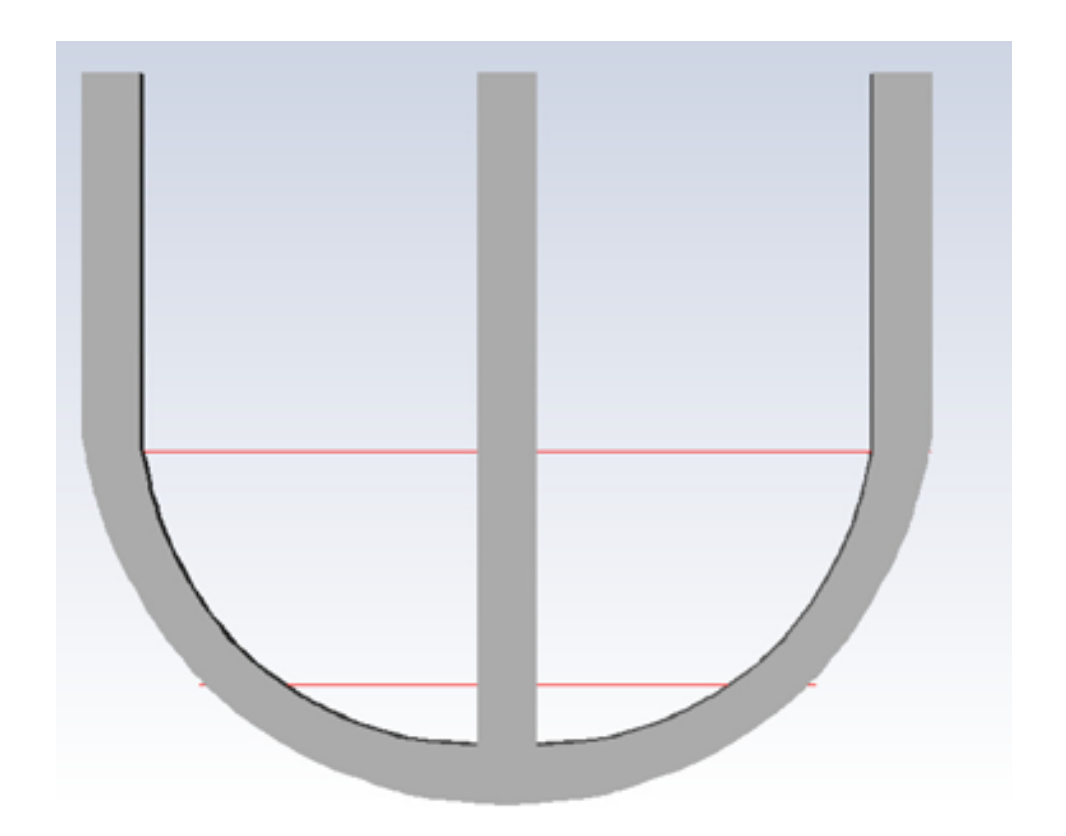


Figure 34. Lines at different height.

The Non Newtonian fluid used was $27.5\% \frac{w}{w}$ after 1h of reaction. The apparent viscosity has a value of about 7.66[Pas], while the Newtonian fluid has a viscosity of 6.7[Pas]. The profiles of the velocity magnitude are show below.

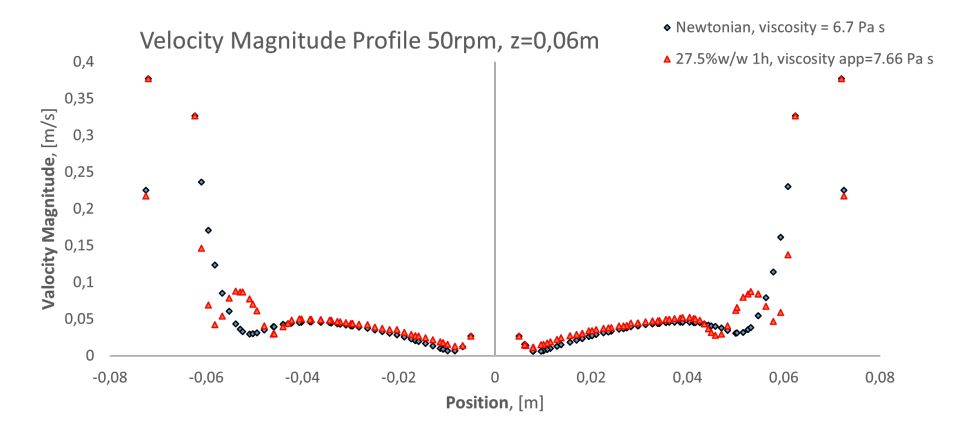


Figure 35. Velocity Magnitude Profile at z = 0.06m

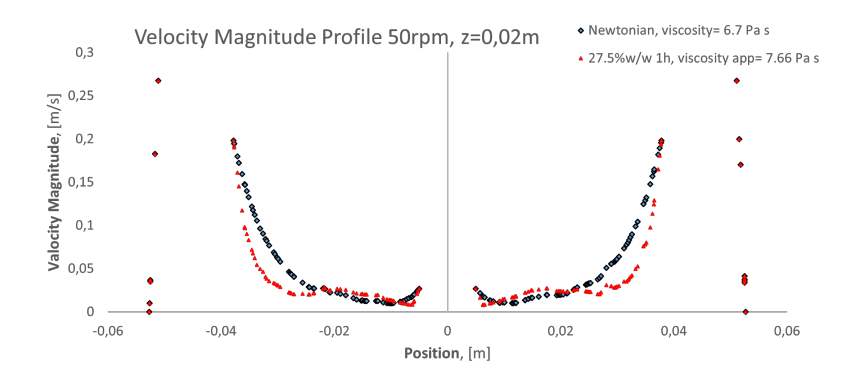


Figure 36. Velocity Magnitude Profile at z = 0.02m

The profile shows a similar behavior of the fluids near the impeller because the velocity are higher. In the middle of the tank the behavior of the Herschel Bulkley is more complex than the one of the Newtonian fluid.

It was also possible to plot the velocity vectors inside the tank during the agitation, for highlight the main flow of the fluid and it direction.

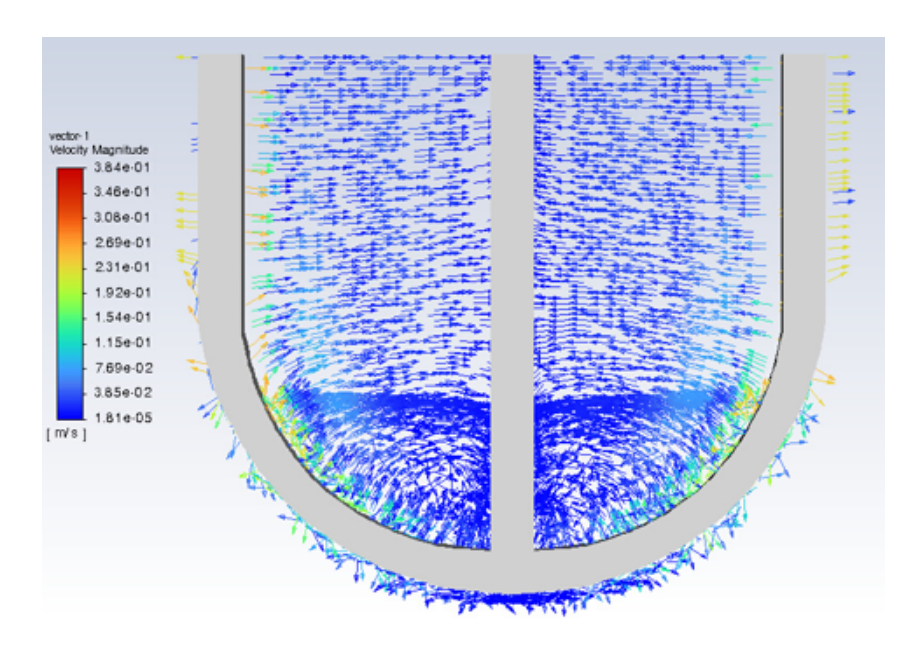


Figure 37. Vectors of velocity $27.5\% \frac{w}{w}$ after 1h of reaction at 50rpm

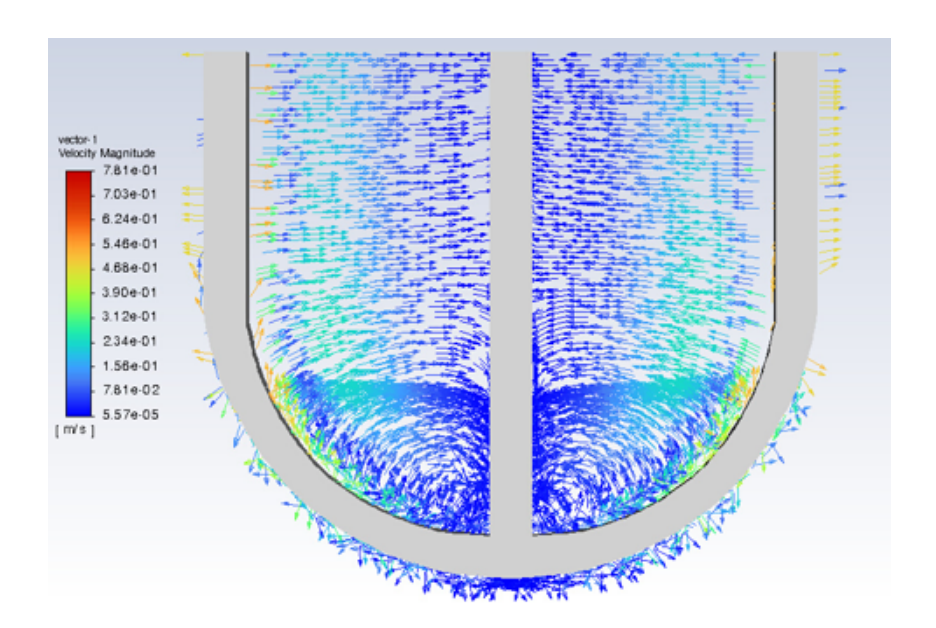


Figure 38. Vectors of velocity $27.5\% \frac{w}{w}$ after 1h of reaction at 100rpm

For better show the difference in the value of the strain rate in the tank, it was necessary to change the range of it. Near the impeller the strain rate is very high, while in the middle is very low. Removing the higher value and set the maximum to $175[\frac{1}{s}]$ it was possible to obtain a better resolution of the contours.

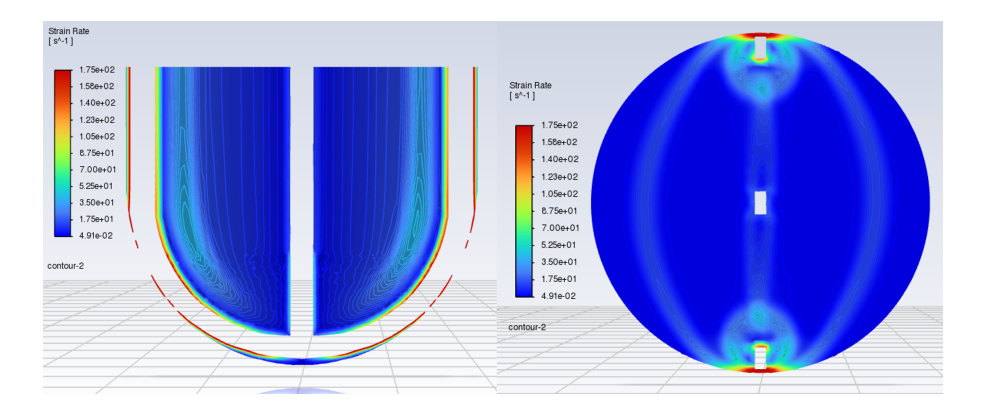


Figure 39. Strain Rate Contours at 50rpm

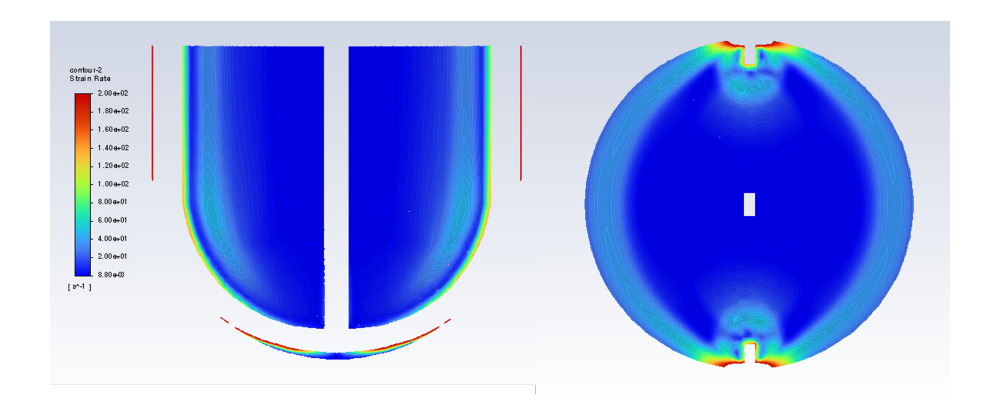


Figure 40. Strain Rate Contours at 100rpm

Another important parameter to estimate is the elongational stress imparted by the impeller to the fluid. During agitation, the overall motion of the fluid can be considered as the combination of two contributions: rigid body rotation and deformation. The latter provides an indication of the intensity of the deformation experienced by the fluid, as well as its contribution to the total motion. ([1])

Using the software CFD post it is possible to calculate the velocity gradient, useful to extract the different contribution of the rotation and the deformation.

The velocity gradient is defined as follow:

$$\nabla \vec{\mathbf{v}} = \begin{bmatrix} \frac{\partial v_x}{\partial x} & \frac{\partial v_x}{\partial y} & \frac{\partial v_x}{\partial z} \\ \frac{\partial v_y}{\partial x} & \frac{\partial v_y}{\partial y} & \frac{\partial v_y}{\partial z} \\ \frac{\partial v_z}{\partial x} & \frac{\partial v_z}{\partial y} & \frac{\partial v_z}{\partial z} \end{bmatrix}$$

At this point it is possible to define two different Tensor:

- Rate of Deformation, D;
- Vorticity Tensor, Ω .

The Rate of Deformation Tensor is a symmetric tensor about the contribution of the deformation to the fluid motion, called elongational stress. This tensor is defined as follow:

$$D = \frac{1}{2} (\nabla \vec{v} + (\nabla \vec{v})^T)$$
(23)

Or in an other way:

$$\mathbf{D} = \begin{bmatrix} \frac{\partial v_x}{\partial x} & \frac{1}{2} \left(\frac{\partial v_x}{\partial y} + \frac{\partial v_y}{\partial x} \right) & \frac{1}{2} \left(\frac{\partial v_x}{\partial z} + \frac{\partial v_z}{\partial x} \right) \\ \frac{1}{2} \left(\frac{\partial v_y}{\partial x} + \frac{\partial v_x}{\partial y} \right) & \frac{\partial v_y}{\partial y} & \frac{1}{2} \left(\frac{\partial v_y}{\partial z} + \frac{\partial v_z}{\partial y} \right) \\ \frac{1}{2} \left(\frac{\partial v_z}{\partial x} + \frac{\partial v_x}{\partial z} \right) & \frac{1}{2} \left(\frac{\partial v_z}{\partial y} + \frac{\partial v_y}{\partial z} \right) & \frac{\partial v_z}{\partial z} \end{bmatrix}$$

In a similar way we could define the Vorticity Tensor, which is antisymmetric and it can be written like this:

$$\Omega = \frac{1}{2} (\nabla \vec{v} - (\nabla \vec{v})^T) \tag{24}$$

Or in another way:

$$\mathbf{\Omega} = \begin{bmatrix}
0 & \frac{1}{2} \left(\frac{\partial v_x}{\partial y} - \frac{\partial v_y}{\partial x} \right) & \frac{1}{2} \left(\frac{\partial v_x}{\partial z} - \frac{\partial v_z}{\partial x} \right) \\
\frac{1}{2} \left(\frac{\partial v_y}{\partial x} - \frac{\partial v_x}{\partial y} \right) & 0 & \frac{1}{2} \left(\frac{\partial v_y}{\partial z} - \frac{\partial v_z}{\partial y} \right) \\
\frac{1}{2} \left(\frac{\partial v_z}{\partial x} - \frac{\partial v_x}{\partial z} \right) & \frac{1}{2} \left(\frac{\partial v_z}{\partial y} - \frac{\partial v_y}{\partial z} \right) & 0
\end{bmatrix}$$

For each tensor is possible to calculate the magnitude using the Frobenius Norm. In this way is possible to quantify the contribution of both the deformation and the vorticity. ([1])

$$\xi = |D:D|^{\frac{1}{2}} = |\sum_{i} \sum_{j} D_{ij} D_{ji}|^{\frac{1}{2}}$$
(25)

Which is representing the intensity of the local deformation without the contribution of the rotation.

In the same way:

$$\omega = |\Omega:\Omega|^{\frac{1}{2}} = |\sum_{i} \sum_{j} \Omega_{ij} \Omega_{ji}|^{\frac{1}{2}}$$

$$(26)$$

Which is representing the intensity of the rotation of the fluid, without the contribution of the deformation.

It is also possible to calculate ϕ , the Dispersive Mixing Efficiency, which is the ratio of ξ and the sum $\xi + \omega$, helpful to evaluate how big is the contribution of the deformation to the total motion.([1])

$$\phi = \frac{\xi}{\xi + \omega} \tag{27}$$

For those simulation have been choose different points inside the tank, close to the impeller and in the middle of the tank at different heights. Then for each point, using CFD post, has been calculate the velocity gradient $\nabla \vec{v}$, helpful for obtain the two tensor defined

before, Ω and D. At this point the value of ξ and ω has been esteemed, for discover which zone has the high intensity of deformation.

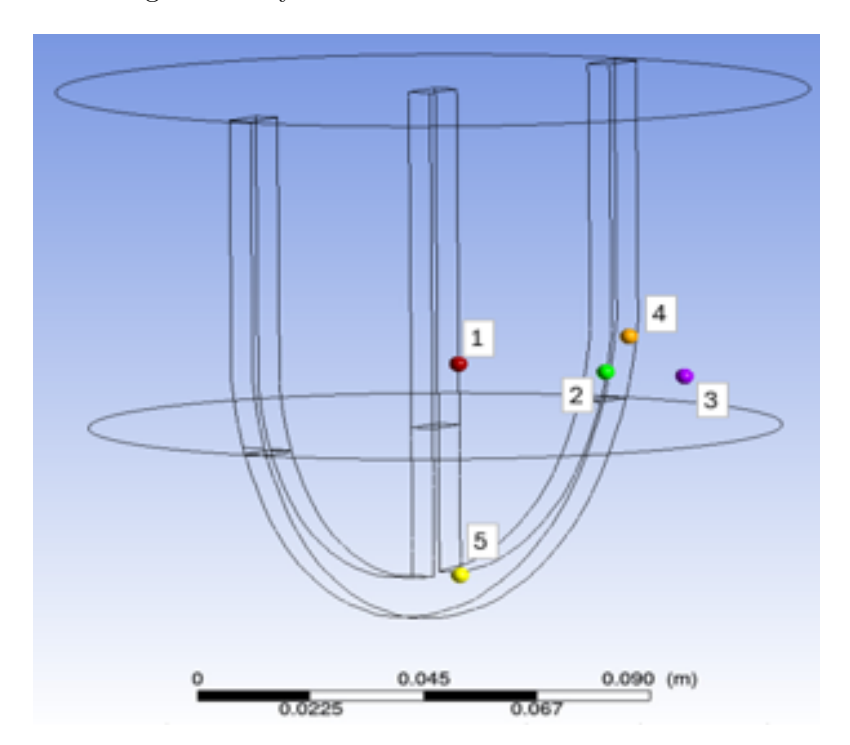


Figure 41. Points inside the tank.

From those points have been calculated the following results:

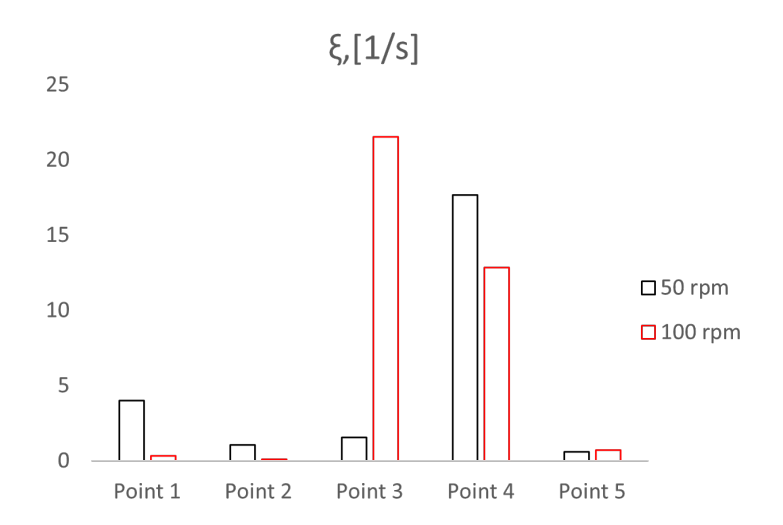


Figure 42. Intensity of deformation for two different velocity

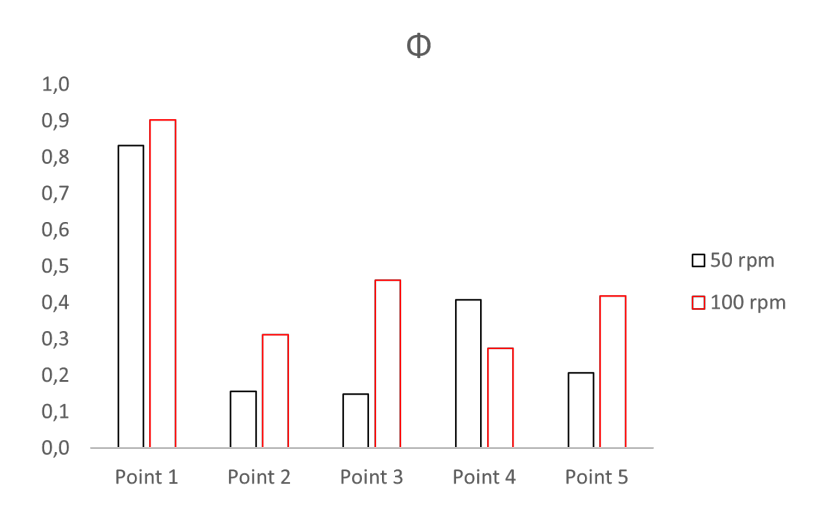


Figure 43. Dispersive mixing efficiency for two different velocity

The intensity of deformation varies significantly within the tank, indicating that the fluid is not uniformly in motion. A comparison between two rotational speeds shows that increasing the impeller speed enhances the deformation intensity, with the highest values occurring near the tank wall and the impeller.

The dispersive mixing efficiency, ϕ , also change a lot in the tank, ranging from 0.15 to 0.9. When the the value is higher than 0.5 it means that the contribution of the deformation is higher than the contribution of the rotation. Increasing the rotational speed increase also the contribution of the deformation and the value decrease in the middle of the tank. In the last part of the model validation have been calculated the percentage of dead zones in the tank during the reaction for the two fluids. The dead zones or stagnant zones are defined as zones where the shear rate is lower than the critical shear rate defined during the setup for the Herschel Bulkley model.

It is possible to calculate the shear rate in the CFD post but it is necessary to define it as follow:

$$\dot{\gamma} = \sqrt{2\left[\left(\frac{\partial u}{\partial x}\right)^2 + \left(\frac{\partial v}{\partial y}\right)^2 + \left(\frac{\partial w}{\partial z}\right)^2 + \frac{1}{2}\left(\frac{\partial u}{\partial y} + \frac{\partial v}{\partial x}\right)^2 + \frac{1}{2}\left(\frac{\partial u}{\partial z} + \frac{\partial w}{\partial x}\right)^2 + \frac{1}{2}\left(\frac{\partial v}{\partial z} + \frac{\partial w}{\partial y}\right)^2\right]}$$
(28)

It is possible calculate the volume of fluid with shear rate below a certain value using the iso volume tools on CFD post. Then, the percentage of dead zone over the total volume of fluid has been calculated for different velocities with the aim of evaluate at which rotational speed there are no more stagnant zones.

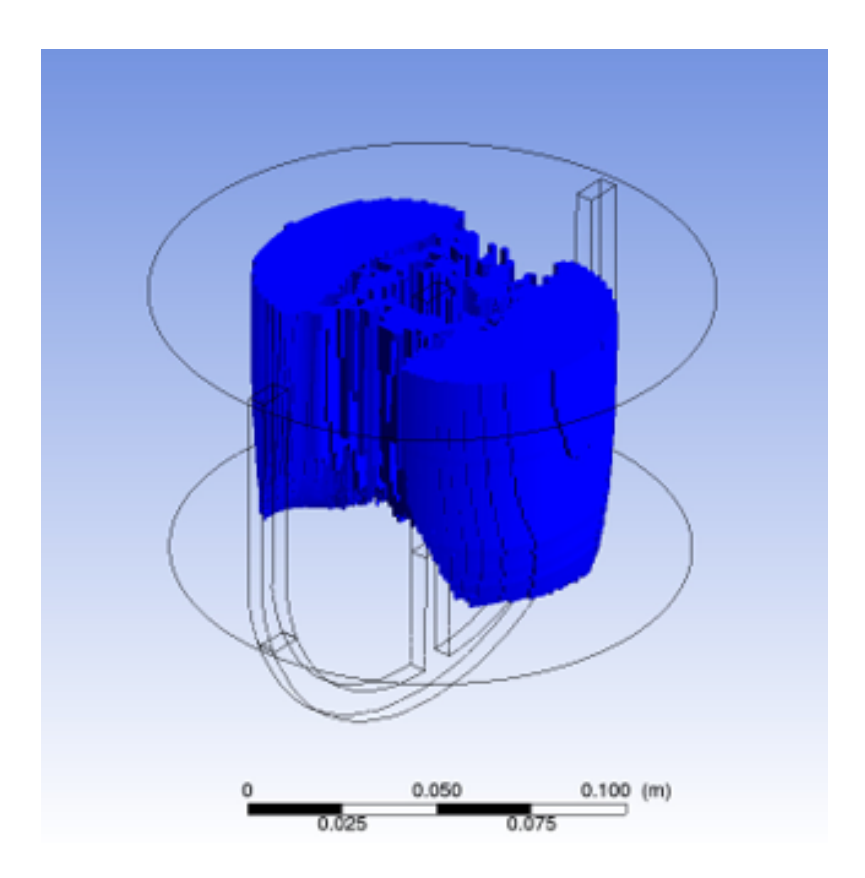


Figure 44. Stagnant Zones $27.5\%\frac{w}{w}$ after 1h at 50rpm

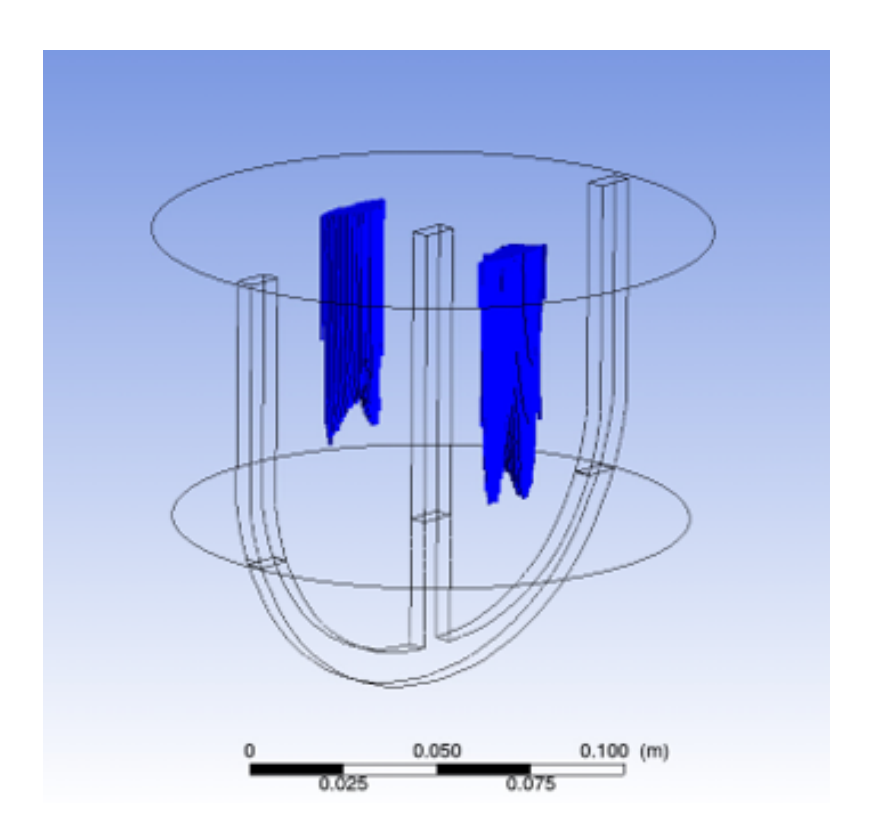


Figure 45. Stagnant Zones $27.5\% \frac{w}{w}$ after 2h at 50rpm

Those two figures (Figure 44 45) shows the changes of the stagnant zones during the reaction of hydrolysis. At the beginning, mixing of the fluid is very difficult, resulting in large dead zones. As the reaction progresses, the stagnant zones decrease, leading to an improvement in the mixing efficiency of the impeller.

In CFD-Post, it is possible to calculate the fluid volume where the local shear rate is lower than a specified critical value. This critical shear rate was chosen as the criterion for identifying stagnant regions, since below this threshold the fluid behaves as a highly viscous material. The resulting stagnant volume was then normalized with respect to the total fluid volume in the tank.

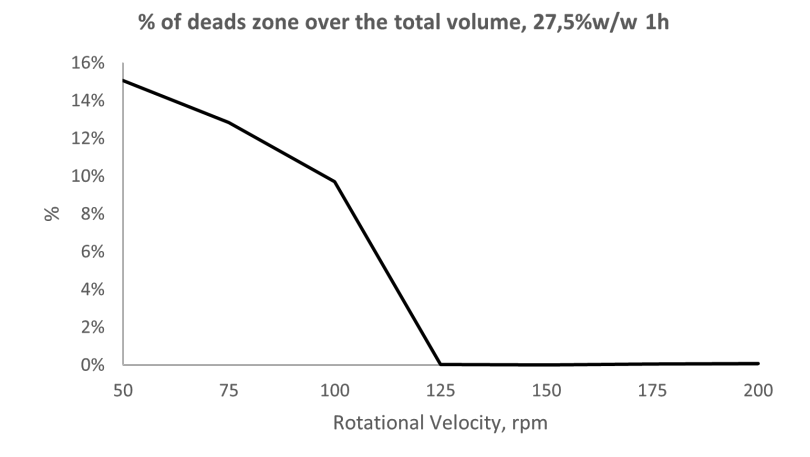


Figure 46. % of dead zones over the total volume, $27.5\% \frac{w}{w}$ after 1h

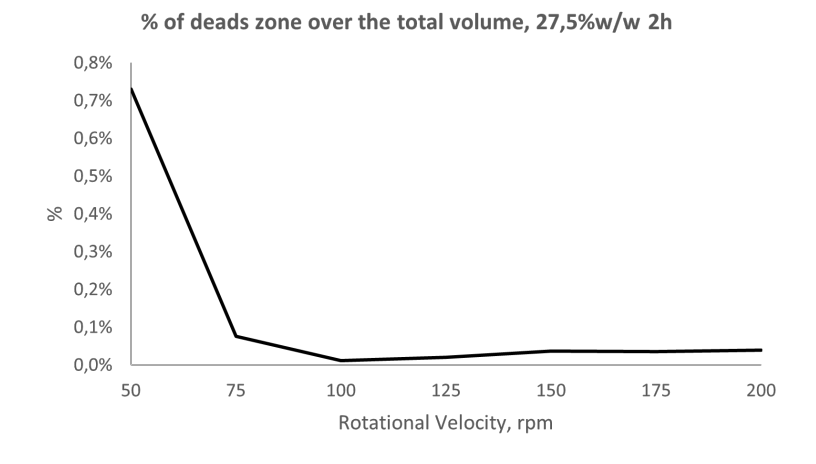


Figure 47. % of dead zones over the total volume, $27.5\% \frac{w}{w}$ after 2h

For the fluid $27.5\% \frac{w}{w}$ after 1h of reaction it is possible to not have any dead zone with a rotational velocity of 125rpm, while with the fluid after 2h of reaction, the percentage of stagnant zone have always value under 1%, meaning that the mixing efficiency is quite good for all the velocities.

0.10 Fitting of the Experimental Data

Regarding the rheological data, experimental measurements obtained at the IFPEN laboratories were used. These consisted of shear stress versus shear rate curves recorded throughout the liquefaction process, approximately once per hour for a total duration of six hours. The Herschel Bulkley model was then fitted to these curves in order to determine the optimal parameters: τ_0 , k, and n. These three parameters were subsequently implemented in Fluent to simulate the fluid behavior.

To best represent the liquefaction process, three time points were selected: the first hour, the midpoint (three hours), and the final stage (six hours). The rheological data were collected at three different constant rotational speeds (50, 100, and 150 rpm), with the experiments conducted using the Paravisc IKA impeller.

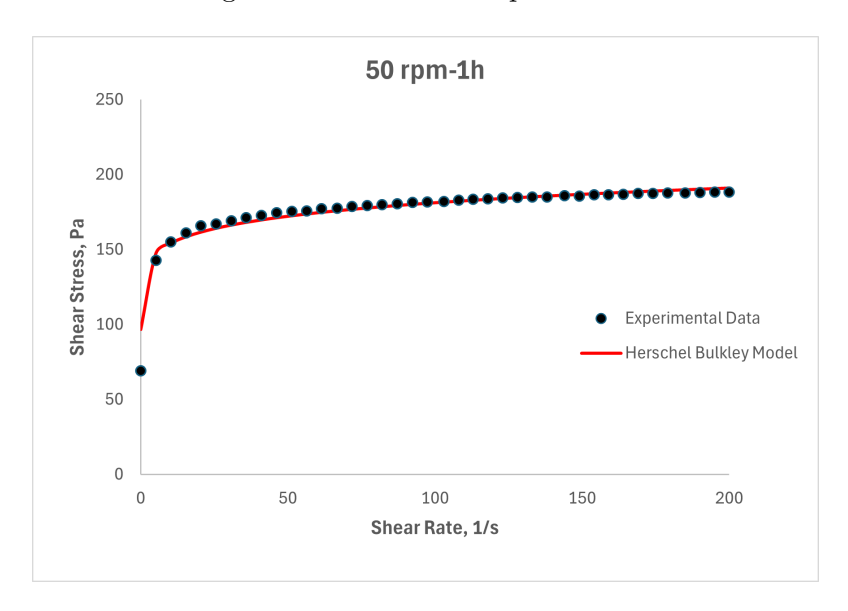


Figure 48. Rheological Data Fitting of Experimental Data, 50 rpm after 1 hour of reaction.

Rotational speed, [rpm]	time, [hours]	$\tau_0, [Pa]$	$k, [Pas^n]$	n, [-]
50	1	68,29	65,00	0,120
50	3	34,77	27,00	0,055
50	6	27,36	22,79	0,054
100	1	68,60	46,50	0,150
100	3	58,00	38,00	0,101
100	6	31,56	23,09	0,101
150	1	51,40	36,00	0,110
150	3	34,71	31,00	0,070
150	6	23,79	20,00	0,100

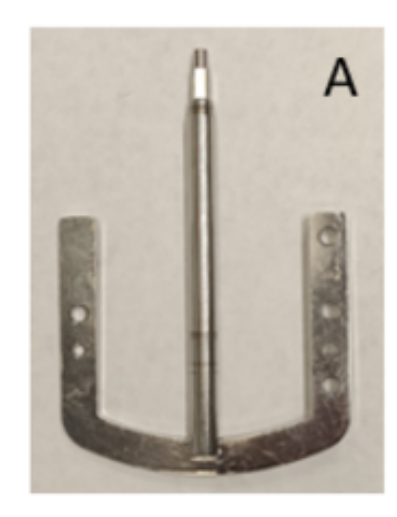
0.11 IKA Reactors

0.11.1 Geometry

For the modeling it has been used the same IKA reactor (Figure 49) with three different impellers (Figure 50). The items available in the laboratory were the following:



Figure 49. 3L stirred tank reactor setup.



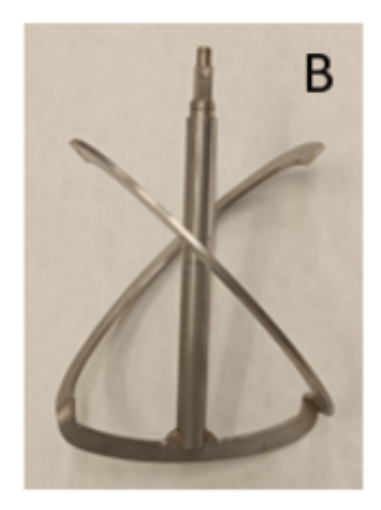


Figure 50. A) Anchor B) Paravisc

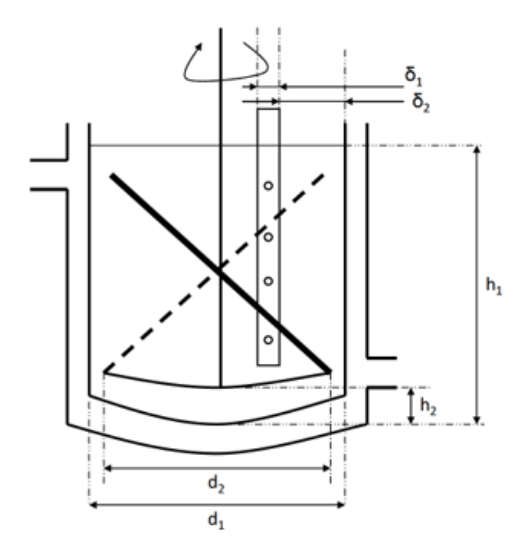
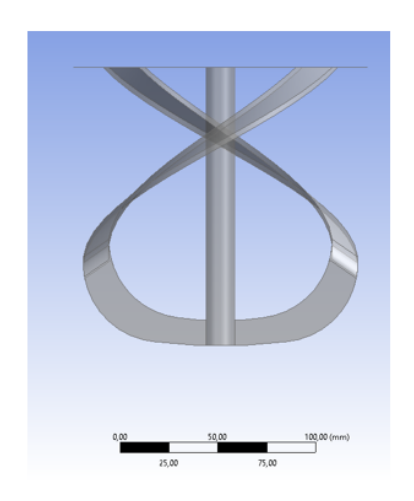


Figure 51. Geometry of the tank with the paravisc

- H1: high of the liquid = 165 mm
- H2: position of the impeller relative to the bottom of the tank = 30 mm
- D1: internal diameter of the tank = 150 mm
- D2: impeller diameter = 130 mm

The creation of the geometry has been done on Desingmodeler on ANSYS fluent (Figure 52 and 53) and the dimensions were measured in the IFPEN laboratories.



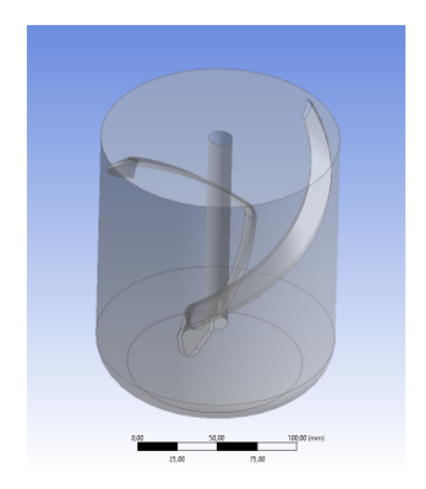
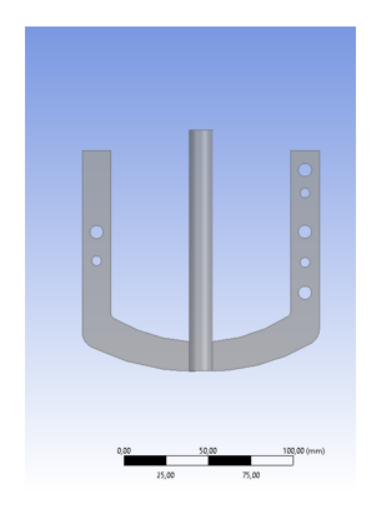


Figure 52. Geometry of the paravisc impeller.



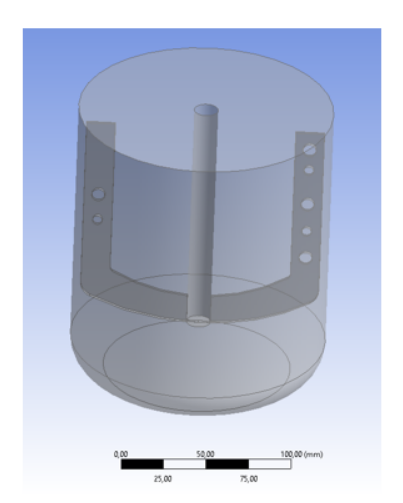


Figure 53. Geometry of the anchor impeller.

0.11.2 Mesh

To generate a high quality mesh for the IKA reactors, the Hexcore type was selected due to its ability to provide good resolution in complex geometries without requiring an excessive number of cells. Subsequently, a grid independence study was carried out to determine the optimal number of cells, using both a Newtonian fluid and a non-Newtonian fluid modeled with the Herschel Bulkley equation.

During CFD simulations maybe be different source of error and among the most common, we find:

- Discretization error and rounding error
- Iteration or convergence error
- Physical modeling error:
- Human error

Regarding discretization error, this can be observed by considering a transport variable ϕ and analyzing the finite difference formulation, specifically through the Taylor series expansion.

The discretization of the spatial derivative error is expressed through the error term $o(\Delta x)$, which decreases as the grid size is reduced.

Rounding error is a well known phenomenon that occurs when decimal numbers are approximated. In CFD, rounding errors are influenced by numerical precision, which can be either single or double precision. Single precision (32-bit) calculations are faster but introduce greater errors, whereas double precision (64-bit) provides higher accuracy at the cost of increased computational time.

The grid refinement process aims to optimize numerical parameters, such as grid size, to

reduce discretization error and strike a proper balance with rounding error, as demonstrated in the trade-off graph between discretization error and computational time. The goal of a grid refinement study is to ensure a high-quality solution without excessive computational time.

Furthermore, a grid independence study is essential to determine when the simulation results no longer change with further mesh refinement (that is, when sufficient accuracy has been achieved). To properly conduct a grid independence study, the procedure typically involves defining the geometry, creating an initial mesh, selecting a key parameter to monitor, running the simulation, and iteratively refining the mesh. These steps are repeated until the results indicate that the solution is independent of the grid, allowing the selection of an optimal mesh size for subsequent analyses.

For the Anchor IKA has been choose a mesh of about $7*10^5$ cells while for the Paravisc IKA a similar mesh of about $6*10^5$ has been used. The grid independence has been conducted using the value of the torque on the impeller and the best mesh has been selected when the value of the torque didn't change significantly along the different mesh.

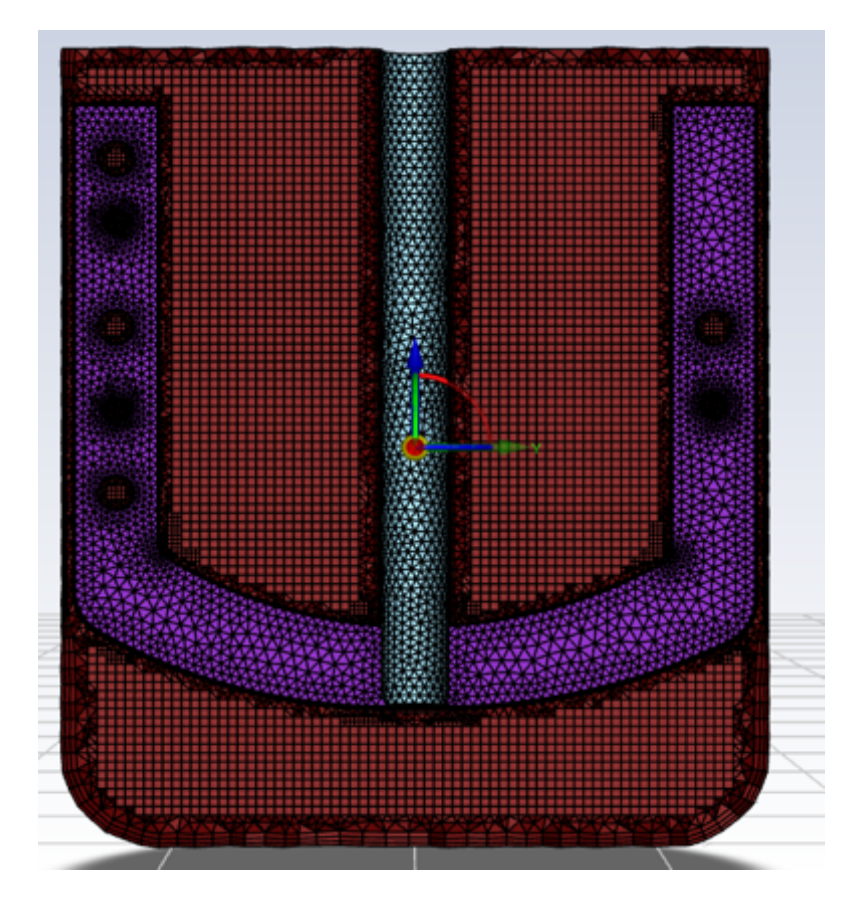


Figure 54. Anchor IKA Hexcore Mesh

Grid Indipendence Newtonian Fluid

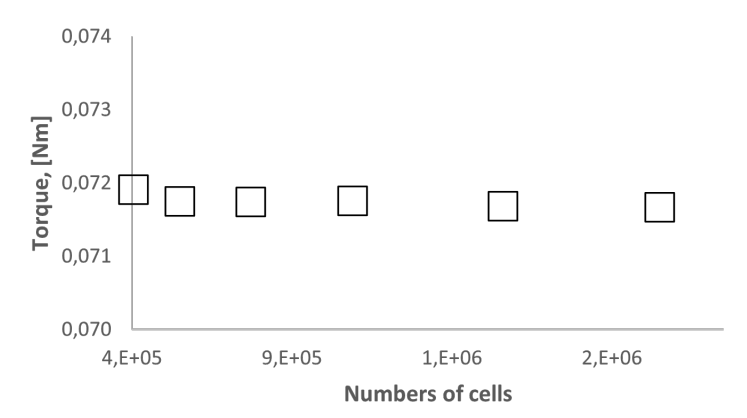


Figure 55. Grid Independence with Newtonian fluid (Glycerin, $\mu = 0.37 Pas$ at $36^{\circ}C$ [2])

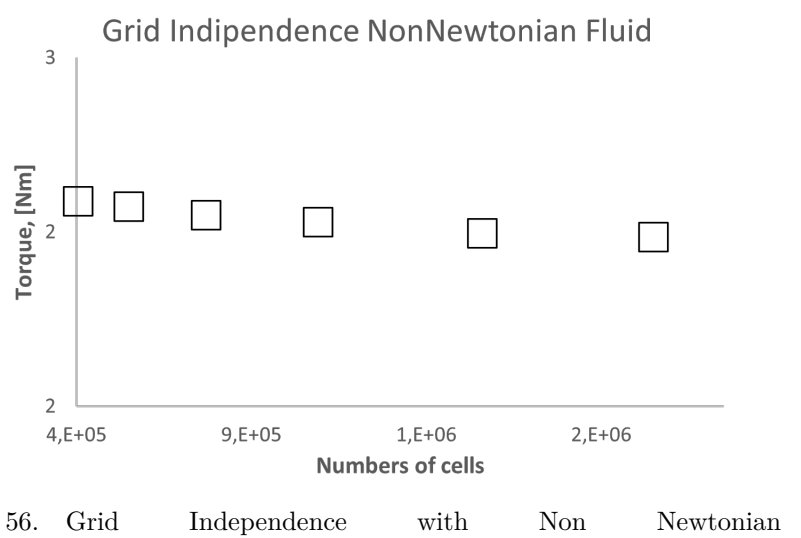


Figure 56. Grid Independence with Non Newtonian fluid $(\tau_0=484.14Pa,k=0.00113Pas^n,n=2.3$ [2])

Different mesh with different number of cells have been used, ranging from $4*10^5$ to $3*10^6$, but the value of Torque doesn't change much during all the simulations. So, for have the best compromise between accuracy and velocity has been choose the mesh with $7*10^5$.

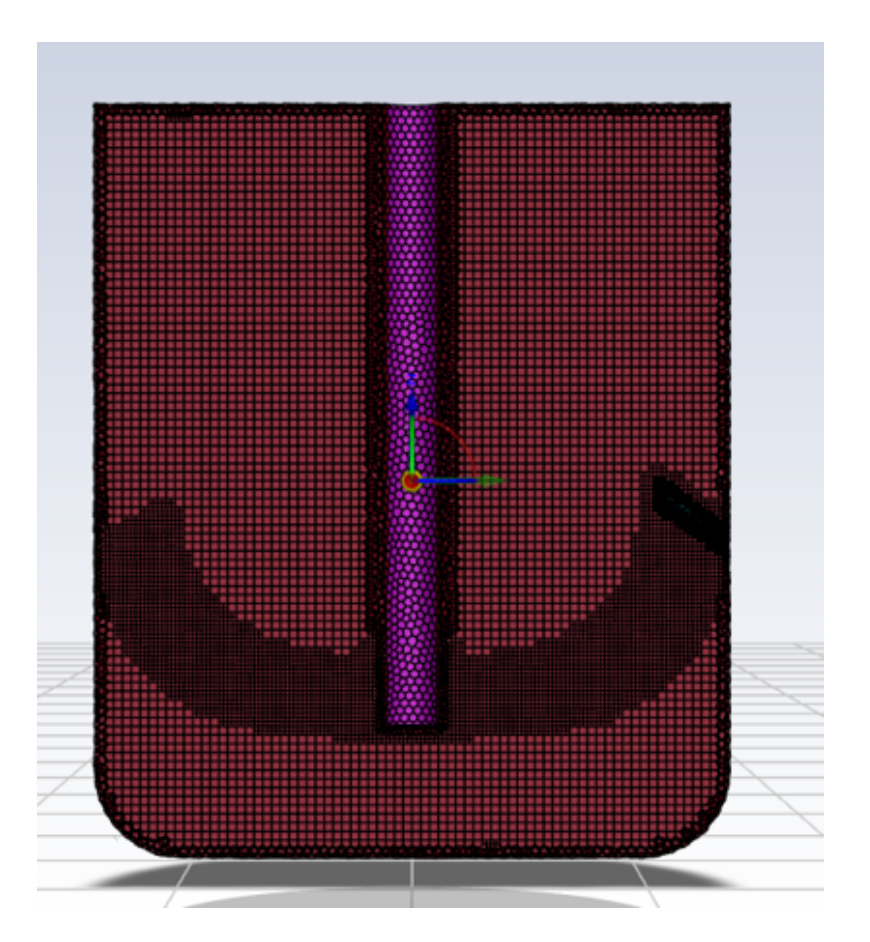


Figure 57. Paravisc IKA Hexcore Mesh



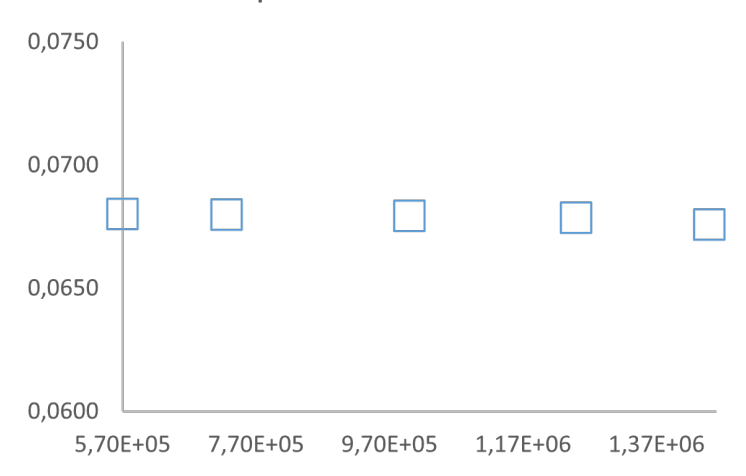


Figure 58. Grid Indipendence with Newtonian fluid (Glycerin, $\mu = 0.37 Pas$ at $36^{\circ}C$ [2])

Grid Indipendence NonNewtonian Fluid



Figure 59. Grid Independence with Non Newtonian fluid $(\tau_0 = 484.14 Pa, k = 0.00113 Pas^n, n = 2.3$ [2])

Also for the Paravisc IKA has been tried different number of cells, and, for achieve the best compromise, the one with $6*10^5$ has been selected.

0.11.3 Metzner Otto Constant

For the calculation of the Metzner Otto constant has been used the method used in the Model Validation section.

The first step is to calculate the curve Np-Re and obtain the value of the Power Constant,

B with (18). The Newtonian fluids used with this aim are the same used before (glycerin, polyglycerin and starch), and the proprieties can be observed in the table (0.9).

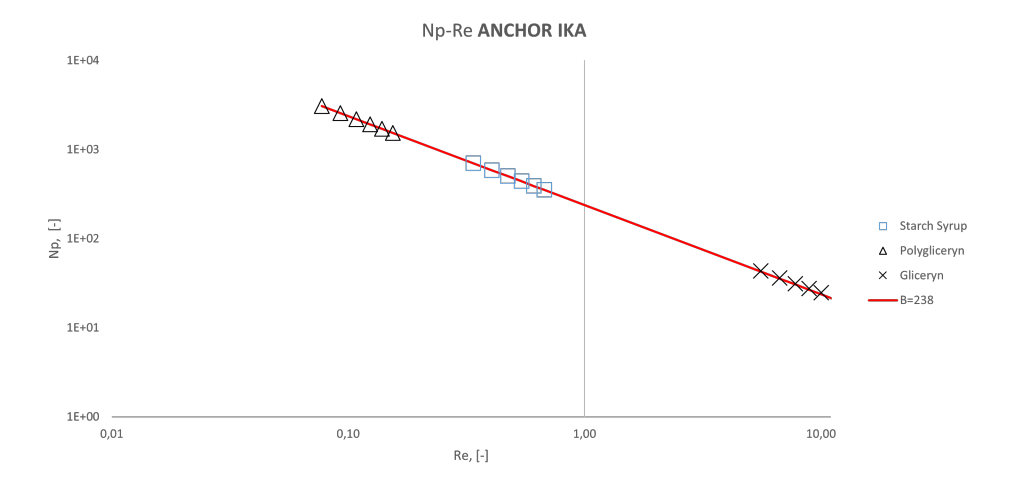


Figure 60. Np - Re for Anchor IKA impeller

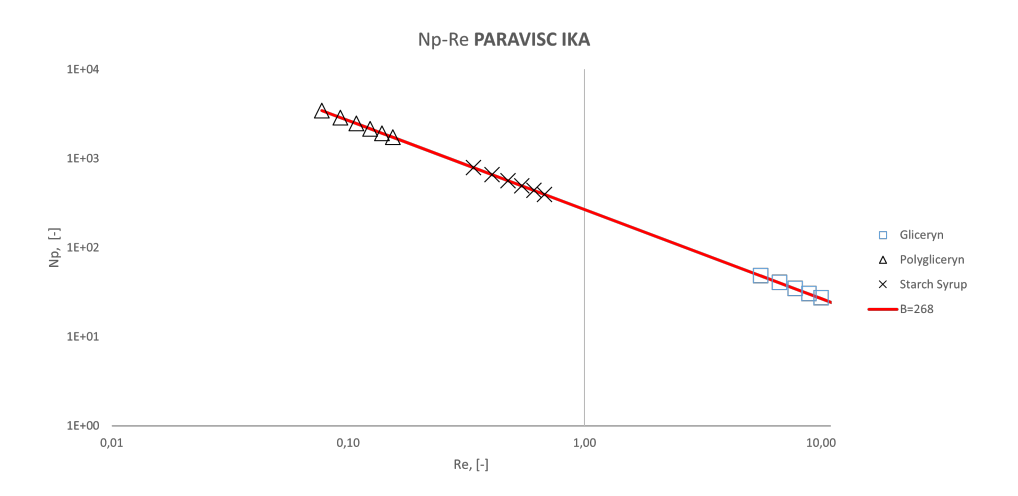


Figure 61. Np - Re for Paravisc IKA impeller

From these two graphs it is possible to extract the value of the power constant. For the anchor IKA the values are the following.

Anchor IKA	Power Constant, B
Glycerin	245
Polyglicerin	238
Starch Syrup	238

For the next calculations has be assumed a Power Constant equal to 238. In the same way is possible to calculate the constant for the Paravisc IKA.

Paravisc IKA	Power Constant, B
Glycerin	272
Polyglicerin	268
Starch Syrup	268

For the next calculations has be assumed a Power Constant equal to 268. Then, using two different fluids modeled with the Power Law model (9), also used in the section of Model Validation, it is possible to calculate the Metzner Otto Constant with the formula (22).

Metzner & Otto Constant Anchor IKA	
HEC 1.75 %	
HEC 2.00 %	

Metzner & Otto Constant Paravisc IKA	Ks
HEC 1.75 %	
HEC 2.00 %	

0.11.4 Real Rheology Simulations

In this section has been simulated the real rheology of the slurry during the liquefaction. The parameters for the Herschel Bulkley model have been calculated in the past section and so three different time have been used:

after 1 hour of reaction, 3 hour of reaction and at the end of the process. For each time, three different velocities have been investigated and after that, from the results, the torque on the impeller, the average shear rate and the elongation have been extracted with the aim to better understand how different impellers may impact the hydrodynamics of the system.

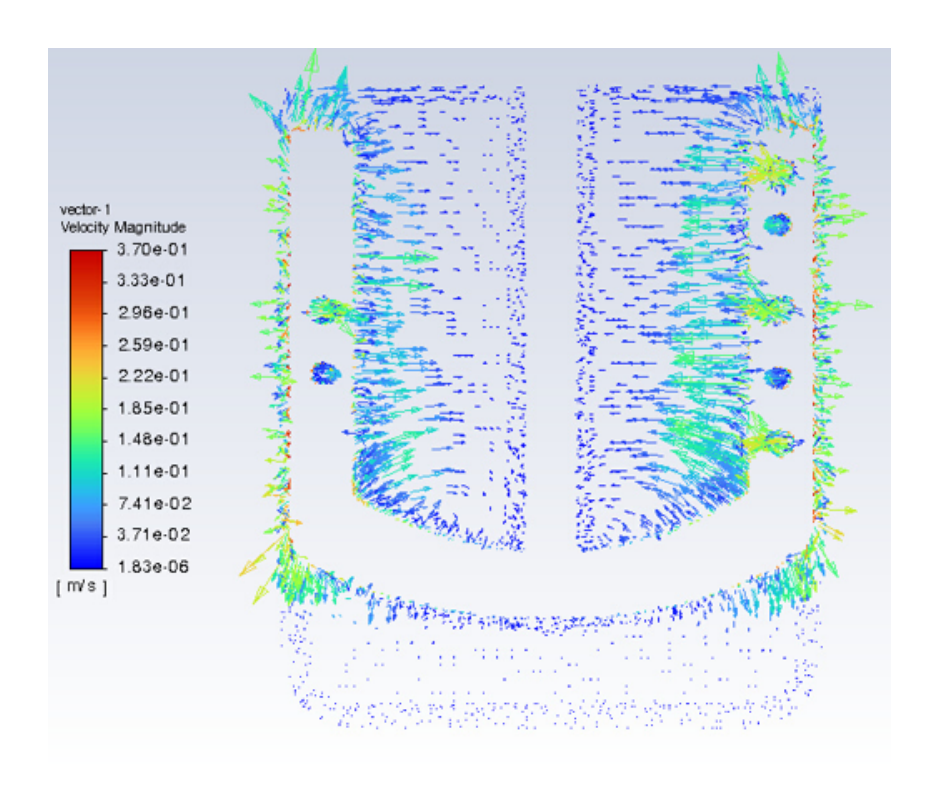


Figure 62. Velocity vectors for a rotational speed of 50rpm for Anchor IKA impeller after 6 hours of liquefaction

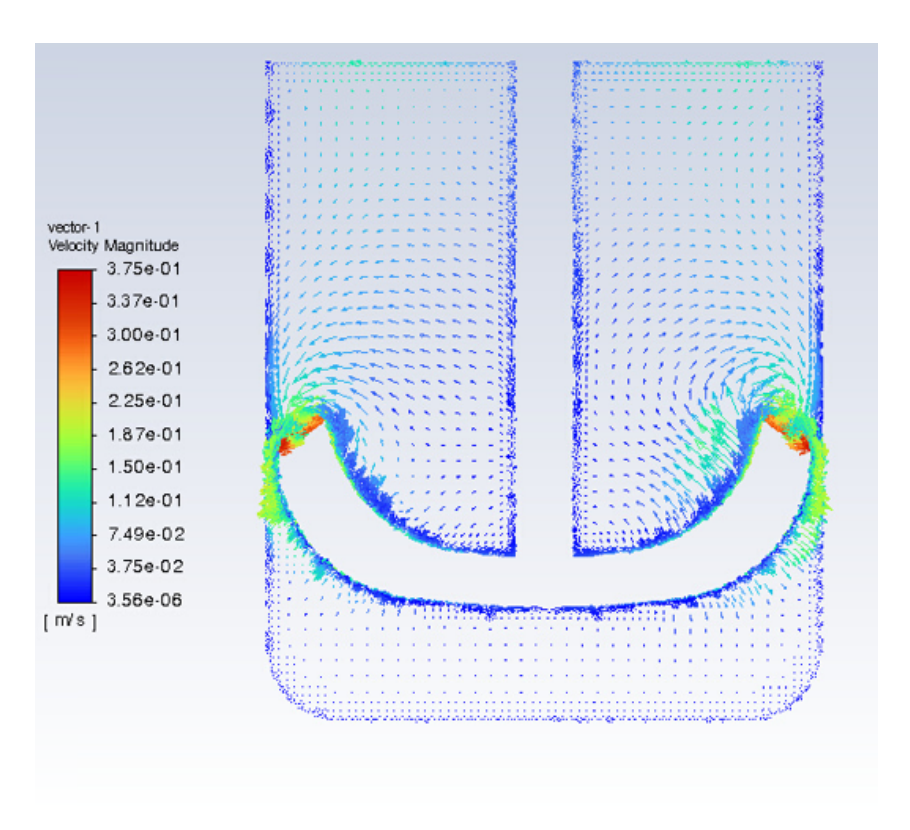


Figure 63. Velocity vectors for a rotational speed of 50rpm for Paravisc IKA impeller after 6 hours of liquefaction

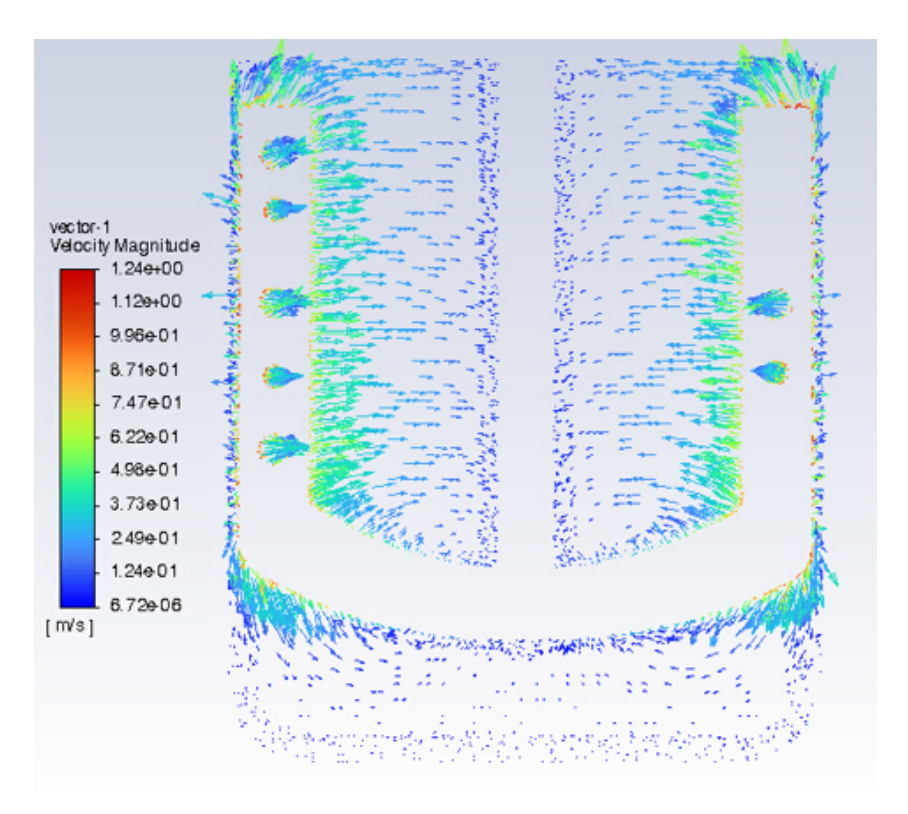


Figure 64. Velocity vectors for a rotational speed of 150rpm for Anchor IKA impeller after 6 hours of liquefaction

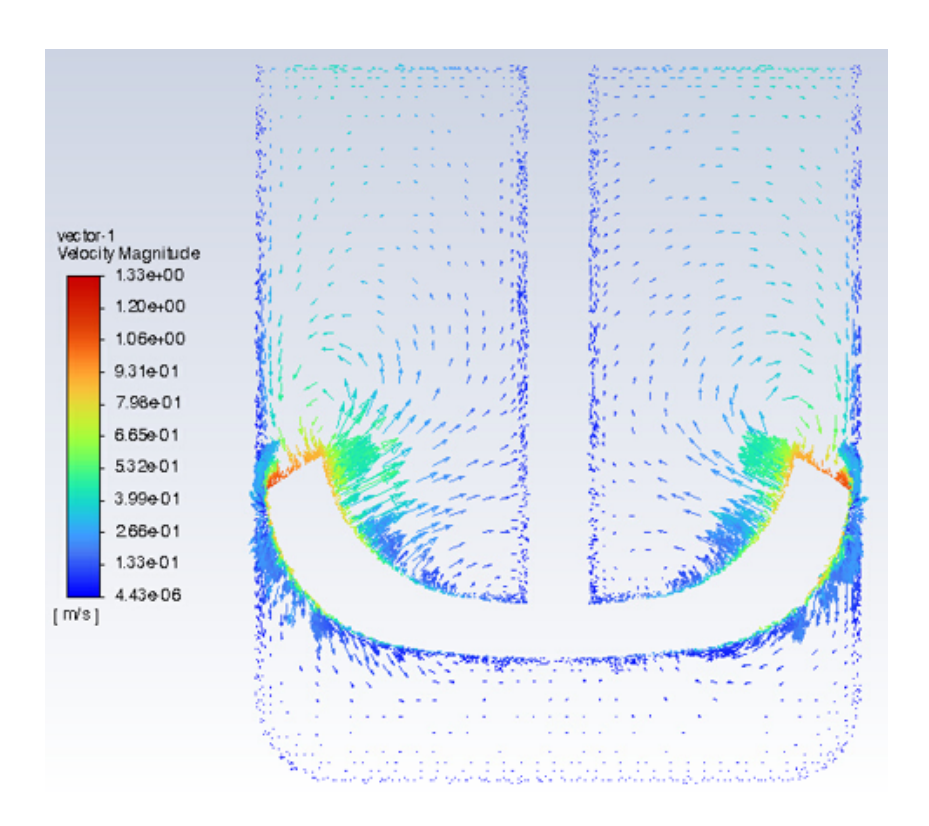


Figure 65. Velocity vectors for a rotational speed of 150rpm for Paravisc IKA impeller after 6 hours of liquefaction

In these four images (Figure 62 63 64 65) it is possible to observe how the velocity vectors change with the rotational speed, form 50 rpm to 150 rpm, and also how they change with different impeller, Anchor and Paravisc. It is important to see that the higher value of velocity is quite similar for both the impeller, slightly higher for the Paravisc.// As shown in the following graphs, the torque measured on the impeller is also very similar; however, it varies significantly over the course of the reaction.

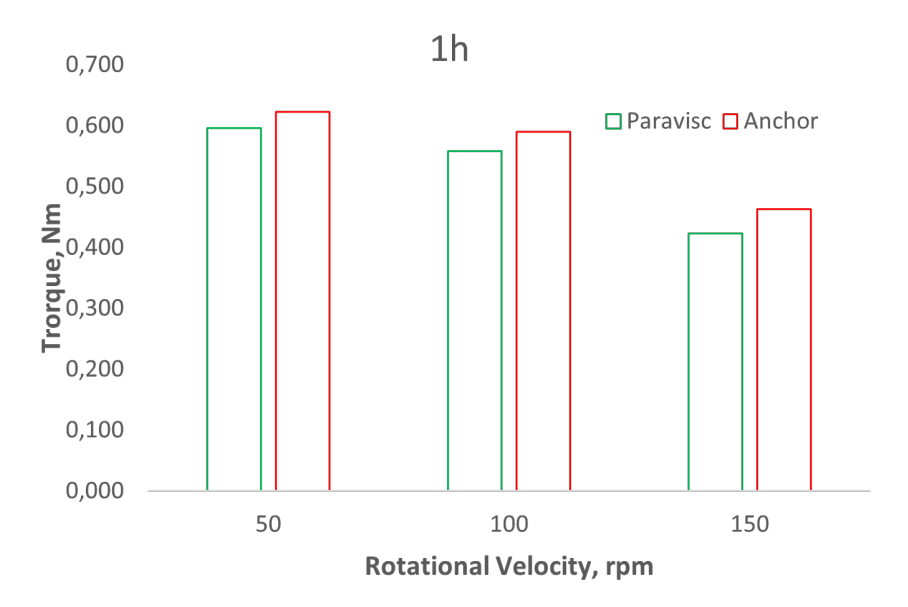


Figure 66. Comparison of the Torque measured on the impellers after 1 hour of reaction, for different velocities.

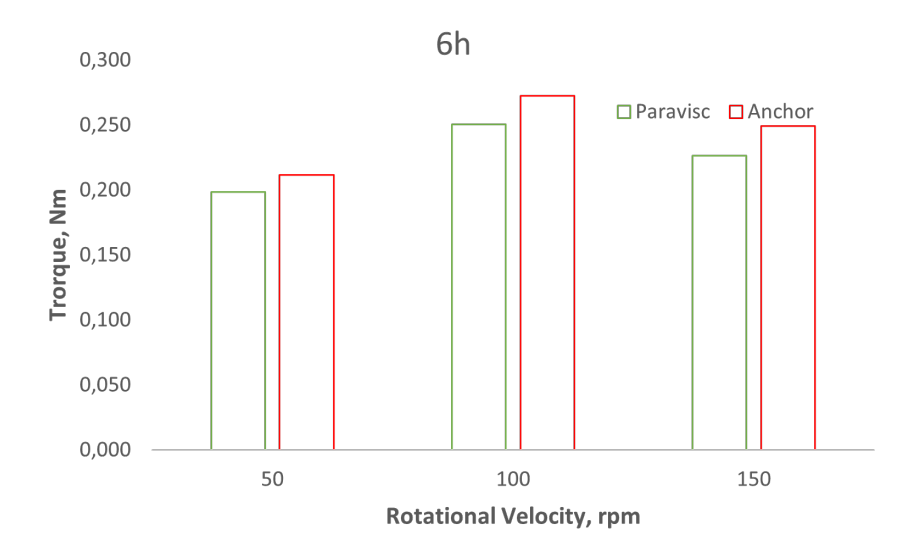


Figure 67. Comparison of the Torque measured on the impellers after 6 hour of reaction, for different velocities.

With the values of torque and using 14 it is possible to calculate the Power required for the agitation and then, using the 15, to calculate the Power Number, Np. In the end, using 19 it is possible to estimate the apparent viscosity.

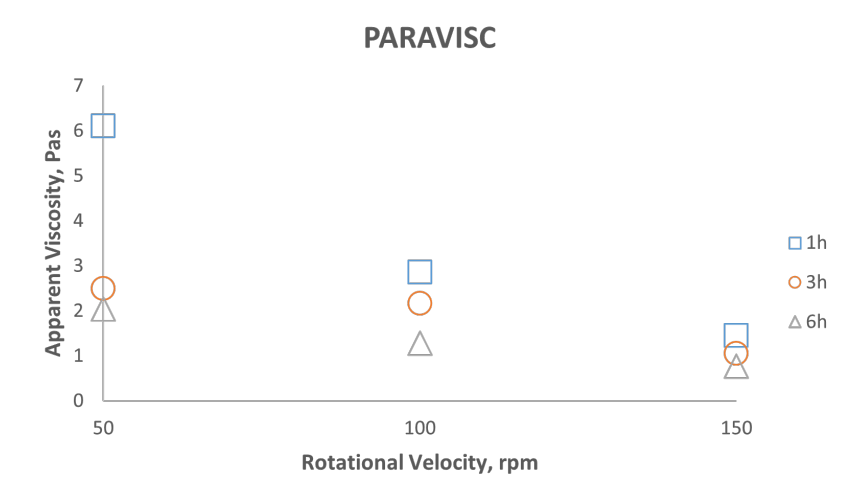


Figure 68. Apparent Viscosity of the slurry for different time of reaction and rotational speed. Paravisc Impeller.

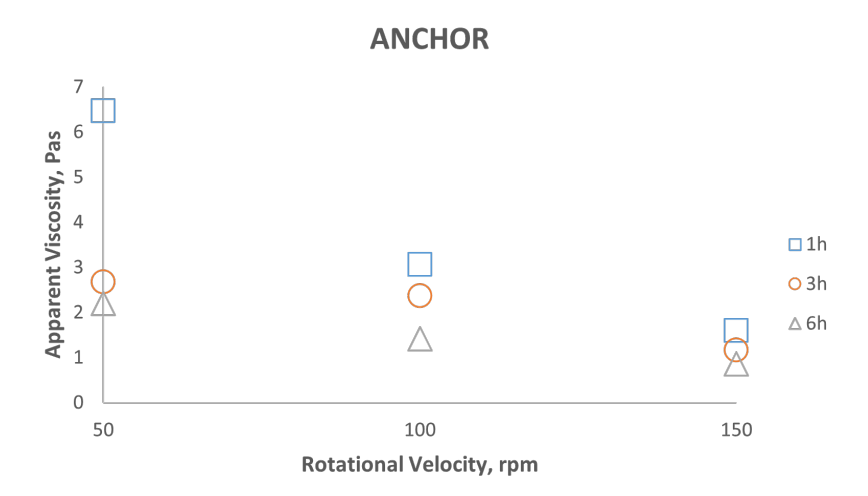


Figure 69. Apparent Viscosity of the slurry for different time of reaction and rotational speed. Anchor Impeller.

These graphs (Figure 68 69) are showing how is varying the apparent viscosity along the reaction time. The trend is descendant, mostly in the first part of the reaction time, from the first hour to after three hours. The viscosity is also decreasing with the rotational speed of the impeller and higher is the velocity and lower is the effect during the reaction time. The Reynolds number is between 1 to 70, still in the laminar regime.

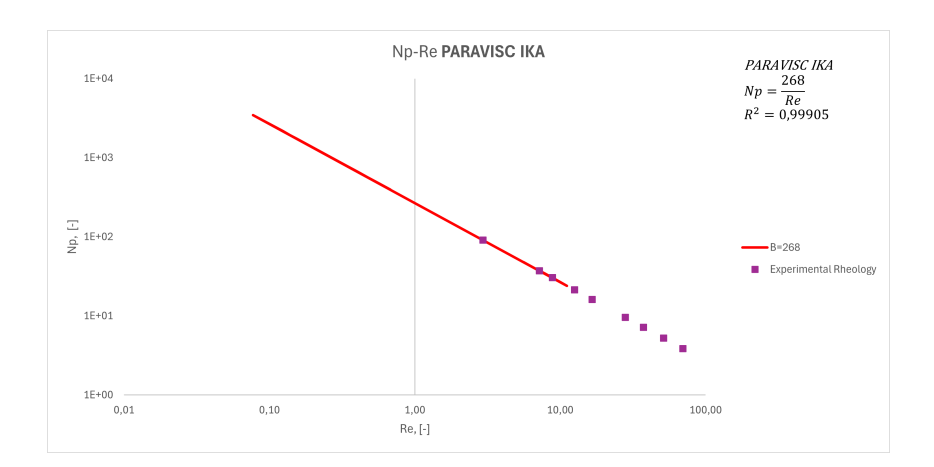


Figure 70. Np - Re graph for Paravisc with the Experimental Rheology points.

As it is possible to observe from this graph (Figure 70), the experimental points are still in the linear part of the graph and so the system is still in the laminar regime. Knowing the apparent viscosity it is possible to estimate again the Metzner Otto constant through the equation 10 and substituting the shear rate, $\dot{\gamma}$, with the Metzner Otto equation 21.

From the Herschel Bulkley model, it is possible to obtain an equation for the apparent viscosity, starting to divided by $\dot{\gamma}$ each part.

$$\frac{\tau}{\dot{\gamma}} = \frac{\tau_0}{\dot{\gamma}} + \frac{k \left(\dot{\gamma}\right)^n}{\dot{\gamma}} \tag{29}$$

Then, knowing that $\mu = \frac{\tau}{\dot{\gamma}}$, the formula can be written as follow:

$$\mu_{apparent} = \frac{\tau_0}{\dot{\gamma}} + k \left(\dot{\gamma}\right)^{n-1} \tag{30}$$

Now, it is possible to substitute the Metzner Otto equation 21 and obtain the final form of the equation:

$$\mu_{apparent} = \frac{\tau_0}{K_s N} + k \left(K_s N \right)^{n-1} \tag{31}$$

The equation is non linear and so it is necessary to use a program to fit the best value to obtain Ks. For this aim it has been used the Excel tool for fitting and the results are show below.

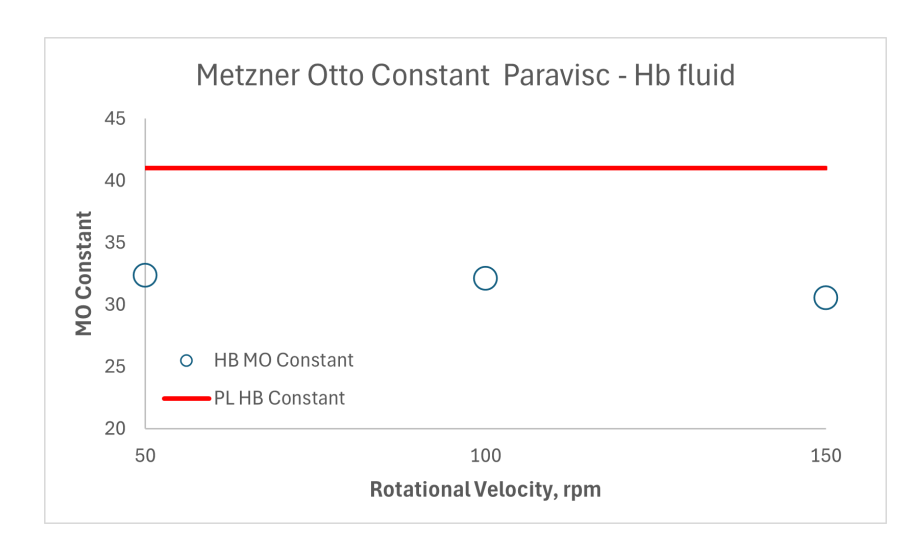


Figure 71. Values of Metzner Otto Costant for the Paravisc after 1h of reaction.

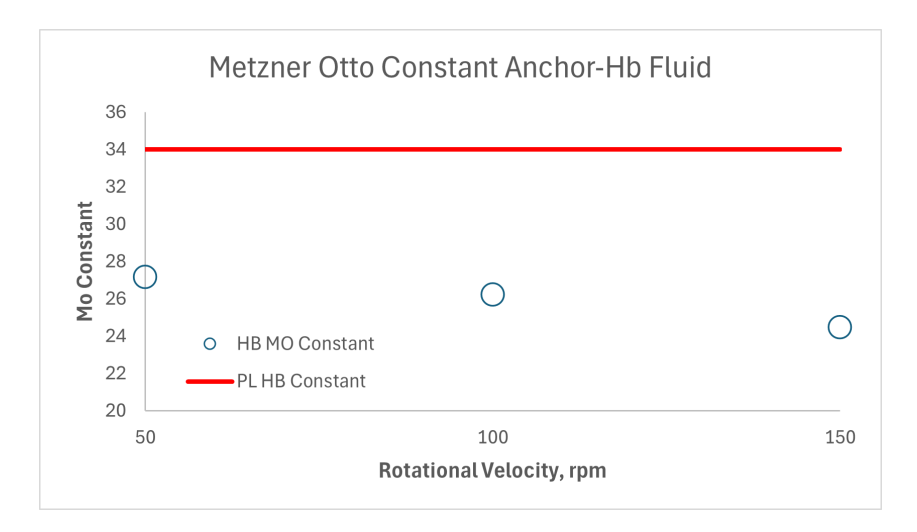


Figure 72. Values of Metzner Otto Costant for the Anchor after 1h of reaction.

The Metzner Otto (MO) values are compared to the ones calculated with the power law fluids (PL) and then plotted for each velocity (Figure 7172). It is possible to observe that the value in both case are decreasing with the rotational velocity, probably because the Reynolds number is getting higher and so the system is closer to the transition regime. For the Paravisc, the differences are about the 20%, while for the Anchor are around from 20% to 30%.

For the last part of this section, both the Average Shear Rate and the Elongation have been calculated. For the first parameter, has been used the Metzner Otto Equation 21, while for the second has been followed the procedure described in the Model Validation section. Then, the values for both the impellers have been compared to find any difference

between the set up.

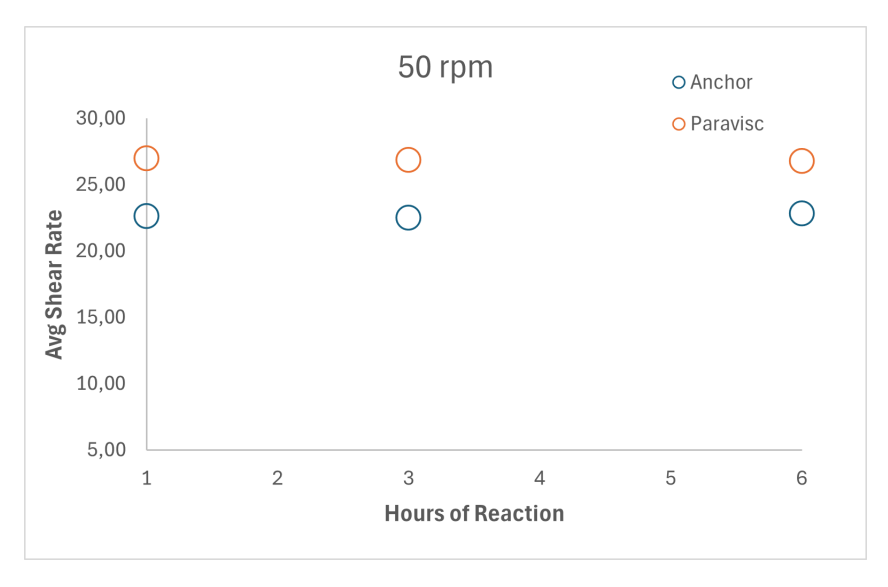


Figure 73. Comparison of the average Shear Rate between Paravisc and Anchor at $50 \mathrm{rpm}$ over the reaction time

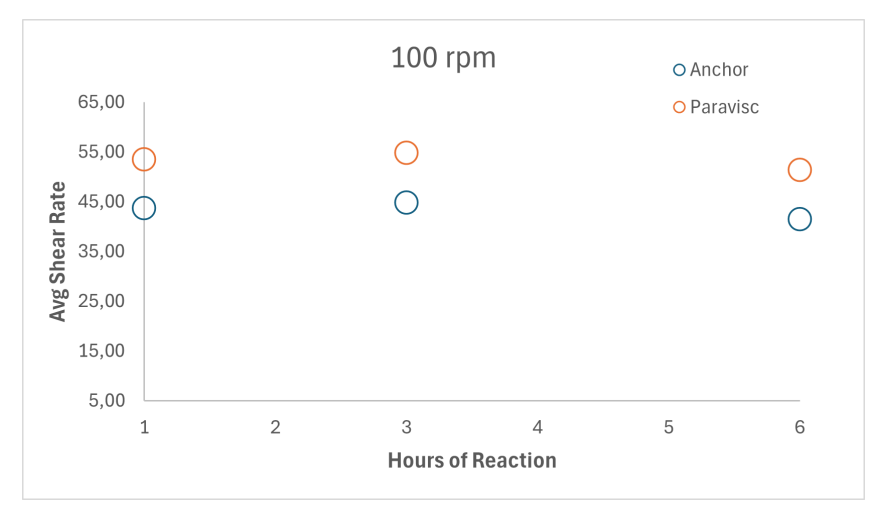


Figure 74. Comparison of the average Shear Rate between Paravisc and Anchor at $100 \mathrm{rpm}$ over the reaction time

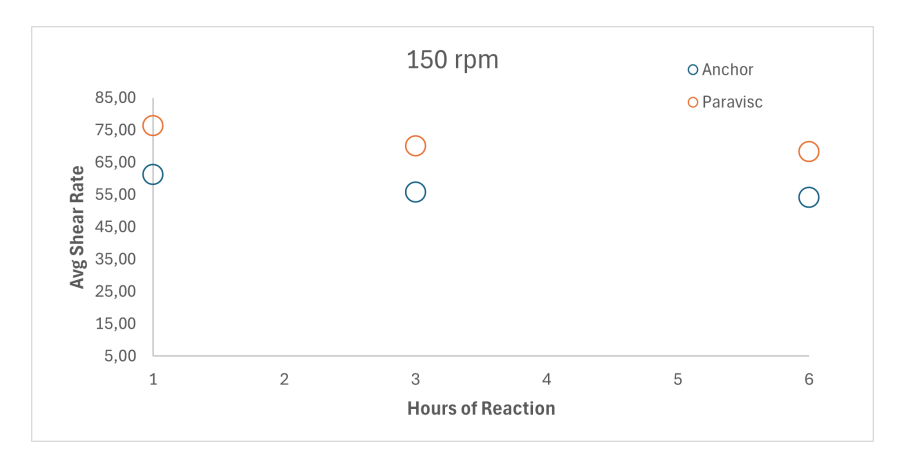


Figure 75. Comparison of the average Shear Rate between Paravisc and Anchor at 150rpm over the reaction time

From the comparison of the average shear rate values, it can be observed that it remains nearly constant throughout the reaction time, while increasing with the rotational speed. The Paravisc is able to provide the fluid with a higher shear rate, likely due to the fact that the impeller motion involves the entire volume of the tank.

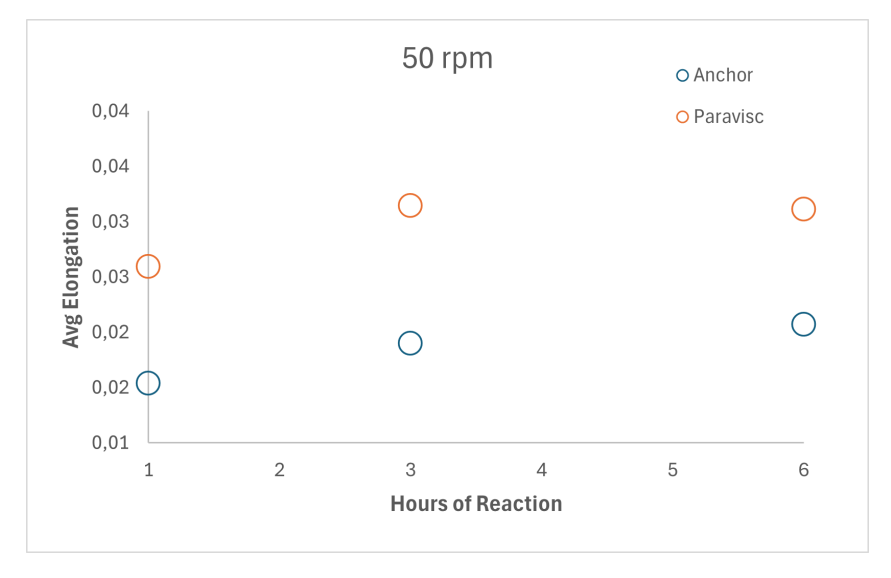


Figure 76. Comparison of the average Elongation between Paravisc and Anchor at 50rpm over the reaction time

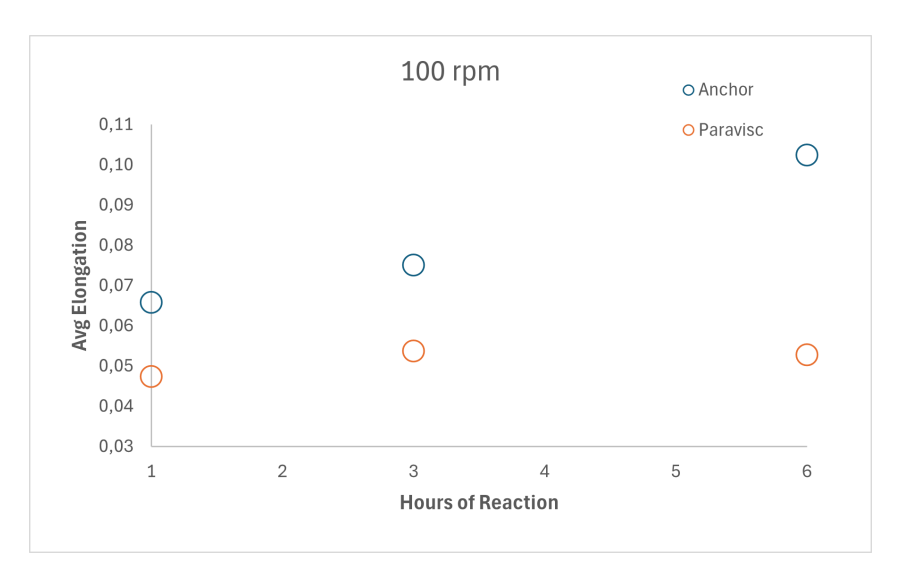


Figure 77. Comparison of the average Elongation between Paravisc and Anchor at 100rpm over the reaction time

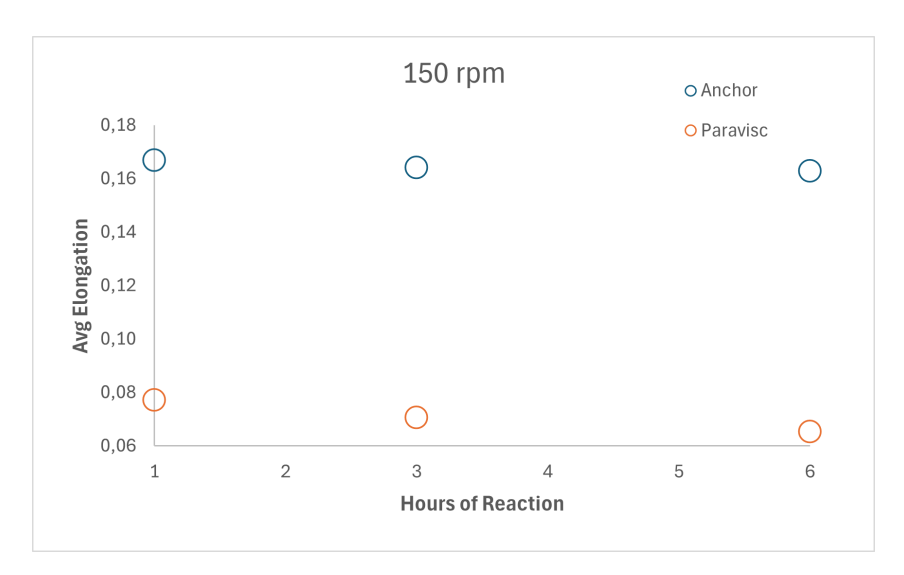


Figure 78. Comparison of the average Elongation between Paravisc and Anchor at 150rpm over the reaction time

Regarding the elongation, it shows a different trend as the rotational speed increases. At 50 rpm, elongation values rise over the course of the reaction, with the Paravisc exhibiting higher values than the Anchor. Thus, at low rotational speeds, the Paravisc is able to impart greater deformation to the fluid.

This trend changes at higher velocity, where the value of elongation of the Anchor become higher respect to the Paravisc and they also vary with the time.

At 150 rpm, the elongation values of the Anchor are nearly twice those of the Paravisc, suggesting that the Anchor should be recommended for agitation at high rotational speeds.

In the final part of this section, the presence of dead zones within the tank during agitation with different impellers was investigated. The stagnant zones were defined as in the Model Validation section. After selecting a shear rate threshold, typically equal to the critical shear rate used in the setup, the volume of fluid with a shear rate below this value was calculated.

The results are presented in the following graph.

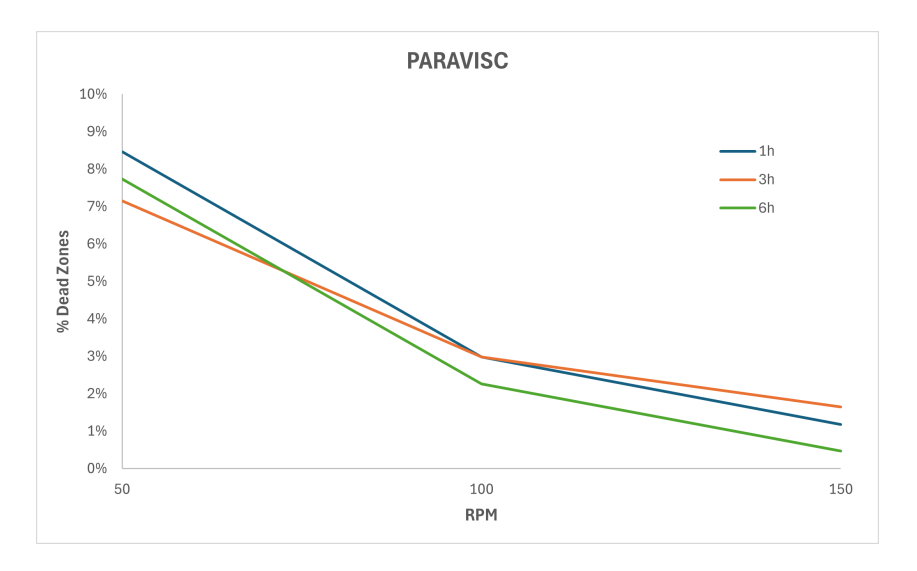


Figure 79. Percentage of Dead Zones in the tank with the Paravisc during the reaction time.

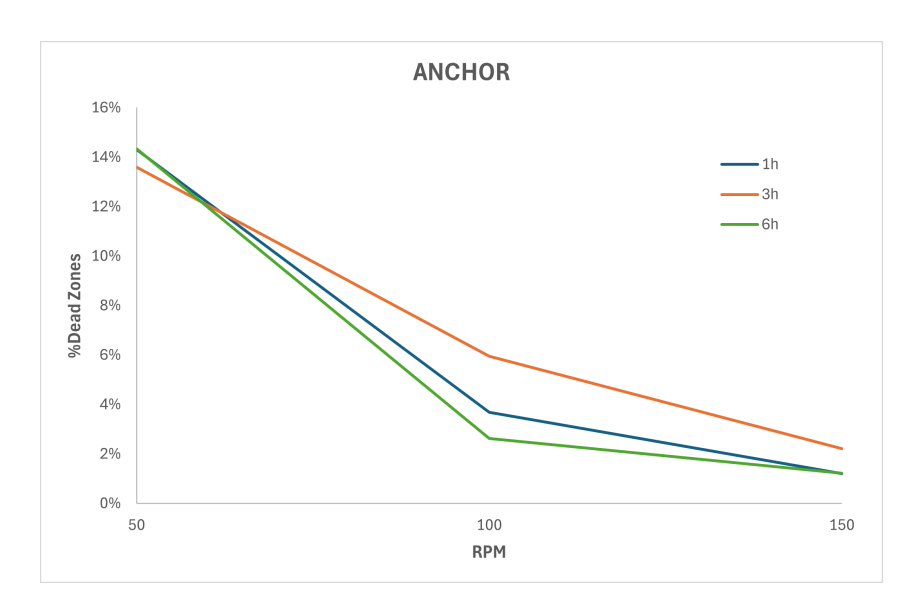


Figure 80. Percentage of Dead Zones in the tank with the Anchor during the reaction time.

From these graphs (Figure 79 80), the presence of low velocity regions can be observed in both configurations. To enable a clearer comparison between the two impellers, the volume of stagnant zones was normalized to the total volume of the tank. At 50 rpm, the Anchor exhibits a higher proportion of dead zones, ranging between 14% and 15%, after which the percentage begins to decrease. In contrast, with the Paravisc at low rotational speeds, stagnant zones are less pronounced, with values between 7% and 9%. At higher rotational speeds, the percentage of dead zones becomes very small in both cases, remaining below 5%. The observed difference between the impellers may be attributed to the ability of the Paravisc to set a larger portion of the fluid into motion compared to the Anchor.

0.12 Tornado Reactor

0.12.1 Geometry

Another reactor which the behavior was investigated is the Tornado Reactor. Is smaller compared to the IKA reactor and the volume is about 250 ml and the code for the identification is RR99935. In the following images it is possible to observe the setup, the reactor itself and the impeller used during the liquefaction period.



Figure 81. Tornado set up, it is possible to use more reactor at the same time and with different rotational velocity of the impeller.



Figure 82. Tornado Reactor.



Figure 83. Anchor impeller of the TORNADO Reactor.

After the measurement of the Reactor and the Impeller, it was possible to recreate the model on the commercial software ANSYS Fluent, using DesignModeler.

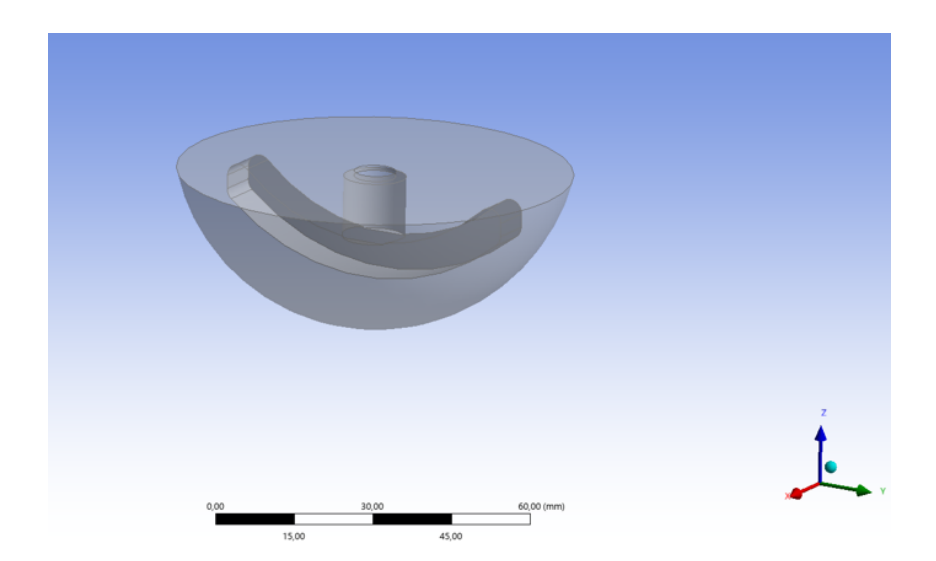


Figure 84. TORNADO Reactor geometry obtained using DesignModeler.

Then, the process of meshing was started, with similar approach used with the IKA reactor.

0.12.2 Mesh

For the TORNADO mesh was used a HEXCORE mesh and were conducted two grid independence, one for a Newtonian fluid and one with a Non Newtonian fluid modeled with the Herschel Bulkley law.

For the Newtonian fluid was choose Glycerin at 36°C ($\mu = 0.37 Pas$ at 36°C [2]) and some mesh with different number of cells were selected. Then a velocity was choose and after the simulation, the torque on the impeller was calculated. The best mesh selected was a compromise between low number of cells and accuracy of the solution of the torque. The results are shown below.

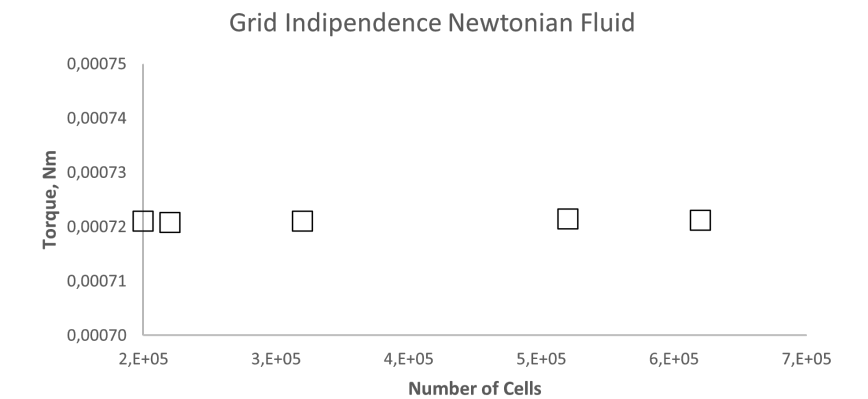


Figure 85. Grid Independence for Newtonian fluid at 70 rpm.



Grid Indipendence Non Newtonian Fluid

Figure 86. Grid Independence for Non-Newtonian fluid at 70 rpm.

Number of Cells

5,E+05

6,E+05

7,E+05

4,E+05

0,001 2,E+05

3,E+05

The optimal number of cells was found to be near 6 hundred thousand. The solutions for the Newtonian fluid were more constant, while for the Non-Newtonian fluid there was more change of the solution for different mesh. The final mesh is shown below.

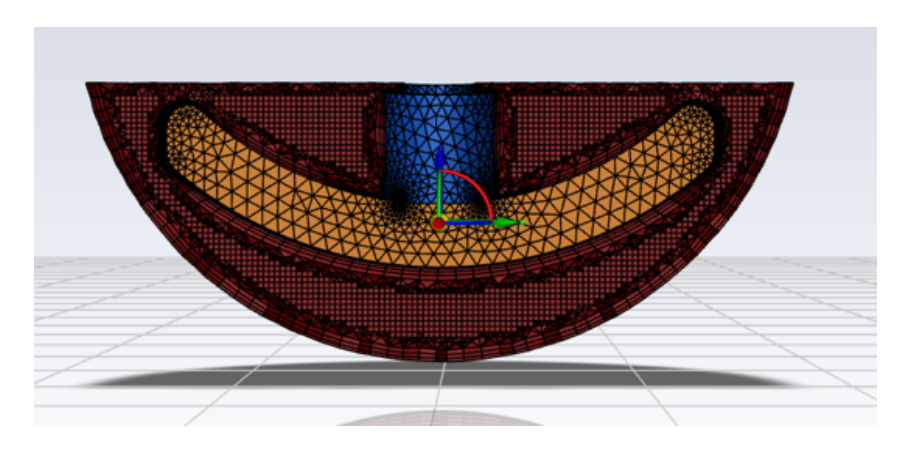


Figure 87. Tornado mesh selected for the simulation.

0.12.3 Metzner Otto Constant

For the calculation of the Metzner Otto constant has been used the same methodology used in the Model Validation Section.

Firstly, the Power constant was calculated using different Newtonian fluids, obtaining the Np-Re curve.

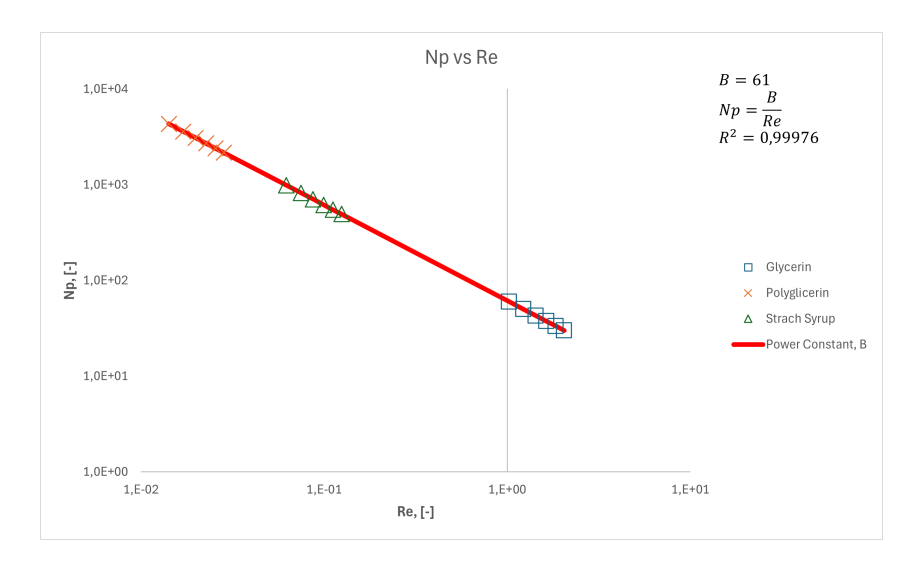


Figure 88. Np-Re for TORNADO Reactor.

In the laminar regime, the slope of the line is a constant value and this value is called Power Constant. For TORNADO Reactor the value is 61.

Then, using the two fluids modeled with the Power Law it was possible to calculate directly the Metzner Otto Constant 21. The values obtained are consisted with each other and summarized in the following table.

Metzner & Otto Constant TORNADO Reactor	Ks
HEC 1.75 %	20
HEC 2.00 %	20

The constant has the same value for both fluids and is lower than that of the IKA Reactor. It should be noted that the Mezter Otto constant depends primarily on the geometry and only marginally on the conditions of fluid motion.

0.12.4 Real Rheology Simulation

In this section, similar to the section of the IKA Reactors, has been simulated the Rheology of the slurry during the liquefaction. The fluid parameters are describer in the Fitting of the experimental Data. From each simulation different parameters are been extracted, like the average shear rate, and the average elongation has been calculated. Firstly, for each simulation has been extracted the value of the torque.

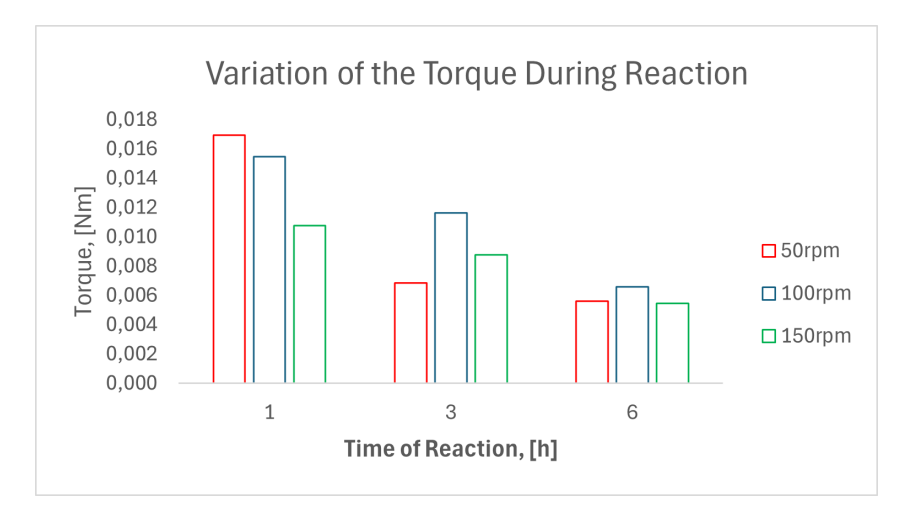


Figure 89. Torque calculated on the impeller for the TORNADO Reactor for different velocities and different time.

It can be observed that during liquefaction, the torque on the impeller decreases, indicating that the fluid is more easily agitated.

The Power required for the agitation can be calculated from the value of torque using (14). With the Power and the Power constant calculated before, the apparent viscosity can be estimated using (19). The results are shown below.

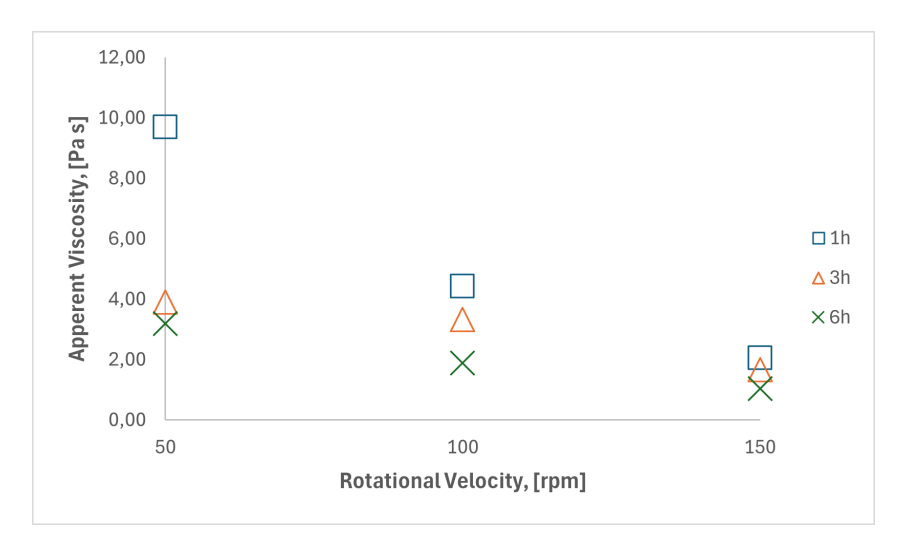


Figure 90. Apparent Viscosity for different velocities during the liquefaction for the TORNADO Reactor.

The graph illustrates the evolution of apparent viscosity throughout the reaction. At lower agitation speeds, for example 50 rpm, the viscosity exhibits a big variation, whereas at higher speeds the changes are considerably less pronounced. This phenomenon can be attributed to the complex rheological behavior of the slurry, whereby viscosity decreases with increasing shear rate.

Similar to the IKA reactors part, it is possible to calculate again the Metzner Otto constant using (29) and compare the values to the ones calculate with the power law fluid.

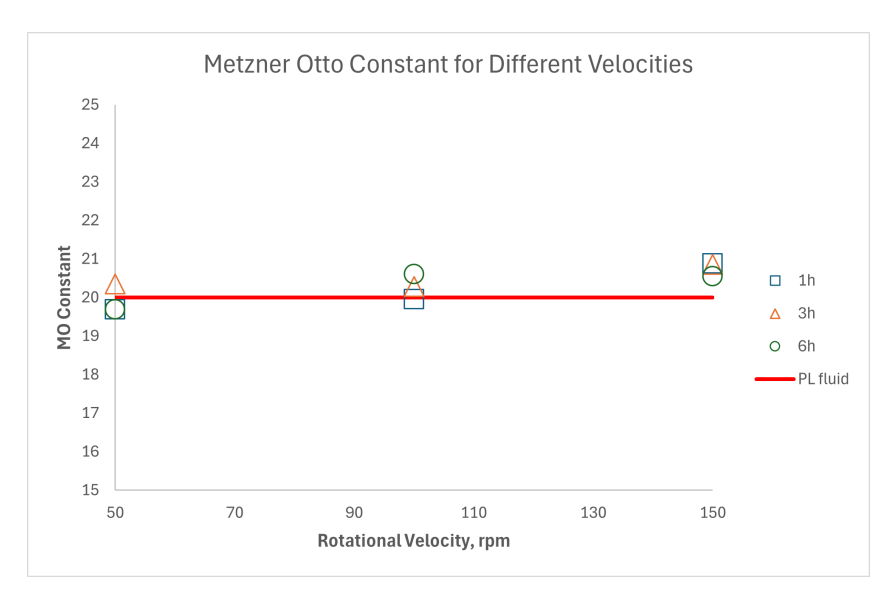


Figure 91. Values of Metzner Otto constant calculated with the Herschel Bulkely model and Power Law model.

The values obtained using the fitting model are close to those calculated with the Power Law. The largest differences occur at high velocities, likely due to the higher Reynolds number. The values are also more consistent compared to the ones calculated for the IKA reactor.

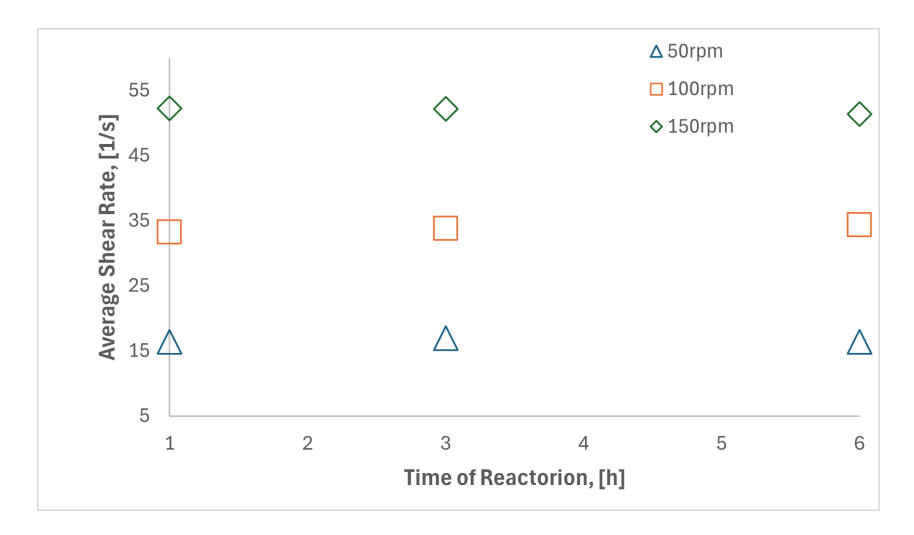


Figure 92. Average Shear Rate during the liquefaction for the TORNADO Reactor.

Knowing the Metzner Otto constant and using the (21) is possible to calculate the average shear rate in the tank. The impeller is able to give a similar average shear rate during the all liquefaction, similar also to the IKA Reactors. As expected, more the rotational speed is high more the average shear rate is high.



Figure 93. Average Elongation during the liquefaction for the TORNADO Reactor.

The values of elongation increase during the first few hours, likely due to the high viscosity of the slurry. Subsequently, the elongation decreases slightly until the end.

In the final part of this section, the presence of low velocity regions was examined. These regions were identified using the critical shear rate as a threshold, with zones exhibiting shear rates below this value classified as stagnant. The corresponding stagnant volume was then quantified as a percentage of the total tank volume.

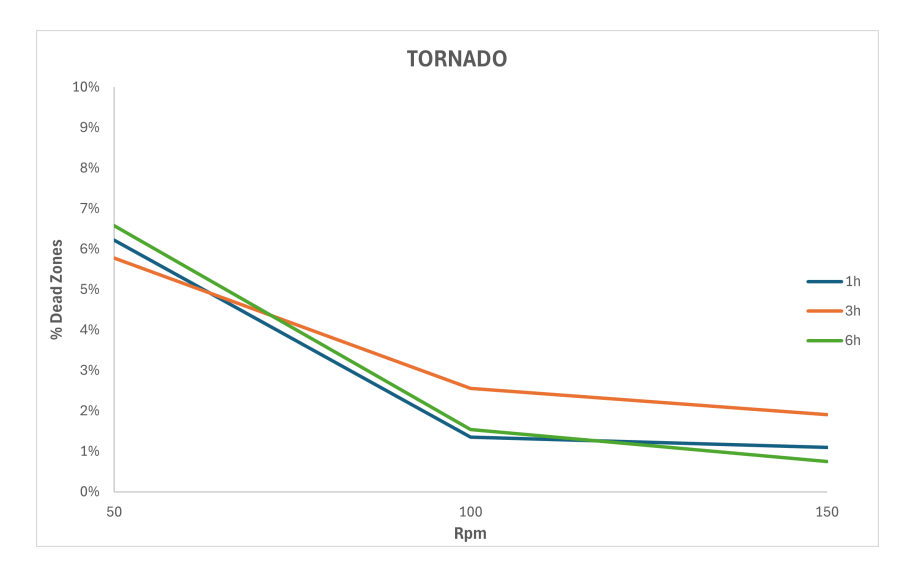


Figure 94. Percentage of dead zones for different velocities.

The stagnant zones are less present in the tank compared to the IKA Reactor, starting with value of about 6-7% for low rotational velocity. Then, the value starts to decrease until the value is approximately negligible, around 1-2%.

0.13 Comparison of Reactor Configurations

In this section, the different reactors configurations (IKA and TORNADO) are compared in terms of average shear rate, elongation, and stagnant zones.

A helpful parameter is the power required for agitation and by dividing this value by the tank volume, it becomes possible to compare reactors with different geometries. Focusing on the shear rate, one can determine the expected average shear rate in the tank for the same P/V input.

This graph (Figure 95 was constructed using the Metzner Otto constant calculated in the previous section. It is important to note that once this constant is known, the power required for agitation can be determined.

The starting point for building the graph is the Metzner Otto equation (22), which allows the estimation of the average shear rate for each rotational speed. From this, and using the Herschel Bulkley model (29) with the average model parameters, the apparent viscosity can be calculated. This makes it possible to determine the apparent Reynolds number. With the power constant obtained in the previous section for each impeller type, the Reynolds number can be used to estimate the power number, and consequently the power

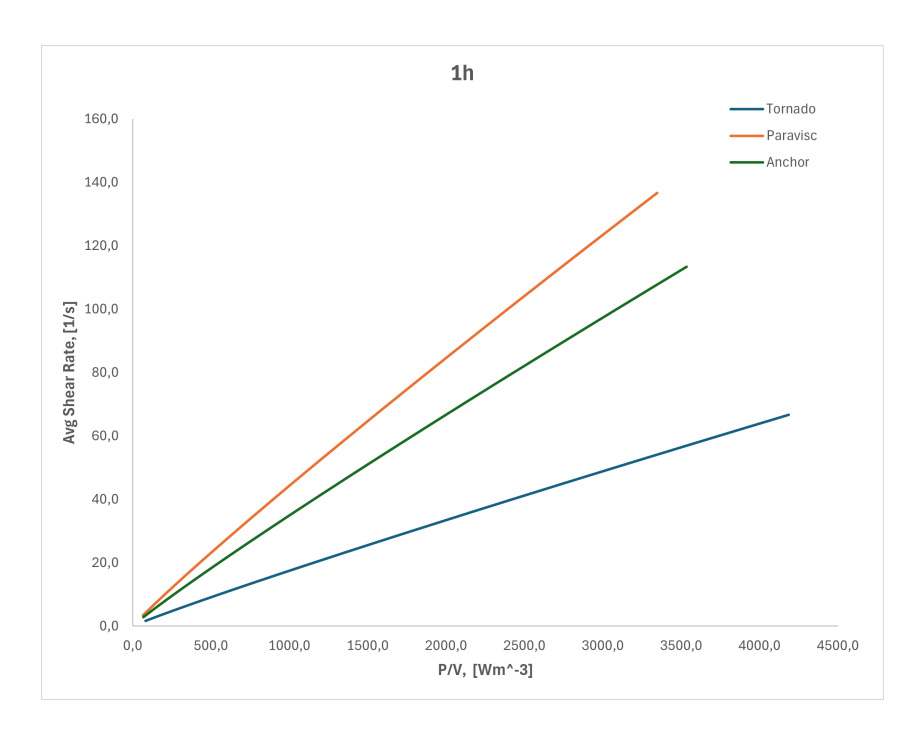


Figure 95. Average shear rate versus Power input per Volume after 1 hour of liquefaction.

The graph highlights the differences between the various reactors and impellers. For the same P/V input, the average shear rate inside the tank can vary significantly. The TORNADO reactor shows lower efficiency compared to the IKA reactors, which exhibit similar performance. The best results are obtained with the Paravisc impeller, as it consistently achieves a higher average shear rate than both the Anchor and the TORNADO. This effect can be explained by the greater ability of the Paravisc to move a larger portion of the fluid within the tank.

A similar graph (Figure 96) can be done also for the average elongation experienced by the fluid during the agitation. To build it, the power required for the agitation has been calculated directly from the torque value, extracted from the results of the simulation.

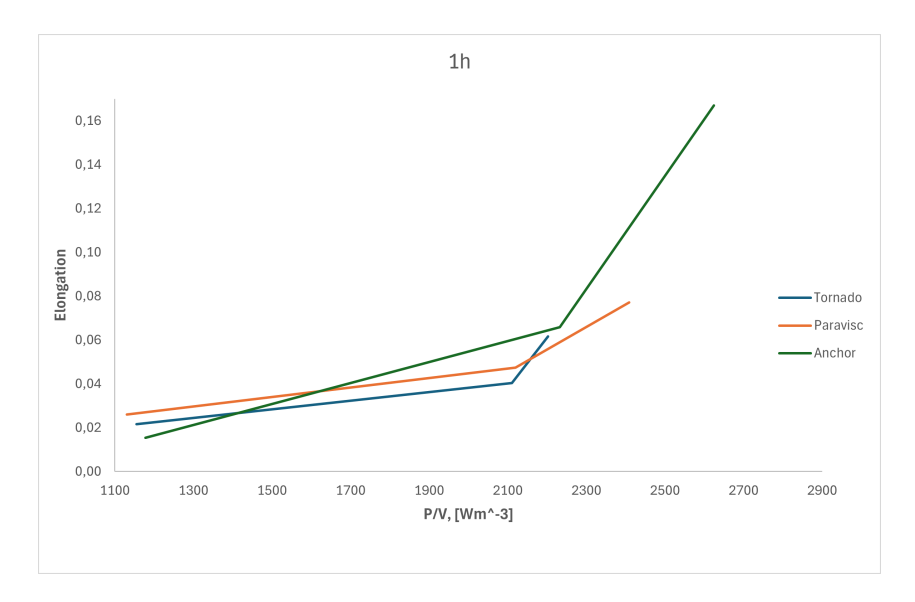


Figure 96. Average elongation versus Power input per Volume after 1 hour of liquefaction.

The value of elongation measured with the Anchor are very different compared to the ones calculated with both the Paravisc and the TORNADO. It means that the Anchor is able to give to the fluid more deformation during the agitation for the same P/V input.

0.14 Correlation between Fluid Agitation and Glucose Conversion

The final section of this work focuses on the analysis of hydrodynamic parameters in the reactors and their relationship with biomass conversion. The rheological behavior was characterized using the Paravisc at three different shear rates, with pretreated wheat straw as the biomass. The rheological parameters employed are those obtained in the section "Fitting of the Experimental Data", where the Herschel Bulkley model was applied.

The aim of this section is to identify which hydrodynamic parameters can explain the observed differences in biomass conversion. At present, only a single set of experiments is available to investigate the effect of agitation on biomass liquefaction, and within this dataset the influence of agitation is not very pronounced. Nevertheless, the following section represents an attempt at a hydrodynamic analysis.

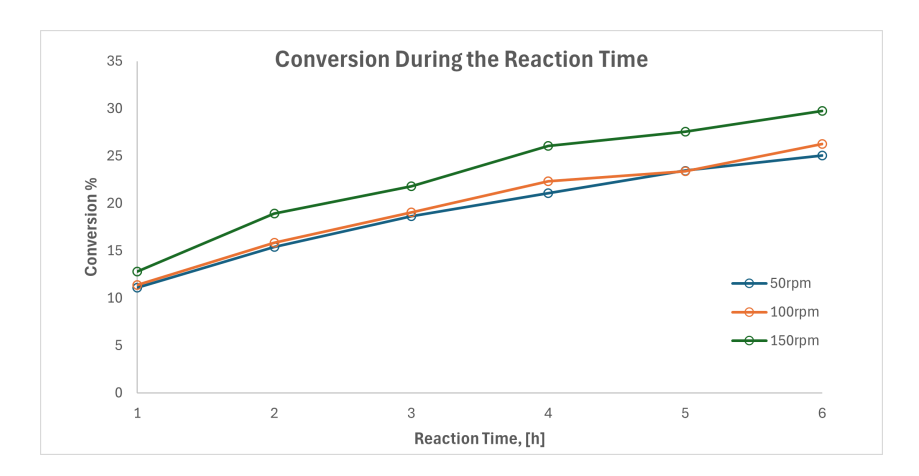


Figure 97. Conversion of glucose during the reaction time for three different velocities.

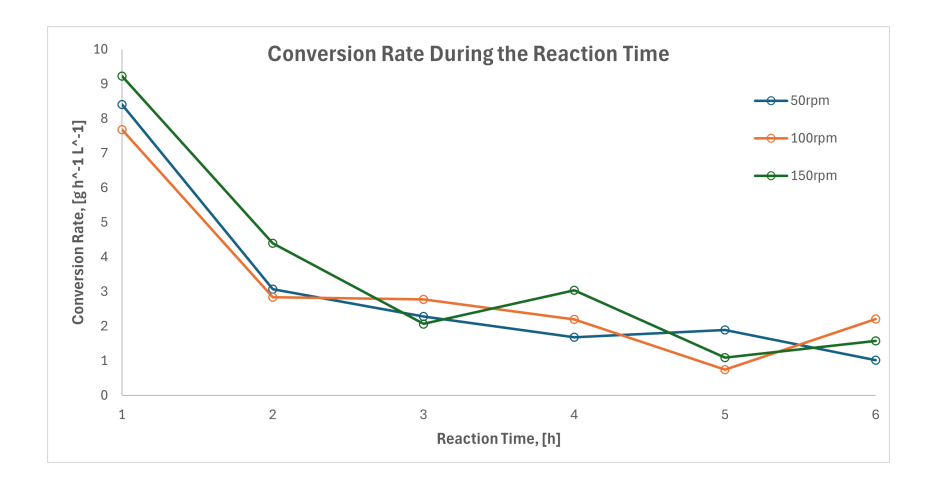


Figure 98. Conversion Rate of glucose during the reaction time for three different velocities.

In the two graphs above (Figure 97 and 98), the glucose conversion over time and the conversion rate during liquefaction are reported for three different rotational velocities. During the first two hours of liquefaction, a clear difference in the conversion rate can be observed at the highest velocity (150 rpm), while the other two conditions show a rather similar behavior. This initial difference in conversion rate translates into a variation in the final biomass conversion, as highlighted in the first graph.

These observations suggest that agitation intensity may play a role in influencing biomass conversion.

To investigate this influences, some hydrodynamics parameters have been chosen and compared to the conversion rate of glucose to find which has the most influences on the conversion. They are: power input, average shear rate, elongation and dead zones.

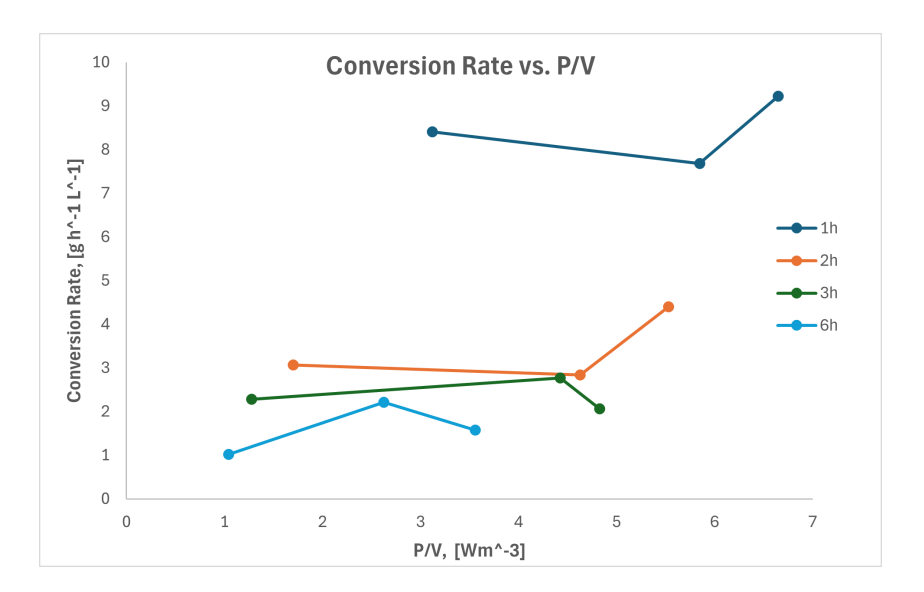


Figure 99. Conversion Rate over Power input for different liquefaction time.

To better highlight the effect of agitation on the conversion rate, a graph such as the one shown above (Figure 99) can be constructed. On the y axis, the conversion rate is reported (expressed in $\frac{g}{h \cdot L}$), while on the x axis a hydrodynamic parameter, such as the power input, is represented. Each curve corresponds to a specific liquefaction time, ranging from 1 to 6 hours, with an additional point at 2 hours included for this analysis. As shown in the figure, an increase in conversion rate is observed at higher power inputs, but only during the first two hours of liquefaction. Beyond this initial phase, the effect is no longer evident. This suggests that power input influences conversion primarily in the early stages of the process.

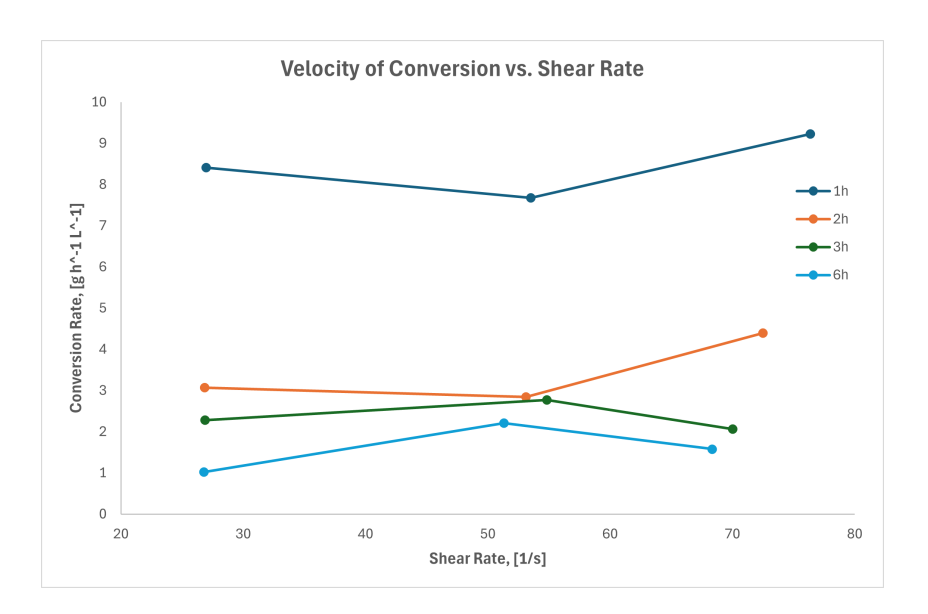


Figure 100. Conversion Rate over Shear Rate for different liquefaction time.

In this case (Figure 100), the selected hydrodynamic parameter is the average shear rate, calculated using the Metzner Otto constant. Similarly, at higher shear rate values an increase in the conversion rate can be observed, but only during the first two hours of liquefaction.

The similar graph can be done also for the elongation and for the dead zones. Every parameters have shown to have an effect on the conversion rate.

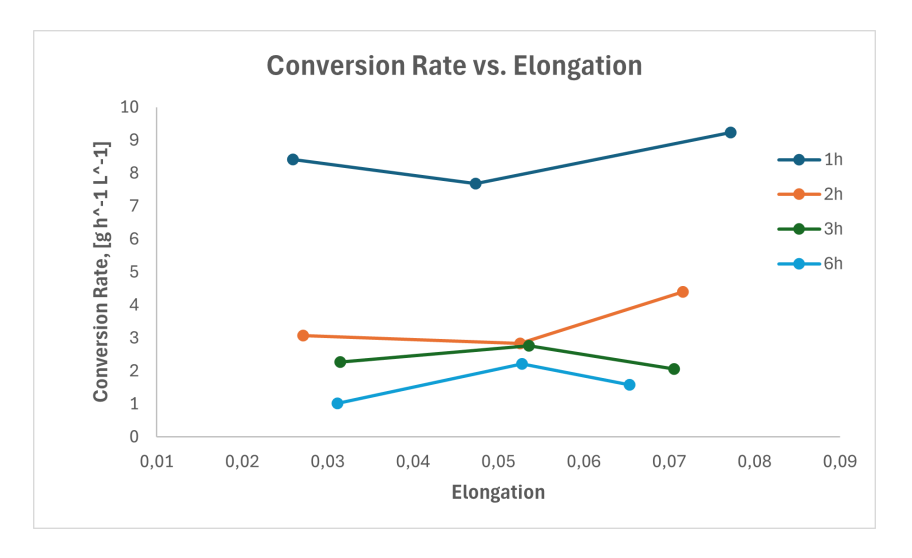


Figure 101. Conversion Rate over Elongation for different liquefaction time.

In the graph (101), the hydrodynamic parameter investigated is elongation, which represents the fluid deformation during motion.

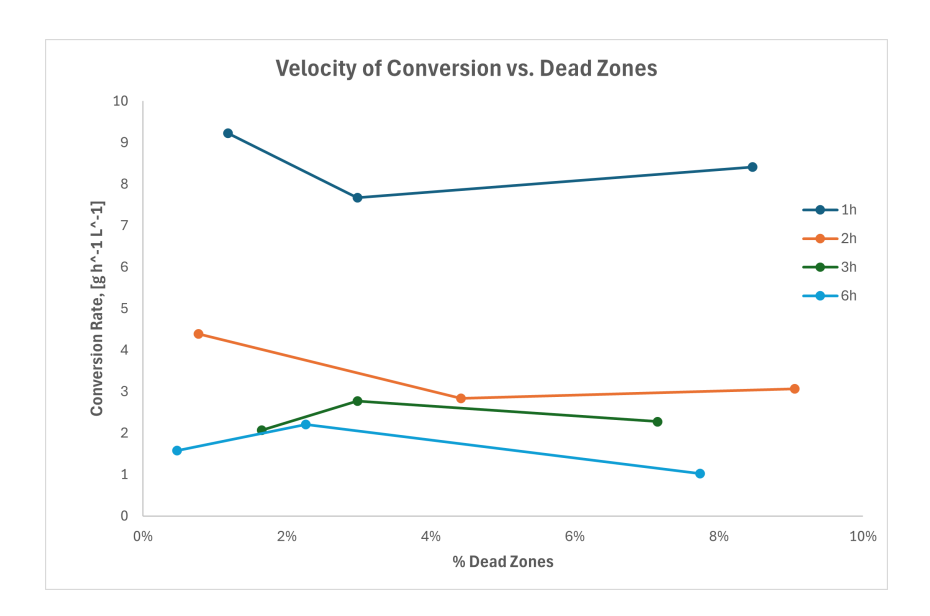


Figure 102. Conversion Rate over Dead Zones for different liquefaction time.

The last graph (102) illustrates the effect of dead zones on the conversion rate. During the first two hours of liquefaction, a reduction in stagnant zones corresponds to an increase in the conversion rate.

These graphs show that each hydrodynamic parameter may have an effect on the conversion rate; however, it is not possible to determine which parameter is the most influential. In fact, using only a single system (Paravisc IKA) makes it impossible to separate the contribution of each parameter and identify which has little or no impact versus which plays the dominant role.

0.15 Conclusion

The liquefaction step in biomass conversion is a complex process due to the non Newtonian rheology of the fluid and the time dependent nature of the process parameters. A good understanding of this step is essential to optimize the process and reduce operational costs.

The aim of this work was to develop a CFD model of the reactors used in the experimental study. To achieve this, a literature review was first conducted to better understand the challenges of the process and the difficulties associated with modeling. A relevant study was then selected and followed to build a model whose results could be trusted. The geometry reported in the paper was recreated, and the torque values on the impeller at different velocities were compared with the experimental data from the study. This approach allowed for validation of the model for both Newtonian and non-Newtonian fluids.

Subsequently, the Metzner Otto constant for the impeller was estimated, and the fraction of dead zones during agitation was calculated for different fluids. Once the validation was done, models of the actual reactors were implemented, including the IKA reactors with

Paravisc and Anchor impellers, as well as the TORNADO reactor.

Using these models, several hydrodynamic parameters were estimated to investigate the effect of agitation on biomass conversion. Experimental data obtained with the Paravisc IKA and pretreated wheat straw were employed for this analysis. Four hydrodynamic parameters were selected and extracted from the simulations: power input, average shear rate, elongation, and dead zones. Comparisons between these parameters and the glucose conversion rate revealed that all of them may have some influence on the conversion, but only during the first two hours of liquefaction; beyond this point, their effect was no longer significant.

In conclusion, it was not possible to determine the individual contributions of each hydrodynamic parameter using a single system (Paravisc IKA). To determine which parameters exert the greatest influence on biomass conversion, additional liquefaction experiments under different conditions (e.g. using a different reactor and impeller) are required. Such experiments would enable a more comprehensive understanding of the role of each parameter in the overall conversion process.

Bibliography

- [1] Joelle Aubin, David F Fletcher, Joël Bertrand, and Catherine Xuereb. Characterization of the mixing quality in micromixers. Chemical Engineering & Technology: Industrial Chemistry-Plant Equipment-Process Engineering-Biotechnology, 26(12):1262–1270, 2003.
- [2] Danilo Carvajal, Daniele L Marchisio, Samir Bensaid, and Debora Fino. Enzymatic hydrolysis of lignocellulosic biomasses via cfd and experiments. *Industrial & engineering chemistry research*, 51(22):7518–7525, 2012.
- [3] Rajendra P Chhabra. Non-newtonian fluids: an introduction. *Rheology of complex fluids*, pages 3–34, 2010.
- [4] Haruki Furukawa, Yoshihito Kato, Yoshiro Inoue, Tomoho Kato, Yutaka Tada, and Shunsuke Hashimoto. Correlation of power consumption for several kinds of mixing impellers. *International Journal of Chemical Engineering*, 2012(1):106496, 2012.
- [5] M Jain and R Misumi. Experimental investigation of the power consumption and metzner-otto constant for highly shear-thinning fluids with different impeller geometries. *Journal of Chemical Engineering of Japan*, 57(1):2387459, 2024.
- [6] AB Metzner and RE Otto. Agitation of non-newtonian fluids. *AIChE Journal*, 3(1):3–10, 1957.
- [7] Alicia A Modenbach and Sue E Nokes. Enzymatic hydrolysis of biomass at high-solids loadings—a review. *Biomass and bioenergy*, 56:526–544, 2013.
- [8] Edward L Paul, Victor A Atiemo-Obeng, Suzanne M Kresta, et al. *Handbook of industrial mixing*. Wiley Online Library, 2004.
- [9] Loukas Petridis and Jeremy C Smith. Molecular-level driving forces in lignocellulosic biomass deconstruction for bioenergy. *Nature Reviews Chemistry*, 2(11):382–389, 2018
- [10] S Murthy Shekhar and S Jayanti. Cfd study of power and mixing time for paddle mixing in unbaffled vessels. *Chemical Engineering Research and Design*, 80(5):482–498, 2002.
- [11] Jonathan J Stickel, Jeffrey S Knutsen, Matthew W Liberatore, Wing Luu, Douglas W Bousfield, Daniel J Klingenberg, C Tim Scott, Thatcher W Root, Max R Ehrhardt, and Thomas O Monz. Rheology measurements of a biomass slurry: an inter-laboratory study. *Rheologica Acta*, 48:1005–1015, 2009.
- [12] Philippe A Tanguy, F Thibault, and E Brito De La Fuente. A new investigation of the metzner-otto concept for anchor mixing impellers. *The Canadian journal of chemical engineering*, 74(2):222–228, 1996.